
Optical High-Order Harmonic Generation in Gas Targets with Spatially Tailored Driving Fields

Erzeugung optischer Hoher Harmonischer in Gas-Targets mit räumlich maßgeschneiderten treibenden Feldern

Masterarbeit
im Studiengang Physik
der Ludwig-Maximilians-Universität München

vorgelegt von
Maximilian Högner

Durchgeführt am
Max-Planck-Institut für Quantenoptik Garching
und an der Ludwig-Maximilians-Universität München
2012–2013

Betreuung: Prof. Dr. Ferenc Krausz,
Dr. Ioachim Pupeza, Dr. Vladislav Yakovlev

Contents

1. Introduction	5
2. High Harmonic Generation in Gas Targets	7
2.1. Simple Man's Model	7
2.2. Lewenstein Model	9
2.3. Limitations and Alternatives	11
2.4. Extension to Elliptically Polarized Driving Fields	12
3. A Computational Model	14
3.1. Definitions	14
3.2. Efficient Implementation of the Lewenstein Model	14
3.3. Driving Field	17
3.3.1. Ultrashort Pulses	19
3.3.2. Elliptically Polarized Driving Field	20
3.3.3. Normalization	20
3.3.4. Effects of the Gas Target	22
3.4. Build-up of the Harmonic Beam	23
3.5. Far Field Distribution of the Harmonic Radiation	27
3.6. Fluorescent Screen	28
3.7. Diffraction Grating	29
3.7.1. 3D Grating Equation	30
3.7.2. Arbitrarily Positioned and Oriented Grating	32
3.7.3. Decomposition of the Incident Field into Plane Waves	35
3.7.4. Far-Field Approximation for a Flat Screen	37
3.7.5. Summary and Implementation	38
4. Theoretical and Experimental Applications	40
4.1. Single Atom Dipole Response – Comparison with the TDSE	40
4.2. Macroscopic Response from a Gas Target	41
4.3. Output Coupling from Enhancement Cavities	45
4.3.1. Motivation	45
4.3.2. HHG in a Quasi-Imaging Resonator	46
5. Outlook	54
5.1. Future Experimental Focus	54
5.2. Extensions of the Computational Model	55

Bibliography	60
A. Documentation of the Code	63
A.1. Overview	63
A.2. Installation	63
A.2.1. MATLAB under Windows	63
A.2.2. GNU Octave under Linux	65
A.3. Reference	66
A.3.1. Driving Field	66
A.3.2. Gauss-Hermite Modes	68
A.3.3. Pulse Shape	72
A.3.4. Dipole Response	73
A.3.5. Propagation of Harmonics	80
A.3.6. Far Field	85
A.3.7. Conversion between SI units and scaled atomic units	89
A.3.8. Matlab Interface to the Implementation of the Lewenstein Model	90

1. Introduction

High-harmonic generation (HHG) is a phenomenon that allows for generating broad-band coherent radiation in the extreme ultraviolet (XUV) and soft X-ray regimes by irradiating a medium with a very intense pulsed laser. The medium usually is realized as a gas stream, but it is also possible to use solid targets, which are subject to damage induced by the high intensities, however. Using HHG in gas targets, it is possible to build table-top XUV sources that allow spectroscopy and microscopy applications with both excellent frequency resolution due to inherent frequency comb features and time resolution in the attosecond regime due to the broad spectrum.

For some applications, it is interesting to achieve not only high intensities of the harmonic radiation, but also to drive the process with a high repetition rate, e.g. for precision spectroscopy applications that require sufficient tooth spacing in the frequency comb, which is also linked to the per-tooth spectral intensity, or for applications where there is an intrinsic limit on the amount of data that can be obtained in a single pass. To achieve a high repetition rate, it is practical to produce the harmonic radiation within an enhancement cavity (EC), which is an externally driven passive resonator that allows to convert lower-intensity seeding laser pulses to considerably higher-intensity circulating pulses. While HHG in general is a rather mature field of research that has already been extensively studied in the last two decades, HHG in enhancement cavities is an actively researched topic for which several interesting questions and challenges remain open, most importantly to find a good mechanism for output coupling of the harmonic radiation and to achieve isolated attosecond pulses.

The primary goal of this thesis was to develop, implement and apply a computational model that allows to investigate and understand the effects of the numerous degrees of freedom on the harmonic radiation produced by gas targets, especially in the context of enhancement cavities, in order to optimize different aspects of the radiation. The most important degrees of freedom come from the choice of the driving field. The non-linear response of a single target particle (here we restrict ourselves to atoms) depends on the time evolution of the electric field at the position of the particle, and the macroscopic field is determined by the coherent superposition of the single-atom responses which makes it depend on the spatial features of the driving field. Interesting aspects for which the output radiation can be optimized are a maximal harmonic yield for a specific harmonic order, the harmonic beam quality (divergence angle, focusability), suitability of the radiation for certain output coupling mechanisms, a continuous and broad-band spectrum, and the reduction of the harmonic radiation to single isolated attosecond pulses per driving field pulse using gating mechanisms.

The first declared task was to convert an existing computational model for the single-atom dipole response from Matlab to C++ in order to improve the performance. I achieved a speed improvement of a factor of 100 and also extended the implementation to elliptically polarized driving fields, which makes it possible to investigate polarization gating methods in the future. The model and the implementation are described in chapter 2.2 and 3.2 in more detail, respectively.

Then, the model was to be extended so that HHG with tailored driving fields can be simulated. For this, I had to familiarize myself with the particular steps that are needed to model the macroscopic response of a gas target. Specifically, building on the idea of an existing implementation developed in the group where I did my thesis, I developed a simple model for a pulsed driving laser beam that is general enough to describe arbitrary superpositions of fundamental and higher-order transverse resonator modes (chapter 3.3). Second, I derived a solution to the well-established first-order propagation equation, which allows to compute the macroscopic electric field of the harmonic radiation from the individual single-atom responses (chapter 3.4) and incorporates phase matching effects. To provide a way to compute the harmonic field within an arbitrarily oriented plane at a larger distance from the gas target, I applied the far-field approximation (chapter 3.5). For comparing data obtained from the computational model with experimental data, I worked out a formula that maps an electric field distribution of the harmonics to the observed image on a fluorescent screen, taking into account the conversion efficiency (chapter 3.6). Moreover, I derived an algorithm that simulates the effect of a diffraction grating with arbitrary orientation placed in the harmonic beam (chapter 3.7).

Finally, the computational model should be used to design, optimize and interpret experiments carried out in the vicinity of our group. For this, I spent several months participating in experimental work in the laboratory, which allowed me to gain some experimental experience, while refining the implementation of the developed model in parallel. At the end of that time, a HHG experiment in an enhancement cavity with a higher-order transverse driving field mode tailored for output coupling was conducted, which enabled me to experience a direct connection between theoretical and experimental work. I took part in the set-up, data acquisition and interpretation steps of the experiment, where the latter one involved intensive usage of the model implemented in the scope of this thesis for investigating the impact of phase matching, the output coupling efficiency and the harmonic beam profiles. The full-widths at half-maximum of the beam profiles determined in the experiment were found to agree very well with the ones obtained from corresponding simulations. Both experiment and simulations are described in detail in chapter 4.3.2.

2. High Harmonic Generation in Gas Targets

High harmonic generation is a means of accomplishing coherent broad-band radiation over a broad spectral range. Using an infrared driving laser with noble gas targets, it is possible to achieve harmonics orders up to several hundreds, i.e. up to the soft x-ray regime. Coherent radiation in this spectral range is usually not accessible without large accelerators.

While the conversion efficiency is very low ($\approx 10^{-7}$), the harmonic radiation shows a plateau behavior in the spectrum, i.e. the intensity of high harmonics does not drop significantly with increasing harmonic order up to a cutoff frequency, which means that the produced radiation can be very broad-band, spanning several octaves. This makes it a very valuable tool for spectroscopy, where the broad spectrum permits a time resolution down to the attosecond domain.

High harmonic generation in gas targets was first observed in 1987 by McPherson et al. [18], who produced harmonics up to the 17th in neon. In 1993, Corkum presented a descriptive semi-classical model for the underlying microscopic process, which is able to explain the most important features like the plateau and cutoff of the harmonic spectrum [7]. Building on the picture suggested by Corkum et al., Lewenstein et al. developed a more elaborate model for the harmonic emission of gas atoms in 1994 [17], which starts with a full quantum mechanical ansatz and makes some well-grounded approximations. This model not only explains all important features of the phenomenon, but also provides quantitatively correct results (except for a prefactor) for the harmonic spectral intensity of a single atom in the regime where the approximations are well fulfilled.

2.1. Simple Man's Model

For an accurate description of what happens in a single atom when it is irradiated with an intense driving field, the most consequent approach would be to solve the three-dimensional time-dependent Schrödinger equation. This is difficult however, especially if multiple electrons are to be considered, and it takes much computation time.

For getting a picture of how high harmonic radiation emerges, the so-called three-step model described by Corkum et al. can be considered. In this model, the process is divided into three steps (see figure 2.1):

- The electric field of the intense driving laser bends the atomic potential so that

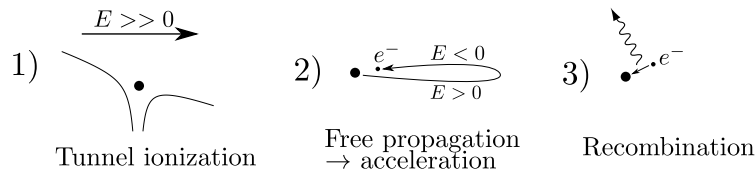


Figure 2.1.: Three step model

an electron can tunnel out (tunnel ionization).

- The now free electron is accelerated away from the atom by the electric field of the driving laser. When the oscillating electric field changes its sign, the electron is accelerated back to the core.
- When the electron reaches the core, it recombines. As the electron acquired kinetic energy during propagation, the emitted radiation can reach high frequencies.

This model is able to explain the most important features of high harmonic generation: First of all, it is easy to see that there is a cutoff frequency. Depending on the strength of the driving field, the electron can only acquire a certain amount of kinetic energy during its way. This limits the energy that can be released upon recombination. The model is even able to predict the value of the cutoff frequency ω_c as

$$\hbar\omega_c \approx 3.17U_p + I_p$$

where $U_p = 2e^2/(c\epsilon_0 m) \cdot I/(4\omega_0^2)$ is the ponderomotive energy of the electron, which depends on the driving field intensity I , and I_p is the ionization potential of the atom. This cutoff law is confirmed experimentally.

Furthermore, one can compute the spectrum of the harmonic radiation with this model if the dependence of the ionization probability of the atom on the driving field is known. This does not yield quantitatively correct results, yet it is possible to see the formation of the plateau.

The model provides another very important insight: When a periodic driving field is assumed, which is a good approximation for long pulses, for a given harmonic frequency there are two distinct electron trajectories that lead to emission at this frequency. One trajectory has a shorter and one a longer excursion time, therefore they are called the short and long trajectory, accordingly. Even though the radiation created by both trajectories interferes, it is often possible to discriminate features of one trajectory even in the far field of the harmonic radiation due to their slightly different behavior.

2.2. Lewenstein Model

Building on this understanding, Lewenstein et al. provided a more sophisticated model for high harmonic generation in gas atoms. It is a quantum-mechanical model with some well-grounded approximations. Following [17] closely, the derivation is outlined shortly.

The starting point is the three-dimensional time-dependent Schrödinger equation (TDSE) for one shell electron

$$i \frac{\partial}{\partial t} |\psi(t)\rangle = \left[-\frac{1}{2} \nabla^2 + V(\mathbf{r}) - E \cos(t)x \right] |\psi(t)\rangle,$$

where $V(\mathbf{r})$ is the atomic potential and the $E \cos(t)x$ term is the additional potential due to a periodic electric field of the driving laser. The magnetic force can be neglected for the intensities at which harmonics are usually generated (below or on the order of 10^{15} W/cm²).

The unit system used here is atomic units but with energies expressed in multiples of the driving laser photon energy, which is called “scaled atomic units” in the following.

The TDSE is solved using an ansatz that is basically a decomposition into vacuum continuum states, but has an extra term for the ground state. Several assumptions and approximations are made on the way:

- The only bound state that plays a role for the evolution of the system is the ground state.
- The depletion of the ground state is neglected. This is only a good assumption if the driving field intensity is weak enough or the interaction time is small, i.e. short driving pulses.
- There is no overlap of the continuum states with the ground state, nor is there a coupling between the continuum states due to the atomic potential $V(\mathbf{r})$. This approximation together with the first are justified by the picture described before: The electron is in the ground state, then ionization occurs (however, only a small fraction of the wave function leaves the ground state) and then the electron propagates freely without impact of the atomic potential. The approximation of free propagation is only valid if the kinetic energy of the electron is high, which requires a strong driving field.

With the derived time-dependent wave function $|\psi(t)\rangle$ it is possible to calculate the time-dependent dipole element

$$\mathbf{d}(t) = -e \cdot \mathbf{r}(t) = -\mathbf{r}(t) = -\langle \psi(t) | \hat{\mathbf{r}} | \psi(t) \rangle,$$

which turns out to be an integral over time and the canonical momentum of the electron. Using a saddle point method, it is possible to perform the integration over the canonical momentum. Applying the saddle point method is equivalent to only

considering momenta that correspond to trajectories that start and end at the same position. Then the dipole moment gets

$$\begin{aligned} \mathbf{d}(t) = -i\mathbf{e}_x \cdot \int_0^\infty d\tau \left(\frac{\pi}{\epsilon + i\tau/2} \right)^{3/2} \cdot E \cos(t - \tau) \cdot D_x(p_s(t, \tau) - A_x(t - \tau)) \times \\ \times \exp(-iS_s(t, \tau)) \cdot D_x^*(p_s(t, \tau) - A_x(t)) + \text{c.c.} \end{aligned} \quad (2.1)$$

This term has an intuitive physical interpretation. The integral can be seen as a sum over complex probability amplitudes for electron trajectories that return to the same point after an excursion time τ . This probability amplitude is constituted of three terms.

The first term $E \cos(t - \tau) \cdot D_x(p_s(t, \tau) - A_x(t - \tau))$ gives the probability amplitude that the driving field $E \cos(t - \tau)$ releases the electron to the continuum. Here, the term $D_x(\mathbf{v}_i)$ gives a coupling of the ground state to the vacuum continuum state corresponding to the initial electron velocity $\mathbf{v}_i = p_s(t, \tau) - A_x(t - \tau)$. The function $D_x(\mathbf{v})$ is given by the dipole matrix elements $\mathbf{D} = \langle \mathbf{v} | \mathbf{r} | 0 \rangle$, where $|\mathbf{v}\rangle$ denotes the vacuum continuum state for the electron velocity \mathbf{v} and $|0\rangle$ denotes the ground state.

The second term $\exp(-iS_s(t, \tau))$ is the phase that the electron acquires during propagation, where S_s is the quasiclassical action corresponding to the trajectory. The term for the quasiclassical action, which is given later, manifests a close analogy to the classical action for a freely propagating electron that does not see the atomic potential.

The third term $D_x^*(p_s(t, \tau) - A_x(t))$ gives the probability amplitude for “recombination”, i.e. a coupling of the vacuum continuum state corresponding to the recollision velocity $\mathbf{v}_r = p_s(t, \tau) - A_x(t)$ with the ground state. Note that the word recombination does not describe well what is happening – this is in fact not a recombination, as the picture of Corkum suggests, but interference of the ground state wave function with the returning wave packet.

During propagation, the electronic wave packet disperses so that the overlap with the ground state wave function will become smaller with increasing excursion time τ . This is what the prefactor $(\pi/(\epsilon + i\tau/2))^{3/2}$ accounts for. Here, ϵ is a small positive constant that prevents the integrand from diverging for $\tau = 0$.

The model of Lewenstein et al. is successful in explaining all important features of high harmonics like the plateau and the cutoff, and can easily be used to compute the dipole response of single atoms and from this, using a Fourier transformation, the dipole spectrum. In the regime where the approximations are valid, it is able to reproduce the shape of the dipole spectra obtained from solving the TDSE (see e.g. [16]). Moreover, it clearly reproduces the intuitive picture suggested by Corkum using well-grounded approximations.

2.3. Limitations and Alternatives

However, it is very important to know when these approximations are justified and when they are not. The first assumption is that the magnetic force on the electron due to the driving field can be neglected. This force grows with both the driving field intensity and the driving field wavelength. A valid regime would be e.g. for intensities below 10^{16} W/cm² and wavelengths below 2000 nm [4].

Moreover, in the formula provided for the dipole moment, the depletion of the ground state is neglected. For short pulses at low intensities, this is not a problem, but when the interaction time or the driving field intensity is larger, the ground state depletion must be accounted for. This limitation can be fixed, however – the paper of Lewenstein et al. also provides a formula where depletion is not neglected.

A key assumption of the model is that the electron can propagate freely, without seeing the atomic potential, after ionization occurred. This is only the case if the kinetic energy of the free electron is sufficiently high, i.e. when the driving field has a high intensity. To check whether the intensity is high enough, one can consider the Keldysh parameter

$$\gamma = \sqrt{\frac{I_p}{2U_p}},$$

which should be much smaller than one – this corresponds to a regime where tunnel ionization and not multiphoton ionization is the dominant process. So in order for the approximations to work, there are lower and upper bounds on the driving field intensity.

In the classical picture on which the Lewenstein model builds, it is not possible to produce harmonics with a photon energy below the ionization energy I_p , so the Lewenstein model cannot be expected to deliver accurate results for these harmonics. However, another very important conclusion from the free propagation assumption is that also harmonics with a photon energy slightly above the ionization energy are not handled well. The reason is that these harmonics correspond to electron trajectories with a low kinetic energy on recollision so that the effect of the atomic potential cannot be neglected. Moreover, for these trajectories the electrons generally do not achieve a large distance to the core.

One assumption of the model is that only one outer shell electron is considered. Although harmonics are usually created with noble gases that have many outer shell electrons, this so-called single active electron approximation works fine for HHG in the strong field regime.

For applying the Lewenstein model, one needs the dipole matrix elements $\mathbf{D} = \langle \mathbf{v} | \mathbf{r} | 0 \rangle$. These dipole matrix elements depend on the ground state $|0\rangle$ which in turn depends on the atomic potential $V(\mathbf{r})$. As it is not obvious how to choose the atomic potential in the case of multiple electrons, the paper of Lewenstein et al. suggests several simple model ground states. Depending on the used dipole matrix elements, the obtained dipole spectra change considerably. One commonly used method to get the dipole matrix elements is to consider a hydrogen-like potential scaled for a given

ionization potential I_p . Then the dipole matrix elements in scaled atomic units are

$$\mathbf{D}(\mathbf{v}) = i \left(\frac{2^{7/2} \alpha^{5/4}}{\pi} \right) \frac{\mathbf{v}}{(\mathbf{v}^2 + \alpha)^3} \quad (2.2)$$

with $\alpha = 2I_p$. If one wants to obtain quantitatively better results, however, it is necessary to use more accurate dipole matrix elements.

Nowadays, several promising alternatives and extensions to the Lewenstein model, which was already introduced in 1994, are available. E.g. Plaja et al. [23] present a model that can quantitatively reproduce the harmonic yield for high harmonics, with significantly improved computation time compared to solving the TDSE. Frolov et al. [10] derive analytic formulas for the harmonic spectral density that can be applied to pulses with arbitrary length and carrier-envelope phase. Le et al [16] provide an easy method to scale the harmonic yield predicted the Lewenstein model which significantly improves the data for lower harmonics.

For the purpose of this thesis, we nonetheless decided to adopt the Lewenstein model, at least for first computational implementation, for the following reasons: First of all, it is easy to implement. Second, it can be implemented efficiently, so that a personal computer can compute hundreds of dipole responses per second. Third, it is well-established. It has been used and verified in many publications, which means that its strengths and limitations are well-known and that it is easy to find data to which the implementation can be compared (see chapter 4.1). Moreover, apart from the dipole matrix elements and the ionization potential of the model atom, no additional data is needed for performing simulations. Another advantage is that the model has a nice interpretation in terms of probability amplitudes. Finally, it is easy to extend the model to elliptically polarized driving fields, which is done in the next chapter.

2.4. Extension to Elliptically Polarized Driving Fields

The original paper of Lewenstein et al. assumed a periodic, linearly polarized driving field. It is however possible to generalize the formula for a general driving field $\mathbf{E}(t)$ with arbitrary polarization, which is done in [3]. Instead of formula (2.1), one obtains

$$\begin{aligned} \mathbf{d}(t) = -i\mathbf{e}_x \cdot \int_0^\infty d\tau \left(\frac{\pi}{\epsilon + i\tau/2} \right)^{3/2} \cdot [\mathbf{E}(t) \cdot \mathbf{D}(\mathbf{p}_s(t, \tau) - \mathbf{A}(t - \tau))] \times \\ \times \exp(-iS_s(t, \tau)) \cdot \mathbf{D}^*(\mathbf{p}_s(t, \tau) - \mathbf{A}(t)) + \text{c.c.} \end{aligned} \quad (2.3)$$

which is constituted of the same terms as before but uses vector quantities. Here, $\mathbf{A}(t)$ is the vector potential given by

$$\mathbf{A}(t) = - \int_{-\infty}^t dt' \mathbf{E}(t'), \quad (2.4)$$

the stationary value of the canonical momentum is given by

$$\boldsymbol{p}_s(t, \tau) = \int_{t-\tau}^t dt'' \boldsymbol{A}(t'')/\tau \quad (2.5)$$

and the quasiclassical action is given by

$$S_s(t, \tau) = \int_{t-\tau}^t dt'' \left(\frac{(\boldsymbol{p}_s(t, \tau) - \boldsymbol{A}(t''))^2}{2} + I_p \right). \quad (2.6)$$

3. A Computational Model

3.1. Definitions

There are two alternative sign conventions for describing a plane wave:

$$E_{\text{pw}}(\mathbf{r}, \omega) = Ae^{i(\omega t - \mathbf{k} \cdot \mathbf{r} + \phi_0)}$$

$$E_{\text{pw}}(\mathbf{r}, \omega) = Ae^{i(\mathbf{k} \cdot \mathbf{r} - \omega t + \phi_0)}$$

Here, we choose the latter one. Consequently, we use the following expression for the inverse temporal Fourier transform:

$$\mathcal{F}_t^{-1} \{ \tilde{f} \} = \frac{1}{2\pi} \int \tilde{f}(\omega) \cdot e^{-i\omega t} d\omega \quad (3.1)$$

This corresponds to a Fourier transform

$$\mathcal{F}_t \{ f \} = \int f(t) \cdot e^{i\omega t} dt. \quad (3.2)$$

On the contrary, for the two-dimensional inverse spatial Fourier transforms we use

$$\mathcal{F}_{xy}^{-1} \{ \tilde{f} \} = \frac{1}{(2\pi)^2} \iint \tilde{f}(k_x, k_y) \cdot e^{i(k_x x + k_y y)} dk_x dk_y, \quad (3.3)$$

which corresponds to a Fourier transform

$$\mathcal{F}_{xy} \{ f \} = \iint f(x, y) \cdot e^{-i(k_x x + k_y y)} dx dy. \quad (3.4)$$

3.2. Efficient Implementation of the Lewenstein Model

To get the single atom dipole response $\mathbf{d}(t)$, we need to numerically evaluate integral (2.3):

$$\begin{aligned} \mathbf{d}(t) = & -i\mathbf{e}_x \cdot \int_0^\infty d\tau \left(\frac{\pi}{\epsilon + i\tau/2} \right)^{3/2} \cdot [\mathbf{E}(t) \cdot \mathbf{D}(\mathbf{p}_s(t, \tau) - \mathbf{A}(t - \tau))] \times \\ & \times \exp(-iS_s(t, \tau)) \cdot \mathbf{D}^*(\mathbf{p}_s(t, \tau) - \mathbf{A}(t)) + \text{c.c.} \end{aligned} \quad (3.5)$$

For this, a simple trapezoidal rule can be used, which can be implemented easily and efficiently.

One problem that must be solved is that the upper limit of the integral is infinity. Physically, τ represents the excursion time of the electron and the prefactor of the integrand $(\pi/(\epsilon + i\tau/2))^{3/2}$ accounts for the spread of the returning wave packet. The longer the excursion time, the more time the wave packet will spread and the less overlap the returning wave packet will have with the ground state wave function, which is why the prefactor falls rapidly with increasing τ . Therefore, no large error is made if the upper integration limit is replaced by a suitable finite value. However, due to the rapidly oscillating integrand, simply cutting the integral at a finite value would introduce artifacts into the dipole response, which would result in a noise-like background in the dipole spectrum. So it is better to apply a soft window at the upper integration limit, i.e. to evaluate the integral

$$\begin{aligned} \mathbf{d}(t) = -ie_x \cdot \int_0^{\tau_{\max}} d\tau w(\tau) \cdot \left(\frac{\pi}{\epsilon + i\tau/2} \right)^{3/2} \cdot [\mathbf{E}(t) \cdot \mathbf{D}(\mathbf{p}_s(t, \tau) - \mathbf{A}(t - \tau))] \times \\ \times \exp(-iS_s(t, \tau)) \cdot \mathbf{D}^*(\mathbf{p}_s(t, \tau) - \mathbf{A}(t)) + \text{c.c.} \end{aligned} \quad (3.6)$$

where $w(\tau)$ is a weight function with $w(\tau) = 1$ for an interval $[0, \tau_1]$, then a falling soft window in the interval $[\tau_1, \tau_{\max}]$ and finally $w(\tau_{\max}) = 0$. The lower τ_{\max} is chosen, the larger the error will be that we make, but the less time the numerical integration takes. So it is necessary to find a good compromise between speed and accuracy. Most physically interesting effects are covered if the short and long trajectories are both included, for which we need at least $\tau_1 = T$, where T is the cycle duration of the driving field. To suppress the noise, a \cos^2 window of duration $T/2$ is sufficient, i.e. $\tau_{\max} = \frac{3}{2}T$.

Another problem is that the integrand in turn contains other integrals given by (2.4) to (2.6):

$$\begin{aligned} \mathbf{A}(t) &= - \int_{-\infty}^t dt' \mathbf{E}(t') \\ \mathbf{p}_s(t, \tau) &= \int_{t-\tau}^t dt'' \mathbf{A}(t'')/\tau \\ S(\mathbf{p}_s, t, \tau) &= \int_{t-\tau}^t dt'' \left(\frac{(\mathbf{p}_s(t, \tau) - \mathbf{A}(t''))^2}{2} + I_p \right) \end{aligned}$$

These sub-integrals need to be computed for every value of τ , therefore we need to find a way to evaluate them efficiently. For this, we rewrite the last two expressions as follows:

$$\begin{aligned} \mathbf{p}_s(t, \tau) &= \int_{t-\tau}^t dt'' \mathbf{A}(t'')/\tau = \\ &= \frac{1}{\tau} \int_0^t dt'' \mathbf{A}(t'') - \frac{1}{\tau} \int_0^{t-\tau} dt'' \mathbf{A}(t'') = \\ &= \frac{1}{\tau} (\mathbf{B}(t) - \mathbf{B}(t - \tau)) \end{aligned}$$

where we define $\mathbf{B}(t) := \int_0^t dt'' \mathbf{A}(t'')$, and

$$\begin{aligned}
S(\mathbf{p}_s, t, \tau) &= \int_{t-\tau}^t dt'' \left(\frac{(\mathbf{p}_s(t, \tau) - \mathbf{A}(t''))^2}{2} + I_p \right) = \\
&= \int_{t-\tau}^t \frac{\mathbf{p}_s^2(t, \tau)}{2} dt'' - \int_{t-\tau}^t \frac{2\mathbf{p}_s(t, \tau) \mathbf{A}(t'')}{2} dt'' + \int_{t-\tau}^t \frac{\mathbf{A}^2(t'')}{2} dt'' + \tau I_p = \\
&= \frac{\tau}{2} \mathbf{p}_s^2(t, \tau) - \mathbf{p}_s(t, \tau) \int_{t-\tau}^t \mathbf{A}(t'') dt'' + \int_{t-\tau}^t \frac{1}{2} \mathbf{A}(t'')^2 dt'' + \tau I_p = \\
&= \frac{\tau}{2} \mathbf{p}_s^2(t, \tau) - \mathbf{p}_s(t, \tau) (\mathbf{B}(t) - \mathbf{B}(t - \tau)) + \\
&\quad + \frac{1}{2} \left(\int_0^t \mathbf{A}^2(t'') dt'' - \int_0^{t-\tau} \mathbf{A}^2(t'') dt'' \right) + \tau I_p = \\
&= \left(\frac{\tau}{2\tau^2} - \frac{1}{\tau} \right) (\mathbf{B}(t) - \mathbf{B}(t - \tau))^2 + \frac{1}{2} (C(t) - C(t - \tau)) + \tau I_p = \\
&= \tau I_p - \frac{1}{2\tau} (\mathbf{B}(t) - \mathbf{B}(t - \tau))^2 + \frac{1}{2} (C(t) - C(t - \tau))
\end{aligned}$$

where we define $C(t) := \int_0^t dt'' \mathbf{A}^2(t'')$. Then the quantities $\mathbf{B}(t)$ and $C(t)$ can be easily precomputed, again using the trapezoidal rule, so that we do not need to evaluate the integrals $\mathbf{p}_s(t, \tau)$ and $S(\mathbf{p}_s, t, \tau)$ for each value of τ .

One problem that remains to be solved is the infinite lower limit of the integral

$$\mathbf{A}(t) = - \int_{-\infty}^t dt' \mathbf{E}(t').$$

This may not be a problem if $\mathbf{E}(t) = 0$ for $t < t_{\min}$, but it certainly is e.g. for a periodic driving field $\mathbf{E}(t)$. However, $\mathbf{x}(t)$ does not change its value if we simply replace $\mathbf{A}(t)$ by

$$\mathbf{A}'(t) := - \int_0^t dt' \mathbf{E}(t'),$$

as it only contains expressions of the form $\mathbf{p}_s(t_1, \tau) - \mathbf{A}(t_2)$, which are invariant if we substitute \mathbf{A} by \mathbf{A}' :

$$\begin{aligned}
\mathbf{p}_s(t_1, \tau) - \mathbf{A}(t_2) &= \int_{t_1-\tau}^{t_1} dt'' \mathbf{A}(t'') / \tau - \mathbf{A}(t_2) \\
&= \int_{t_1-\tau}^{t_1} dt'' \left(\mathbf{A}'(t'') - \int_{-\infty}^0 dt' \mathbf{E}(t') \right) / \tau - \left(\mathbf{A}'(t_2) - \int_{-\infty}^0 dt' \mathbf{E}(t') \right) \\
&= \int_{t_1-\tau}^{t_1} dt'' \mathbf{A}'(t'') / \tau - \int_{-\infty}^0 dt' \mathbf{E}(t') \int_{t_1-\tau}^{t_1} dt'' / \tau + \int_{-\infty}^0 dt' \mathbf{E}(t') - \mathbf{A}'(t_2) \\
&= \int_{t_1-\tau}^{t_1} dt'' \mathbf{A}'(t'') / \tau - \mathbf{A}'(t_2) \\
&= \mathbf{p}_s^{\mathbf{A}'}(t_1, \tau) - \mathbf{A}'(t_2)
\end{aligned}$$

So finally, we are able to precompute $\mathbf{A}'(t)$, $\mathbf{B}(t)$ and $C(t)$, so that the τ integration can be performed efficiently without doing further integrations.

3.3. Driving Field

To model the driving field, we make two assumptions. First of all, it is assumed that the refractive index n is isotropic, spatially homogenous and does not change with time. This is the case before the driving field hits the gas target. Within the target, however, this assumption can be problematic, as described in chapter 3.3.4. Second, the driving field is assumed to be collimated around an optical axis, i.e. it has the form of a beam.

The general ansatz we use for the electric field $\mathbf{E}(\mathbf{r}, t)$ is a temporal Fourier decomposition

$$\mathbf{E}(\mathbf{r}, t) = \frac{1}{2\pi} \int \tilde{\mathbf{E}}(\mathbf{r}, \omega) e^{-i\omega t} d\omega. \quad (3.7)$$

When this is inserted into the wave equation, which follows from the Maxwell equations in absence of free charges and currents, we get the following equation for the frequency components $\tilde{\mathbf{E}}$:

$$\Delta \tilde{\mathbf{E}}(\mathbf{r}, \omega) + k^2 \tilde{\mathbf{E}}(\mathbf{r}, \omega) = 0 \quad (3.8)$$

Here, the wave number k is given by $k(\omega) = n(\omega) \cdot \omega/c$. The assumptions we made allow us to use the more convenient paraxial wave equation instead. For this, we choose the optical axis to be equal with the z axis, and use the ansatz

$$\tilde{\mathbf{E}} = \begin{pmatrix} U_1 \\ U_2 \\ 0 \end{pmatrix} \cdot e^{ik(\omega)z}, \quad (3.9)$$

which is chosen so that U_i vary slowly in z direction. Therefore, if the ansatz is inserted into (3.8), the $\frac{\partial^2}{\partial z^2}$ part of the Laplacian can be neglected. This is called paraxial approximation. We arrive at the so-called “paraxial wave equation” (compare to (1.5) in [19])

$$\Delta_{\perp} U_i + 2ik \frac{\partial U_i}{\partial z} = 0. \quad (3.10)$$

This is an inhomogenous differential equation, for which an orthonormal basis of solution functions can be provided. One commonly used set of solution functions leads to the so-called “Gauss-Hermite modes” (compare to e.g. (2.25) and (2.28) in

[19]¹) when inserted back into the ansatz (3.9):

$$\begin{aligned}\tilde{E}_i(\mathbf{r}, \omega) = \text{GH}_{nm}(\mathbf{r}) := & \frac{w_0}{w(z)} \cdot H_n \left(\sqrt{2} \frac{x}{w(z)} \right) \exp \left(-\frac{x^2}{w^2(z)} \right) \times \\ & H_m \left(\sqrt{2} \frac{y}{w(z)} \right) \exp \left(-\frac{y^2}{w^2(z)} \right) \times \\ & \exp \left[i \left(kz - \Phi_{nm}(z) + \frac{k}{2R(z)}(x^2 + y^2) \right) \right]\end{aligned}\quad (3.11)$$

with the subexpressions

$$w(z) = w_0 \sqrt{1 + (z/z_R)^2}, \quad (3.12)$$

$$R(z) = z + z_R^2/z, \quad (3.13)$$

$$\Phi_{nm}(z) = (n + m + 1) \arctan(z/z_R), \quad (3.14)$$

$$z_R = \frac{k w_0^2}{2}, \quad (3.15)$$

the physical Hermite polynomials $H_n(x)$, and the parameters $n \in \mathbb{N}_0$, $m \in \mathbb{N}_0$, w_0 and $k = n(\omega) \cdot \omega/c$. For given parameters w_0 and k , the Gauss-Hermite modes GH_{nm} form a complete orthonormal basis for the solution space of the wave equation in paraxial approximation. There are also other basis systems in use, e.g. the Gauss-Laguerre modes that arise from a treatment in cylindrical coordinates. The advantage of the Gauss-Hermite modes is that they can be excited directly in cavities by choosing the geometry so that they become resonant. So while the general solution is a superposition of Gauss-Hermite modes, it is often sufficient to only consider one mode except the cavity is tuned so that multiple modes are resonant at the same time (see chapter 4.3.2). The most commonly used mode is GH_{00} , which corresponds to a Gaussian beam.

The parameter w_0 is called the beam waist of the mode, as it describes the minimal beam radius in transverse direction, which is realized at $z = 0$. z_R is the Rayleigh range and is half the size of the focal region in z direction. Φ_{nm} is an additional z -dependent phase and called “Gouy phase”. For a given z position, $R(z)$ is the phase front curvature and $w(z)$ is the beam radius.

Note that this basis system is only a convenient description if the focus is situated at $z = 0$. In the following, we always choose our coordinate system so that this is the case.

¹signs adapted to the sign convention used here; see chapter 3.1

3.3.1. Ultrashort Pulses

If the driving field is an ultrashort pulse, the spectrum is broad, i.e. the driving field is constituted of many frequency components $\tilde{\mathbf{E}}(\mathbf{r}, \omega)$, which in turn are superpositions of Gauss-Hermite modes. Inserting the decomposition in Gauss-Hermite modes, the ansatz (3.7) for one electric field component becomes

$$E_i(\mathbf{r}, t) = \frac{1}{2\pi} \int \underbrace{\left(\sum_{nm} A_{nm}(\omega) \text{GH}_{nm,\omega}(\mathbf{r}) \right)}_{\tilde{E}(\mathbf{r}, \omega)} e^{-i\omega t} d\omega. \quad (3.16)$$

To fully describe a general spectrally broad driving field, all coefficients $A_{nm}(\omega)$ must be known, which is impractical. Therefore, we make a simplification and assume that each frequency component consists of the *same* superposition $M_\omega(\mathbf{r})$ of modes:

$$E_i(\mathbf{r}, t) = \frac{1}{2\pi} \int F(\omega) \underbrace{\left(\sum_{nm} A_{nm} \text{GH}_{nm,\omega}(\mathbf{r}) \right)}_{M_\omega(\mathbf{r})} e^{-i\omega t} d\omega, \quad (3.17)$$

i.e. we assume that $A_{nm}(\omega)$ can be decomposed into two terms where one accounts for the time dependence and one for the spatial shape:

$$A_{nm}(\omega) = F(\omega) A_{nm}. \quad (3.18)$$

Now, only the parameters A_{nm} and $F(\omega)$ are needed for a description of the driving field. For $F(\omega)$, we can use a similar approach to [29] and take over the Fourier coefficients of a given pulse shape $\mathcal{E}(t)$:

$$F(\omega) = \mathcal{F}_t \{ \mathcal{E}(t) \} (\omega) \quad (3.19)$$

Then, $E_i(\mathbf{r}, t)$ reproduces the pulse shape $\mathcal{E}(t)$ up to a prefactor at the origin $\mathbf{r} = 0$. This can be shown easily. At the origin, $M_\omega(\mathbf{r})$ does not depend on ω :

$$M_\omega(\mathbf{0}) = \sum_{nm} A_{nm} \text{GH}_{nm,\omega}(\mathbf{0}) = \sum_{nm} A_{nm} H_n(0) H_m(0) = M_0 \quad (3.20)$$

So, (3.21) becomes

$$\begin{aligned} E_i(\mathbf{0}, t) &= \frac{1}{2\pi} \int F(\omega) M_0 e^{-i\omega t} d\omega = \\ &= M_0 \mathcal{F}_t^{-1} \{ F(\omega) \} (t) = M_0 \mathcal{E}(t) \end{aligned} \quad (3.21)$$

This means that now we can specify a driving field by giving its spatial shape by coefficients A_{nm} and the temporal pulse shape $\mathcal{E}(t)$ at the origin. The temporal pulse shape is in general position-dependent. In many cases, however, this only manifests in a shift of the carrier-envelope (CE) phase, while the envelope is position-independent. Distortions even of the envelope can occur for few-cycle pulses and tight focusing.

Note that for some superpositions of modes, the prefactor M_0 may be zero, i.e. $E_i(\mathbf{0}, t) = 0$. Then the given pulse shape $\mathcal{E}(t)$ is not reproduced exactly at any position.

3.3.2. Elliptically Polarized Driving Field

In absence of a medium, the electric field components $E_x(\mathbf{r}, t)$ and $E_y(\mathbf{r}, t)$ are independent. Therefore, for the case of a driving field with general polarization, we have two sets of coefficients $\{F_x(\omega), A_{x,nm}\}$ and $\{F_y(\omega), A_{y,nm}\}$:

$$\begin{aligned} E_x(\mathbf{r}, t) &= \frac{1}{2\pi} \int F_x(\omega) \underbrace{\left(\sum_{nm} A_{x,nm} \text{GH}_{nm,\omega}(\mathbf{r}) \right)}_{M_{x,\omega}(\mathbf{r})} e^{-i\omega t} d\omega \\ E_y(\mathbf{r}, t) &= \frac{1}{2\pi} \int F_y(\omega) \underbrace{\left(\sum_{nm} A_{y,nm} \text{GH}_{nm,\omega}(\mathbf{r}) \right)}_{M_{y,\omega}(\mathbf{r})} e^{-i\omega t} d\omega \\ E_z(\mathbf{r}, t) &= 0 \end{aligned} \quad (3.22)$$

with

$$\begin{aligned} F_x(\omega) &= \mathcal{F}_t \{ \mathcal{E}_x(t) \} (\omega), \\ F_y(\omega) &= \mathcal{F}_t \{ \mathcal{E}_y(t) \} (\omega). \end{aligned} \quad (3.23)$$

However, as further simplification, we can assume that we have only time-dependent, but not position-dependent polarization. This means that for each frequency component, both the x and the y component of the electric field are constituted of the same superposition of Gauss-Hermite modes, i.e.

$$A_{x,nm} = A_{y,nm} = A_{nm} \quad \forall n, m \in \mathbb{N}_0. \quad (3.24)$$

This allows us to write (3.22) in a more compact form:

$$\mathbf{E}(\mathbf{r}, t) = \frac{1}{2\pi} \int \mathbf{F}(\omega) \underbrace{\left(\sum_{nm} A_{nm} \text{GH}_{nm,\omega}(\mathbf{r}) \right)}_{M_\omega(\mathbf{r})} e^{-i\omega t} d\omega \quad (3.25)$$

with

$$\mathbf{F}(\omega) = \mathcal{F}_t \{ \mathcal{E}(t) \} (\omega) \quad (3.26)$$

and

$$\mathcal{E}(t) = \begin{pmatrix} \mathcal{E}_x(t) \\ \mathcal{E}_y(t) \\ 0 \end{pmatrix}. \quad (3.27)$$

3.3.3. Normalization

The function $\mathcal{E}(t)$ allows to specify the temporal shape of the pulse and determines also the total pulse energy of the driving field. However, it is not clear yet how to scale this function in order to obtain a given pulse energy E_{pulse} . To achieve this, we

make an ansatz using a positive real scaling prefactor \mathcal{E}_0 and a normalized temporal pulse shape $\hat{\mathcal{E}}(t)$:

$$\mathcal{E}(t) = \mathcal{E}_0 \hat{\mathcal{E}}(t) \quad \text{with} \quad \int |\hat{\mathcal{E}}(t)|^2 dt = 1 \quad (3.28)$$

The pulse energy is the power integrated over time, which in turn can be obtained from the intensity in the $z = 0$ plane:

$$\begin{aligned} E_{\text{pulse}} &= \int dt P(t) = \int dt \iint dx dy I(x, y, t) = \\ &= \int dt \iint dx dy \frac{cn\epsilon_0}{2} |\mathbf{E}(x, y, 0, t)|^2 = \\ &= \frac{cn\epsilon_0}{2} \iint dx dy \int dt |\mathbf{E}(x, y, 0, t)|^2 \end{aligned} \quad (3.29)$$

Using the Plancherel theorem, this becomes

$$\begin{aligned} E_{\text{pulse}} &= \frac{cn\epsilon_0}{2} \iint dx dy \frac{1}{2\pi} \int d\omega \left| \mathbf{F}(\omega) \left(\sum_{nm} A_{nm} \text{GH}_{nm,\omega}(\mathbf{r}) \right) \right|^2 = \\ &= \frac{cn\epsilon_0}{2} \frac{1}{2\pi} \int d\omega |\mathbf{F}(\omega)|^2 \iint dx dy \left| \sum_{nm} A_{nm} \text{GH}_{nm,\omega}(\mathbf{r}) \right|^2. \end{aligned} \quad (3.30)$$

Using the x - y -plane orthonormality of the Gauss-Hermite modes, this can be written as

$$E_{\text{pulse}} = \frac{cn\epsilon_0}{2} \frac{1}{2\pi} \int d\omega |\mathbf{F}(\omega)|^2 \cdot \sum_{nm} |A_{nm}|^2, \quad (3.31)$$

which is the same as, again using the Plancherel theorem,

$$\begin{aligned} E_{\text{pulse}} &= \frac{cn\epsilon_0}{2} \cdot \int dt |\mathcal{E}(t)|^2 \cdot \sum_{nm} |A_{nm}|^2 = \\ &= \frac{cn\epsilon_0}{2} \cdot |\mathcal{E}_0|^2 \cdot \sum_{nm} |A_{nm}|^2. \end{aligned} \quad (3.32)$$

Therefore, to get a driving field with a given pulse energy E_{pulse} , a given temporal pulse shape $\hat{\mathcal{E}}(t)$ and a spatial mode determined by A_{nm} , we can choose the scaling prefactor as

$$\mathcal{E}_0 = \sqrt{\frac{2E_{\text{pulse}}}{cn\epsilon_0 \cdot \sum_{nm} |A_{nm}|^2}} \quad (3.33)$$

3.3.4. Effects of the Gas Target

In the previous treatment, we assumed a constant refractive index n to account for a medium in which the driving field propagates. This is a very simple model that may not be sufficient in many cases. The gas target consists of neutral atoms, ionized atoms and a plasma of free electrons. How these three components affect the refractive index depends on their respective density, which in turn depends on the ionization fraction. The ionization fraction may not only be spatially dependent, but can also change over time.

In principle, to compute the refractive index of a mixture of different components, one needs to model the (linear) polarization response of this mixture. We can use the fact that the polarization density is additive:

$$\mathbf{P}_{\text{total}}(\mathbf{r}, t) = \mathbf{P}_{\text{neutral}}(\mathbf{r}, t) + \mathbf{P}_{\text{ions}}(\mathbf{r}, t) + \mathbf{P}_{\text{plasma}}(\mathbf{r}, t).$$

Inserting $\mathbf{P} = \chi \mathbf{E}$, where χ is the susceptibility, and cancelling \mathbf{E} , we get

$$\chi_{\text{total}}(\mathbf{r}, t) = \chi_{\text{neutral}}(\mathbf{r}, t) + \chi_{\text{ions}}(\mathbf{r}, t) + \chi_{\text{plasma}}(\mathbf{r}, t).$$

From the total susceptibility, we can easily obtain the total refractive index of the mixture:

$$\begin{aligned} n_{\text{total}}(\mathbf{r}, t) &= \sqrt{\epsilon_r \mu_r} \approx \sqrt{\epsilon_r} = \sqrt{1 + \chi_{\text{total}}(\mathbf{r}, t)} = \\ &= \sqrt{1 + \chi_{\text{neutral}}(\mathbf{r}, t) + \chi_{\text{ions}}(\mathbf{r}, t) + \chi_{\text{plasma}}(\mathbf{r}, t)} \end{aligned}$$

Here, we currently make the following assumptions:

- The contribution of the ionized atoms can be neglected, i.e. $\chi_{\text{ions}}(\mathbf{r}, t) = 0$. As the electrons of an ion are in general bound more tightly, the photon energy needed to induce a transition is significantly higher. As the susceptibility of an atom at a certain frequency is mainly determined by nearby resonances, it is justified to neglect the contribution of ionized atoms compared to the contribution of the neutral atoms for the usual regime (infrared driving field).
- The temporal dependence of the refractive index is neglected totally. This is only valid for very small ionization fractions where the plasma does not play a role, or if there is a constant background of ionized atoms that does not change within the time scale of one pulse. The Lewenstein formula (2.3) we used neglected the depletion of the ground state, which is also only justified if this is the case.
- The spatial dependence of the refractive index in direction transverse to the optical axis is neglected. As the driving beam is usually tightly focused to gain a high peak intensity, it only hits a small area of the gas jet. Within this area, the gas density can be assumed to be constant. However, the ionization fraction may change significantly over this length scale, so again we need to assume a small ionization fraction so that this effect does not play a role.

- The spatial dependence of the refractive index in direction of the optical axis is neglected. For this, we need to add the assumption that the gas density is constant in this direction, which is often not the case (compare figure 3 in [12]). Rather the gas density in z direction drops slowly to zero at the edges.

After making these assumptions, we can write the total refractive index as

$$n_t(\mathbf{r}, t) = n_t = \sqrt{1 + \chi_n + \chi_{\text{pl.bg.}}} \quad \forall \mathbf{r}, t$$

with the susceptibility χ_n of the neutral gas component and $\chi_{\text{pl.bg.}}$ of the plasma background. The susceptibility of the neutral gas can be computed from the refractive index of the pure gas for which there exists easily available data (e.g. [8]), using the formula

$$\chi_n = \epsilon_{r,n} - 1 = \sqrt{\epsilon_{r,n} \cdot I^2} - 1 \approx n_{\text{pure}}^2 - 1.$$

The susceptibility of the plasma background component depends on the plasma frequency ω_p as given by (see [9])

$$\chi_{\text{pl.bg.}} = \epsilon_{r,p} - 1 = -\frac{\omega_p^2}{\omega^2}, \quad (3.34)$$

where the plasma frequency is

$$\omega_p = \sqrt{\frac{\mathcal{N}_e e^2}{\epsilon_0 m_e}}$$

with the electron density \mathcal{N}_e .

A more rigorous treatment of the driving field is possible and also necessary for many applications, but will need some more effort, which is out of the scope of this thesis (for a short overview see chapter 5).

3.4. Build-up of the Harmonic Beam

In order to examine the build-up of harmonic radiation within the gas target, we start with the macroscopic Maxwell equations without free charges and currents:

$$\begin{aligned} \nabla \cdot \mathbf{D} &= 0, \\ \nabla \cdot \mathbf{B} &= 0, \\ \nabla \times \mathbf{E} &= -\frac{\partial \mathbf{B}}{\partial t}, \\ \nabla \times \mathbf{H} &= \frac{\partial \mathbf{D}}{\partial t}. \end{aligned} \quad (3.35)$$

In order to make use of these equations, we need to find proper relationships between the quantities \mathbf{E} and \mathbf{D} as well as between \mathbf{H} and \mathbf{B} . In linear media, these are

$$\begin{aligned} \mathbf{D} &= \epsilon_0 \epsilon_r \mathbf{E}, \\ \mathbf{B} &= \mu_0 \mu_r \mathbf{H}, \end{aligned} \quad (3.36)$$

where $\epsilon_r = 1 + \chi$ with the electric susceptibility χ . For HHG, the gas target is a non-linear medium however. To account for this, we need to add a term \mathbf{P}_{nl} for the polarization density due to the non-linear dipole response of the atoms:

$$\mathbf{D} = \epsilon_0 \epsilon_r \mathbf{E} + \mathbf{P}_{\text{nl}} \quad (3.37)$$

The polarization density can be written as $\mathbf{P}_{\text{nl}} = \mathcal{N} \cdot \mathbf{d}_{\text{nl}}$ with the atomic density \mathcal{N} and the atomic dipole moment \mathbf{d}_{nl} , which can be calculated using the Lewenstein model as described before.

For the magnetic field \mathbf{B} , we neglect the induced magnetization totally and assume $\mu_r = 1$.

Using these formula, we can now derive the wave equation. For this, we compute the following expression:

$$\begin{aligned} \nabla \times (\nabla \times \mathbf{E}) &\stackrel{(3.35)}{=} \nabla \times \left(-\frac{\partial \mathbf{B}}{\partial t} \right) \stackrel{(3.36)}{=} -\mu_0 \mu_r \frac{\partial}{\partial t} (\nabla \times \mathbf{H}) \stackrel{(3.35)}{=} \\ &\stackrel{(3.35)}{=} -\mu_0 \frac{\partial^2 \mathbf{D}}{\partial t^2} \stackrel{(3.37)}{=} -\epsilon_0 \epsilon_r \mu_0 \frac{\partial^2 \mathbf{E}}{\partial t^2} - \mu_0 \frac{\partial^2 \mathbf{P}_{\text{nl}}}{\partial t^2} \end{aligned}$$

For the left hand side, we can use the vector identity

$$\nabla \times (\nabla \times \mathbf{E}) = \nabla (\nabla \cdot \mathbf{E}) - \Delta \mathbf{E}.$$

Using (3.37), we get

$$\nabla \cdot \mathbf{E} = \frac{1}{\epsilon_0 \epsilon_r} (\nabla \cdot \mathbf{D} - \nabla \cdot \mathbf{P}_{\text{nl}}),$$

where we have $\nabla \cdot \mathbf{D} = 0$ according to (3.35) and the term $\nabla \cdot \mathbf{P}_{\text{nl}}$ can also be neglected compared to $\Delta \mathbf{E}$. Making this approximation, the left hand side becomes

$$\nabla \times (\nabla \times \mathbf{E}) = \nabla 0 - \Delta \mathbf{E} = -\Delta \mathbf{E}.$$

Together with the right hand side and using $\epsilon_0 \mu_0 = 1/c^2$ as well as the refractive index $n = \sqrt{\epsilon_r \cdot 1}$, we get the wave equation

$$\Delta \mathbf{E} = \frac{n^2}{c^2} \frac{\partial^2 \mathbf{E}}{\partial t^2} + \mu_0 \frac{\partial^2 \mathbf{P}_{\text{nl}}}{\partial t^2}. \quad (3.38)$$

To solve this equation, we use the ansatz

$$\mathbf{E}(\mathbf{r}, t) = \mathbf{U}(\mathbf{r}, t) \cdot e^{ik(\omega)z}, \quad (3.39)$$

with $k(\omega) = n(\omega) \cdot \omega/c$. Inserting this ansatz into the left hand side of the wave

equation yields

$$\begin{aligned}
\Delta \mathbf{E} &= \left(\frac{\partial^2}{\partial x^2} + \frac{\partial^2}{\partial y^2} + \frac{\partial^2}{\partial z^2} \right) (\mathbf{U} \cdot e^{ik(\omega)z}) = \\
&= \Delta_{\perp} \mathbf{U} \cdot e^{ik(\omega)z} + \frac{\partial}{\partial z} \left(\frac{\partial \mathbf{U}}{\partial z} \cdot e^{ik(\omega)z} + \mathbf{U} \cdot ik(\omega) e^{ik(\omega)z} \right) = \\
&= \Delta_{\perp} \mathbf{U} \cdot e^{ik(\omega)z} + \frac{\partial^2 \mathbf{U}}{\partial z^2} \cdot e^{ik(\omega)z} + 2 \cdot \frac{\partial \mathbf{U}}{\partial z} \cdot ik(\omega) e^{ik(\omega)z} + \mathbf{U} \cdot (ik(\omega))^2 e^{ik(\omega)z} = \\
&= \left(\Delta_{\perp} \mathbf{U} + \frac{\partial^2 \mathbf{U}}{\partial z^2} + 2ik(\omega) \cdot \frac{\partial \mathbf{U}}{\partial z} - k^2(\omega) \mathbf{U} \right) \cdot e^{ik(\omega)z} = \\
&= \left(\Delta_{\perp} \mathbf{U} + \frac{\partial^2 \mathbf{U}}{\partial z^2} + 2ik(\omega) \cdot \frac{\partial \mathbf{U}}{\partial z} - \frac{n^2 \omega^2}{c^2} \mathbf{U} \right) \cdot e^{ik(\omega)z}
\end{aligned}$$

The right hand side of the wave equation can be written as

$$\frac{n^2}{c^2} \frac{\partial^2 \mathbf{E}}{\partial t^2} + \mu_0 \frac{\partial^2 \mathbf{P}_{\text{nl}}}{\partial t^2} = \left(\frac{n^2}{c^2} \frac{\partial^2 \mathbf{U}}{\partial t^2} + \mu_0 e^{-ik(\omega)z} \cdot \frac{\partial^2 \mathbf{P}_{\text{nl}}}{\partial t^2} \right) \cdot e^{ik(\omega)z}.$$

Writing both sides together we get

$$\Delta_{\perp} \mathbf{U} + \frac{\partial^2 \mathbf{U}}{\partial z^2} + 2ik(\omega) \cdot \frac{\partial \mathbf{U}}{\partial z} - \frac{n^2 \omega^2}{c^2} \mathbf{U} = \frac{n^2}{c^2} \frac{\partial^2 \mathbf{U}}{\partial t^2} + \mu_0 e^{-ik(\omega)z} \cdot \frac{\partial^2 \mathbf{P}_{\text{nl}}}{\partial t^2}.$$

Finally, if we Fourier transform the equation in t , we get

$$\begin{aligned}
\left(\Delta_{\perp} + \frac{\partial^2}{\partial z^2} + 2ik(\omega) \cdot \frac{\partial}{\partial z} - \frac{n^2 \omega^2}{c^2} - \frac{n^2}{c^2} (i\omega)^2 \right) \mathbf{U}(\mathbf{r}, \omega) &= (i\omega)^2 \mathcal{F}_t \left\{ \mu_0 e^{-ik(\omega)z} \cdot \mathbf{P}_{\text{nl}} \right\} \\
\Rightarrow \left(\Delta_{\perp} + \frac{\partial^2}{\partial z^2} + 2ik(\omega) \cdot \frac{\partial}{\partial z} \right) \mathbf{U}(\mathbf{r}, \omega) &= -\omega^2 \mu_0 e^{-ik(\omega)z} \cdot \mathcal{F}_t \{ \mathbf{P}_{\text{nl}} \}
\end{aligned}$$

Due to the ansatz (3.39) which factors out the rapidly oscillating term of the electric field, the variation of \mathbf{U} in z direction can be assumed to be very slow, so we can neglect the $\partial^2/\partial z^2$ term. This approximation is known as the slowly-evolving-wave approximation (see [5]). Then, by dividing by $2ik(\omega)$, we arrive at the first-order propagation equation

$$\frac{\partial \mathbf{U}}{\partial z} = \frac{i}{2k(\omega)} \Delta_{\perp} \mathbf{U} + \frac{i\omega^2 \mu_0}{2k(\omega)} \cdot e^{-ik(\omega)z} \cdot \mathcal{F}_t \{ \mathbf{P}_{\text{nl}} \}. \quad (3.40)$$

For given initial conditions, this equation has a unique solution. We demand

$$\mathbf{E}(\mathbf{r}, \omega) \stackrel{!}{=} 0 \quad \text{for} \quad z = z_{\text{min}}, \quad (3.41)$$

as initial condition, because our ansatz together with the slowly-evolving wave approximation restricts us to propagation in positive z direction, and no harmonic radiation is generated before the starting position z_{min} of the gas target.

In order to account for absorption of the harmonics within the gas target, we can use a complex refractive index $n = n_r + i\kappa$ where n_r is the real refractive index and κ is related to the absorption coefficient α of the Beer-Lambert law $I = I_0 \exp(-\alpha z)$ as follows:

$$\alpha = \frac{4\pi\kappa}{\lambda} \quad (3.42)$$

There are several different ways in which the first-order propagation equation (3.40) can be solved numerically. One way would be to solve it iteratively using a simple finite difference method

$$U(x, y, z + \Delta z, \omega) \approx U(x, y, z, \omega) + \Delta z \cdot \frac{\partial U}{\partial z}.$$

However, we can also further simplify the equation before solving it. We arrive at a closed formula if the $\Delta_\perp U$ term of (3.40) is neglected – this term is responsible for the diffraction of the harmonic radiation within the gas target, so if the gas target is thin enough, it is a valid approximation to leave it out:

$$\frac{\partial U}{\partial z} = \frac{i\omega^2\mu_0}{2k(\omega)} \cdot e^{-ik(\omega)z} \cdot \mathcal{F}_t\{\mathbf{P}_{\text{nl}}\}. \quad (3.43)$$

As can be easily seen, for the given initial condition the solution is

$$U(x, y, z, \omega) = \int_{z_{\min}}^z dz' \frac{i\omega^2\mu_0}{2k(\omega)} \cdot e^{-ik(\omega)z'} \cdot \mathcal{F}_t\{\mathbf{P}_{\text{nl}}\}(x, y, z', \omega),$$

or, if we plug this into our ansatz,

$$\begin{aligned} \mathbf{E}(x, y, z, \omega) &= e^{ik(\omega)z} \int_{z_{\min}}^z dz' \frac{i\omega^2\mu_0}{2k(\omega)} \cdot e^{-ik(\omega)z'} \cdot \mathcal{F}_t\{\mathbf{P}_{\text{nl}}\}(x, y, z', \omega) = \\ &= e^{in\omega z/c} \int_{z_{\min}}^z dz' \frac{i\omega^2\mu_0 c}{2n\omega} \cdot e^{-in\omega z'/c} \cdot \mathcal{F}_t\{\mathcal{N} \cdot \mathbf{d}_{\text{nl}}\}(x, y, z', \omega) \\ &= \frac{i}{2} \frac{\omega}{c} \frac{1}{n} \mu_0 c^2 \cdot \mathcal{N} \cdot e^{in\omega z/c} \int_{z_{\min}}^z dz' \cdot e^{-in\omega z'/c} \cdot \mathcal{F}_t\{\mathbf{d}_{\text{nl}}\}(x, y, z', \omega) \end{aligned}$$

Using $c^2 = 1/(\mu_0\epsilon_0)$ we get

$$\mathbf{E}(x, y, z, \omega) = \frac{i}{2\epsilon_0 c} \frac{\omega \mathcal{N}}{n} \cdot e^{in\omega z/c} \int_{z_{\min}}^z dz' \cdot e^{-in\omega z'/c} \cdot \mathcal{F}_t\{\mathbf{d}_{\text{nl}}\}(x, y, z', \omega) \quad (3.44)$$

which can be computed e.g. using the trapezoidal rule for numerical integration.

An alternative approach to solving the first-order propagation equation (3.40) without neglecting the Δ_\perp term would be to do a two-dimensional spatial Fourier transformation on the x and y coordinates so that we get

$$\frac{\partial \tilde{U}}{\partial z} = \frac{i}{2k(\omega)} ((ik_x)^2 + (ik_y)^2) \tilde{U} + \frac{i\omega^2\mu_0}{2k(\omega)} \cdot e^{-ik(\omega)z} \cdot \mathcal{F}_{xy}\{\mathcal{F}_t\{\mathbf{P}_{\text{nl}}\}\}. \quad (3.45)$$

where $\tilde{U} := \mathcal{F}_{xy} \{U\}$. This can be written as

$$\frac{\partial \tilde{U}}{\partial z} = A \cdot \tilde{U} + B(z)$$

with the definitions

$$A(k_x, k_y, \omega) := \frac{i}{2k(\omega)} ((ik_x)^2 + (ik_y)^2)$$

$$B(k_x, k_y, \omega; z) := \frac{i\omega^2 \mu_0}{2k(\omega)} \cdot e^{-ik(\omega)z} \cdot \mathcal{F}_{xy} \{ \mathcal{F}_t \{ \mathbf{P}_{nl} \} \}.$$

For the initial conditions given previously, this differential equation has the solution

$$\tilde{U}(k_x, k_y, z, \omega) = e^{A(k_x, k_y, \omega) \cdot z} \int_{z_{\min}}^z dz' B(k_x, k_y, \omega; z') \cdot e^{-A(k_x, k_y, \omega) \cdot z'}$$

as can be seen easily by substituting the term into the equation. This approach would need some more computing power, as a Fourier transformation must be calculated for each value of z' , but it would be easy to implement and allow us to account for the diffraction of the harmonics within the gas target.

3.5. Far Field Distribution of the Harmonic Radiation

Using the far-field approximation, we want to compute the harmonic field distribution on a far-away plane given the field distribution right after the gas target. According to (7.27) and (7.29) from [20], the far field can be calculated using

$$U(x, y, z) = -2\pi i (kz/r) \frac{e^{ikr}}{r} F(kx/r, ky/r) \quad (3.46)$$

with the definitions

$$r = \sqrt{x^2 + y^2 + z^2}$$

and

$$F(k_x, k_y) = \mathcal{F}_{xy} \{U(x, y, 0)\} (k_x, k_y),$$

where the harmonic radiation $U(x, y, z)$ is assumed to be given at $z = 0$.

However, if the field is given in a plane $z = z_t$ due to the position of the target, we must write down these equations in a shifted coordinate system and transform them back to the conventional one, and obtain

$$U(x, y, z) = -2\pi i \frac{k(z - z_t) \cdot e^{ikr}}{r^2} F(kx/r, ky/r) \quad (3.47)$$

$$r = \sqrt{x^2 + y^2 + (z - z_t)^2} \quad (3.48)$$

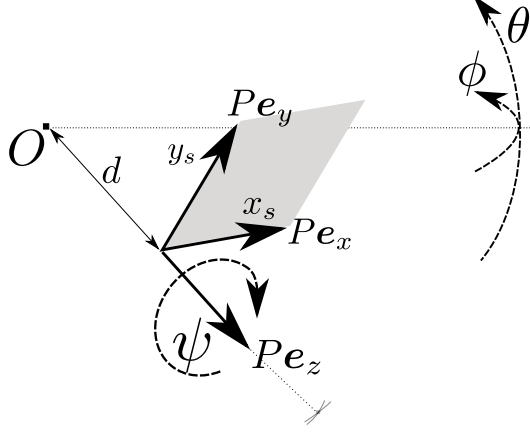


Figure 3.1.: Orientation and Position of Screen Plane

$$F(k_x, k_y) = \mathcal{F}_{xy} \{U(x, y, z_t)\} (k_x, k_y). \quad (3.49)$$

Now, we want to compute the positions (x, y, z) corresponding to screen coordinates (x_s, y_s) . For this, we assume that the screen is at distance d from the origin and parallel to the x - y -plane. To be able to model arbitrary oriented screen planes, one can optionally rotate the screen around the origin using a rotation matrix

$$P = R_x(\theta)R_y(\phi)R_z(\psi),$$

which is chosen so that Pe_x and Pe_y span the screen plane (see figure 3.1). Here, $R_i(\alpha)$ denotes a rotation matrix rotating around the i -th axis with an angle of α .

Then, the transformation from screen coordinates to conventional coordinates is

$$\begin{pmatrix} x \\ y \\ z \end{pmatrix} = P \begin{pmatrix} x_s \\ y_s \\ d \end{pmatrix}. \quad (3.50)$$

Using equations (3.47) to (3.49) and (3.50), we can now approximate the harmonic field at a point (x_s, y_s) of the screen.

3.6. Fluorescent Screen

Often, a fluorescent screen is used in experiments to make the harmonic radiation visible. If the wavelength-dependent conversion efficiency of the screen material is known, it is easy to model the light conversion process.

From the previous considerations, we already can compute the complex electric field amplitude $\mathbf{E}_h(\mathbf{r} \in P, \omega)$ of the harmonics within a far away screen plane P . The spectral intensity of the harmonic radiation can be calculated using

$$I_h(\mathbf{r}, \omega) = \frac{\epsilon_0 c}{2} |\mathbf{E}(\mathbf{r}, \omega)|^2. \quad (3.51)$$

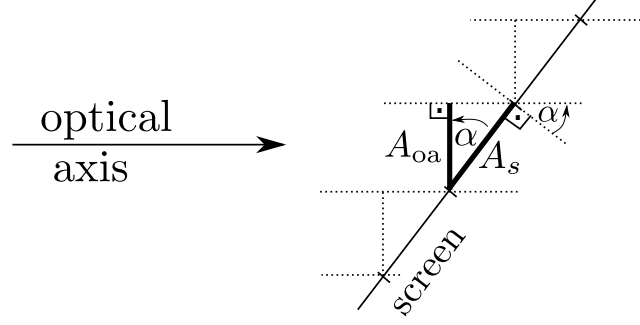


Figure 3.2.: Ratio between unit surfaces

This can also be written as spectral energy density $N(\omega)\hbar\omega$ per unit time t and per unit surface A_{0a} which is perpendicular to the optical axis, where $N(\omega)$ is a spectral number density of photons:

$$I_h = \frac{N(\omega) \cdot \hbar\omega}{A_{0a}t}$$

The conversion efficiency $\eta(\omega)$ of the screen material is the fraction of incoming photons that are converted by the fluorescence process to photons with an angular frequency of ω_f . Using this, we can write the spectral radiant exitance of the converted light on the screen, i.e. the power that is emitted per unit surface A_s of the screen, as

$$M_f = \frac{\eta(\omega)N(\omega) \cdot \hbar\omega_f}{A_s t}.$$

As can be seen in figure 3.2, the unit surfaces A_{0a} and A_s are related as

$$\frac{A_{0a}}{A_s} = \cos \alpha,$$

where α is the angle between the optical axis and the screen plane normal, so that we can write

$$M_f = \eta(\omega) \frac{\omega_f}{\omega} \frac{A_{0a}}{A_s} \cdot \frac{n \cdot \hbar\omega}{A_{0a}t} = \eta(\omega) \frac{\omega_f}{\omega} \cos \alpha \cdot I_h$$

So, plugging in (3.51), we get a spectral radiant exitance of

$$\begin{aligned} M_f(\mathbf{r}, \omega) &= \eta(\omega) \frac{\omega_f}{\omega} \cos \alpha \cdot \frac{\epsilon_0 c}{2} |\mathbf{E}(\mathbf{r}, \omega)|^2 = \\ &= \frac{\epsilon_0 c \omega_f \cos \alpha}{2} \cdot \frac{\eta(\omega)}{\omega} |\mathbf{E}(\mathbf{r}, \omega)|^2 \end{aligned} \tag{3.52}$$

3.7. Diffraction Grating

For experiments that use a grating for analyzing XUV radiation or experiments that use an intra-cavity grating for XUV output coupling from enhancement cavities, it

is necessary to simulate the effect of a diffraction grating on the observed XUV far field distribution.

To simulate a diffraction grating, several things have to be considered. First, there are reflective and transmissive gratings. Second, these gratings can be blazed, i.e. the lines have a 3D structure that allows optimizing the reflectivity for a certain direction. Third, the grating efficiency is usually wavelength-dependent. Moreover, it can be polarization-dependent.

For the calculations, the following assumptions and simplifications are made:

- The grating is transmissive. This assumption can be removed easily after the calculation is done as transmissive and reflective gratings behave very similar.
- The lines have no structure, i.e. the grating is not blazed nor do the lines have inhomogenous transmission or phase shift.
- The wavelength dependence of the transmission is neglected.
- The incoming light, and therefore the diffracted light, is assumed to be linearly polarized in direction of the grating lines.

Using these assumptions, we will first derive a three-dimensional grating equation for an incident plane wave. Then we will consider the case of an arbitrarily positioned and oriented grating. After that, we can treat a general monochromatic field distribution by decomposing it into plane waves. This also allows to treat non-monochromatic radiation by repeating the procedure for each frequency component. Finally, a far field approximation can be applied to get the field within a far away plane after the grating.

3.7.1. 3D Grating Equation

We choose a 3D coordinate system so that the grating lies within the x - y -plane, and we assume the grating lines to be parallel to the y direction. We consider an incoming plane wave with wavenumber \mathbf{k} , $k_z > 0$. We use the following ansatz for the complex electric field E :

$$E(\mathbf{r}, t) = U(\mathbf{r})e^{-i\omega t}$$

As we assume linear polarization, we only consider one component of the full electric field vector \mathbf{E} . The incoming plane wave is then described by

$$U_i(\mathbf{r}) = e^{i\mathbf{k} \cdot \mathbf{r}} e^{i\phi_0}, \quad (3.53)$$

where $e^{i\phi_0}$ is a constant phase factor and $k = |\mathbf{k}|$ is related to ω according to the dispersion relation.

Now, we only concentrate on the x - y -plane. The incoming wave inside this plane is described by

$$U_{i,2D}(x, y) = U_i(\mathbf{r} = (x, y, 0)) = e^{i(k_x x + k_y y)} e^{i\phi_0}.$$

At the positions of the grating lines, the light can pass, while light is blocked between the lines. This can be expressed using a spatially dependent transmission coefficient

$$T(x, y) = \sum_n \delta(x - nd),$$

where d is the spacing of the lines. The light diffracted by the grating directly after the x - y plane can be written as

$$U_{d,2D}(x, y) = U_{i,2D}(x, y) \cdot T(x, y). \quad (3.54)$$

Using a two-dimensional spatial Fourier transform and its inverse, formula (3.54) can be written as

$$\begin{aligned} U_{d,2D}(x, y) &= \mathcal{F}_{xy}^{-1} \{ \mathcal{F}_{xy} \{ U_{i,2D} \cdot T \} \} = \\ &= \mathcal{F}_{xy}^{-1} \{ \mathcal{F}_{xy} \{ U_{i,2D} \} (k'_x, k'_y) * \mathcal{F}_{xy} \{ T \} (k'_x, k'_y) \}, \end{aligned}$$

where $*$ denotes convolution. Inserting the Fourier transforms

$$\begin{aligned} \mathcal{F}_{xy} \{ U_{i,2D} \} (k'_x, k'_y) &= e^{i\phi_0} (2\pi)^2 \delta(k'_x - k_x) \delta(k'_y - k_y) \\ \mathcal{F}_{xy} \{ T \} (k'_x, k'_y) &= \sum_m \delta(k'_x - m \cdot 2\pi/d) \end{aligned}$$

into this expression we obtain

$$\begin{aligned} U_{d,2D}(x, y) &= \\ &= \mathcal{F}_{xy}^{-1} \left(e^{i\phi_0} (2\pi)^3 \delta(k'_x - k_x) \delta(k'_y - k_y) * \sum_m \delta(k'_x - m \cdot 2\pi/d) \right) \\ &= \sum_m \mathcal{F}_{xy}^{-1} \left(e^{i\phi_0} (2\pi)^2 \delta(k'_x - k_x) \delta(k'_y - k_y) * \delta(k'_x - m \cdot 2\pi/d) \right) \\ &= \sum_m \mathcal{F}_{xy}^{-1} \left(e^{i\phi_0} (2\pi)^2 \delta(k'_x - m \cdot 2\pi/d - k_x) \delta(k'_y - k_y) \right) \\ &= \sum_m e^{i((k_x - m \cdot 2\pi/d)x + k_y y)} e^{i\phi_0} = \\ &= \sum_m e^{i(k'_{x,m}x + k'_y y)} e^{i\phi_0} \end{aligned}$$

This is a superposition of plane waves within the x - y -plane, with wavenumbers

$$(k'_{x,m}, k'_y) = (k_x - m \cdot 2\pi/d, k_y) = (k_x, k_y) - m \cdot 2\pi/d \cdot \mathbf{e}_x. \quad (3.55)$$

As we know that the light that passes the grating still has the same wavelength, we can easily reconstruct the 3D field from the 2D field by completing the wave vector with $k'_{z,m} = \sqrt{k^2 - k'^2_{x,m} - k'^2_y}$. Then we get the 3D field of the diffracted light

$$U_d(\mathbf{r}) = \sum_m e^{i\mathbf{k}'_m \mathbf{r}} e^{i\phi_0} \quad \text{with} \quad \mathbf{k}'_m = \left(k'_{x,m}, k'_y, \sqrt{k^2 - k'^2_{x,m} - k'^2_y} \right)^\top,$$

where $k'_{z,m}$ is chosen such that $|\mathbf{k}'_m| = |\mathbf{k}|$ and $k'_{z,m} > 0$. The summation index m is the diffraction order.

In the following, we will consider only light for one diffraction order and therefore omit the summation:

$$U_{d,m}(\mathbf{r}) = e^{i\mathbf{k}'_m \mathbf{r}} e^{i\phi_0} \quad (3.56)$$

So what happens when a plane wave passes a grating can be summarized as follows (see figure 3.3):

- For a given diffraction order, the light that passes the grating is a plane wave too.
- If we look at the wavenumber \mathbf{k} of the incident and \mathbf{k}' of the diffracted plane wave, the components parallel to the grating are related as²

$$\mathbf{k}'_{\parallel} = \mathbf{k}_{\parallel} - \Delta\mathbf{k}_{\parallel}$$

where $\Delta\mathbf{k}_{\parallel}$ is parallel to the grating and perpendicular to the grating lines and the norm is given by

$$|\Delta\mathbf{k}_{\parallel}| = m \cdot 2\pi/d$$

- The component of \mathbf{k}' that is perpendicular to the grating plane must be chosen so that $|\mathbf{k}'| = |\mathbf{k}|$, i.e.

$$k'_{\perp} = \sqrt{\mathbf{k}^2 - \mathbf{k}_{\parallel}^2}$$

- At the origin $\mathbf{r} = 0$, the complex field amplitude of the incident plane wave and of the diffracted plane wave is the same³:

$$U_d(\mathbf{r} = 0) = U_i(\mathbf{r} = 0) = e^{i\phi_0}$$

3.7.2. Arbitrarily Positioned and Oriented Grating

Now we consider a grating that is at an arbitrary position in space and is arbitrarily rotated (see figure 3.4). The position at which the z axis intersects the grating plane is called z_0 . The orientation of the grating is described by a rotation matrix

$$G = R_x(\theta)R_y(\phi)R_z(\psi)$$

which is chosen so that $G\mathbf{e}_x$ and $G\mathbf{e}_y$ span the grating plane and $G\mathbf{e}_y$ is parallel to the grating lines. Here, $R_i(\alpha)$ denotes a rotation matrix rotating around the i -th axis with an angle of α .

As we want to apply a far field approximation later, we will also choose a coordinate

²compare to (3.55)

³compare to (3.53) and (3.56)

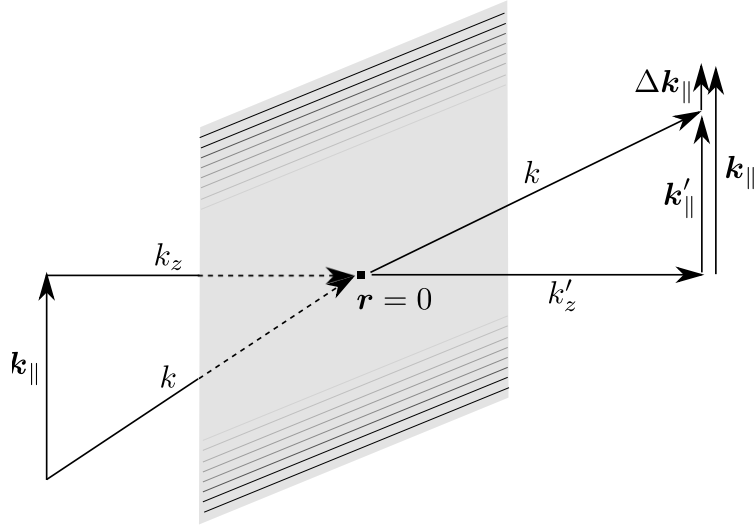


Figure 3.3.: 3D Grating Equation

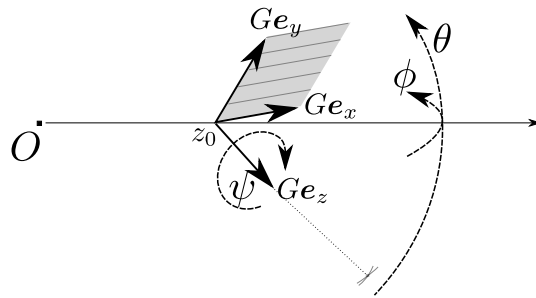


Figure 3.4.: Orientation and position of grating

system $\{D\mathbf{e}_x, D\mathbf{e}_y, D\mathbf{e}_z\}$ which is described by a rotation matrix D . This coordinate system can be chosen later so that the diffracted beam for a given diffraction order is collimated around the $D\mathbf{e}_z$ axis.

In contrast to the previous calculation, where we calculated the diffracted plane wave from the incoming plane wave, we will do it the other way round here: We start with a diffracted plane wave given in the coordinate system defined by D and want to calculate the corresponding incoming plane wave in the conventional coordinate system. The reason is that this is more convenient to implement, as will become apparent later.

The wave vector of the diffracted plane wave in D coordinates is called $\tilde{\mathbf{k}}$. First, we need to calculate the components of the wave vector in grating coordinates G , so that we can apply $\Delta\mathbf{k}_\parallel$ as described previously:

$$\mathbf{k}_{d,G} = G^\top D \tilde{\mathbf{k}} \quad (3.57)$$

Then, we add back the $\Delta\mathbf{k}_\parallel$ that was subtracted at the grating to get the in-plane components of the wave vector of the incident plane wave:

$$\mathbf{k}_{i\parallel,G} = \mathbf{k}_{d\parallel,G} + \Delta\mathbf{k}_\parallel \quad \text{with} \quad \Delta\mathbf{k}_\parallel = (m \cdot 2\pi/d, 0)^\top \quad (3.58)$$

After that, we can reconstruct the component of the wave vector that is perpendicular to the grating plane analogously to what we did when deriving the 3D grating equation:

$$k_{i\perp,G} = \sqrt{k^2 - \mathbf{k}_{i\parallel,G}^2} \quad (3.59)$$

Now that we have $\mathbf{k}_{i\parallel,G}$ and $k_{i\perp,G}$ we know the full wave vector $\mathbf{k}_{i,G}$ of the incident plane wave in grating coordinates. Finally, we can compute the coordinates of this wave vector in conventional coordinates:

$$\mathbf{k}_i = G \mathbf{k}_{i,G} \quad (3.60)$$

Using (3.57) to (3.60), we know how the wave vector \mathbf{k}_i of incident and $\tilde{\mathbf{k}}$ of the diffracted plane wave relate. To fully describe a plane wave, it is however also necessary to know the phases. For the incident plane wave, we use the ansatz

$$U_i(\mathbf{r}) = e^{i\mathbf{k} \cdot \mathbf{r}} e^{i\phi_0}, \quad (3.61)$$

while for the diffracted plane wave we write, using diffracted beam coordinates \mathbf{r}_D ,

$$\tilde{U}(\mathbf{r}_D) = e^{i\tilde{\mathbf{k}} \cdot \mathbf{r}_D} e^{i\tilde{\phi}_0}. \quad (3.62)$$

Now we use the fact that at the origin of the grating coordinate system, both waves must have the same phase (see 3.7.1). In conventional coordinates, the origin of the grating coordinate system lies at $z_0\mathbf{e}_z$. In diffracted beam coordinates, it lies at $\mathbf{0}$. So we demand

$$U_i(z_0\mathbf{e}_z) \stackrel{!}{=} \tilde{U}(\mathbf{0})$$

$$\Rightarrow e^{i\mathbf{k} \cdot z_0 \mathbf{e}_z} e^{i\phi_0} = e^{i\tilde{\mathbf{k}} \cdot \mathbf{0}} e^{i\tilde{\phi}_0}$$

From this, we can get a relation between the phase ϕ_0 of the incident plane wave and $\tilde{\phi}_0$ of the diffracted plane wave:

$$e^{i\tilde{\phi}_0} = e^{ik_z z_0} e^{i\phi_0}. \quad (3.63)$$

3.7.3. Decomposition of the Incident Field into Plane Waves

Our goal is to compute what the grating does to the harmonic radiation coming from the gas target, as calculated in chapter 3.4. For this, we can decompose the incoming harmonic radiation into its frequency components and then into plane waves, which we can handle with the formulas provided in chapter 3.7.2.

Provided that the incoming electric field $E_i(\mathbf{r}, t)$ is given, the decomposition into frequency components is given by a time-domain inverse Fourier transform

$$E_i(\mathbf{r}, t) = \frac{1}{2\pi} \int d\omega E_i(\mathbf{r}, \omega) e^{-i\omega t}. \quad (3.64)$$

In the following we restrict ourselves to one frequency component ω and set $U_i(\mathbf{r}) := E_i(\mathbf{r}, \omega)$. This can be further decomposed into plane waves $\exp(i(k_x x + k_y y + k_z z))$ with wave numbers $\mathbf{k} = (k_x, k_y, k_z)^\top$, where $|\mathbf{k}| = k(\omega)$ is given by the dispersion relation. This decomposition can be written as

$$U_i(\mathbf{r}) = U_i(x, y, z) = \iint F^{3D}(k_x, k_y) e^{i(k_x x + k_y y + k_z z)} dk_x dk_y \quad (3.65)$$

with $k_z = \sqrt{k^2(\omega) - k_x^2 - k_y^2}$ and coefficients $F^{3D}(k_x, k_y)$.

Now, assuming that $U_i(\mathbf{r})$ is given in an x - y -plane behind the gas target at $z = z_t$, we can also do a two-dimensional Fourier expansion of $U_i(x, y, z = z_t)$:

$$U_i(x, y, z_t) = (2\pi)^{-2} \iint F(k_x, k_y) e^{i(k_x x + k_y y)} dk_x dk_y, \quad (3.66)$$

where the coefficients $F(k_x, k_y)$ can be computed easily with a Fourier transform:

$$F(k_x, k_y) = \mathcal{F}_{xy} \{U_i(x, y, z_t)\} \quad (3.67)$$

As both (3.65) and (3.66) should yield the same result for $z = z_t$, we get the relation

$$(2\pi)^{-2} F(k_x, k_y) = F^{3D}(k_x, k_y) \cdot e^{ik_z z_t}.$$

From this, we obtain the plane wave coefficients

$$F^{3D}(k_x, k_y) = (2\pi)^{-2} F(k_x, k_y) \cdot e^{-ik_z z_t}. \quad (3.68)$$

Now that we have decomposed the incident radiation into plane waves with known coefficients $F^{3D}(k_x, k_y) = A \cdot e^{i\phi_0}$, we can apply the grating to the individual plane

waves.

The coefficients transform according to (3.63) as

$$F^{3D}(k_x, k_y) = A \cdot e^{i\phi_0} \mapsto A \cdot e^{i\tilde{\phi}_0} = F^{3D}(k_x, k_y) e^{ik_z z_0},$$

and the plane wave according to (3.61) and (3.62) as

$$e^{i(k_x x + k_y y + k_z z)} \mapsto e^{i\tilde{\mathbf{k}} \cdot \mathbf{r}_D}.$$

Modifying equation (3.65) accordingly yields the harmonic field after the grating

$$\begin{aligned} U_d(\mathbf{r}_D) &= \iint F^{3D}(k_x, k_y) e^{ik_z z_0} e^{i\tilde{\mathbf{k}} \cdot \mathbf{r}_D} dk_x dk_y \stackrel{(3.68)}{=} \\ &\stackrel{(3.68)}{=} \iint (2\pi)^{-2} F(k_x, k_y) e^{-ik_z z_t} e^{ik_z z_0} e^{i\tilde{\mathbf{k}} \cdot \mathbf{r}_D} dk_x dk_y \end{aligned}$$

From this, we can compute the field in the plane with $z_D = 0$:

$$U_d(x_D, y_D, z_D = 0) = \iint (2\pi)^{-2} F(k_x, k_y) \cdot e^{ik_z(z_0 - z_t)} e^{i(\tilde{k}_x x_D + \tilde{k}_y y_D)} dk_x dk_y$$

The term $e^{i(\tilde{k}_x x_D + \tilde{k}_y y_D)}$ looks like the exponential term of a Fourier transformation, however the integration variables k_x and k_y do not fit. Using a variable transformation $(k_x, k_y) \mapsto (\tilde{k}_x, \tilde{k}_y)$, we can rewrite the integral as a two-dimensional inverse Fourier transform:

$$\begin{aligned} U_d(x_D, y_D, z_D = 0) &= \\ &= \iint (2\pi)^{-2} F(k_x, k_y) \cdot e^{ik_z(z_0 - z_t)} e^{i(\tilde{k}_x x_D + \tilde{k}_y y_D)} \left| J(\tilde{k}_x, \tilde{k}_y) \right| d\tilde{k}_x d\tilde{k}_y = \\ &= \mathcal{F}_{xy}^{-1} \left\{ F(k_x, k_y) \cdot e^{ik_z(z_0 - z_t)} \left| J(\tilde{k}_x, \tilde{k}_y) \right| \right\} \end{aligned} \quad (3.69)$$

Here, $J(\tilde{k}_x, \tilde{k}_y)$ is the Jacobi matrix of the transformation. Its value is

$$J = \mathbb{1}_{2 \times 3} G \begin{pmatrix} \frac{\partial c_1}{\partial \tilde{k}_x} & \frac{\partial c_1}{\partial \tilde{k}_y} \\ \frac{\partial c_2}{\partial \tilde{k}_x} & \frac{\partial c_2}{\partial \tilde{k}_y} \\ -\frac{c_1 \frac{\partial c_1}{\partial k_x} + c_2 \frac{\partial c_2}{\partial k_x}}{\sqrt{k^2 - c_1^2 - c_2^2}} & -\frac{c_1 \frac{\partial c_1}{\partial k_y} + c_2 \frac{\partial c_2}{\partial k_y}}{\sqrt{k^2 - c_1^2 - c_2^2}} \end{pmatrix} \quad (3.70)$$

with the definitions

$$c_1 := b_{11} \tilde{k}_x + b_{12} \tilde{k}_y + b_{13} \tilde{k}_z + m \cdot 2\pi/d$$

$$\begin{aligned}
&\Rightarrow \frac{\partial c_1}{\partial \tilde{k}_x} = b_{11} - b_{13} \frac{\tilde{k}_x}{\tilde{k}_z} \\
&\Rightarrow \frac{\partial c_1}{\partial \tilde{k}_y} = b_{12} - b_{13} \frac{\tilde{k}_y}{\tilde{k}_z} \\
&c_2 := b_{21} \tilde{k}_x + b_{22} \tilde{k}_y + b_{23} \tilde{k}_z \\
&\Rightarrow \frac{\partial c_2}{\partial \tilde{k}_x} = b_{21} - b_{23} \frac{\tilde{k}_x}{\tilde{k}_z} \\
&\Rightarrow \frac{\partial c_2}{\partial \tilde{k}_y} = b_{22} - b_{23} \frac{\tilde{k}_y}{\tilde{k}_z} \\
&\begin{pmatrix} b_{11} & b_{12} & b_{13} \\ b_{21} & b_{22} & b_{23} \end{pmatrix} := \mathbb{I}_{2 \times 3} G^\top D \\
&\tilde{k}_z = \sqrt{k^2 - \tilde{k}_x^2 - \tilde{k}_y^2}
\end{aligned}$$

3.7.4. Far-Field Approximation for a Flat Screen

We can safely assume that one frequency component of the incident beam is still collimated after it is diffracted by the grating, but in a different direction. If we choose the diffracted beam coordinate system in a way so that the diffracted beam is collimated around the z axis of this coordinate system, we can again apply the far-field approximation to obtain the field at a screen plane that is sufficiently far away from the grating.

For this, we assume that (x_D, y_D, z_D) is the position of a point in the screen plane where we want to compute the field, given in the diffracted beam coordinate system. Then, in analogy to (3.46), we get the far field

$$U_{\text{ff}}(x_D, y_D, z_D) = -2\pi i (kz_D/r) \frac{e^{ikr}}{r} F_{\text{ff}}(kx_D/r, ky_D/r) \quad (3.71)$$

with the radius

$$r = \sqrt{x_D^2 + y_D^2 + z_D^2}$$

and the two-dimensional Fourier transform

$$\begin{aligned}
F_{\text{ff}}(\tilde{k}_x, \tilde{k}_y) &= \mathcal{F}_{xy} \{U_d(x_D, y_D, z_D = 0)\}(\tilde{k}_x, \tilde{k}_y) \stackrel{(3.69)}{=} \\
&\stackrel{(3.69)}{=} \mathcal{F}_{xy} \left\{ \mathcal{F}_{xy}^{-1} \left\{ F(k_x, k_y) \cdot e^{ik_z(z_0 - z_t)} \left| J(\tilde{k}_x, \tilde{k}_y) \right| \right\} \right\} = \\
&= F(k_x, k_y) \cdot e^{ik_z(z_0 - z_t)} \left| J(\tilde{k}_x, \tilde{k}_y) \right|
\end{aligned} \quad (3.72)$$

It is important to choose the diffracted beam coordinate system, i.e. the matrix D , such that the diffracted beam is collimated around the $D\mathbf{e}_z$ direction, otherwise the far-field approximation is not valid. We assume that the incoming harmonic

radiation is collimated around the z axis. Therefore we look at an incoming plane wave that propagates along the optical axis, i.e. has a wave vector $k\mathbf{e}_z$, and compute the diffracted plane wave. This can be done by applying (3.57) to (3.60) in reverse order. In conventional coordinates, this plane wave is diffracted as

$$k\mathbf{e}_z \mapsto k\mathbf{d}_z \quad \text{with} \quad \mathbf{d}_z := G \begin{pmatrix} G_{31} - m\frac{2\pi}{d}/k \\ G_{32} \\ \sqrt{1 - (G_{31} - m\frac{2\pi}{d}/k)^2 - G_{32}^2} \end{pmatrix}. \quad (3.73)$$

Now we can choose any unitary matrix $D = (\mathbf{d}_x, \mathbf{d}_y, \mathbf{d}_z)$ to get a valid diffracted beam coordinate system. A convenient choice for implementing would be $\mathbf{d}_y := G\mathbf{e}_y$ and $\mathbf{d}_x := \mathbf{d}_y \times \mathbf{d}_z$.

To compute the harmonic field at a screen plane after the grating, we also need a way to compute the positions (x_D, y_D, z_D) corresponding to screen coordinates (x_s, y_s) . For this we assume like in chapter 3.5 that the screen is at a distance d from the origin of the grating coordinate system, and is rotated around this position with a rotation matrix

$$P = R_x(\theta)R_y(\phi)R_z(\psi),$$

which is chosen so that GPe_x and GPe_y span the screen plane, i.e. the angles θ , ϕ and ψ are relative to the grating coordinate system. Here, $R_i(\alpha)$ again denotes a rotation matrix rotating around the i -th axis with an angle of α .

Then, the transformation from screen coordinates to diffracted beam coordinates is

$$\begin{pmatrix} x_D \\ y_D \\ z_D \end{pmatrix} = D^\top GP \begin{pmatrix} x_s \\ y_s \\ d \end{pmatrix}. \quad (3.74)$$

3.7.5. Summary and Implementation

Now, we have everything together that we need to compute the harmonic radiation on a far away screen plane after a grating was passed:

- We decompose the incoming harmonic radiation into its frequency components $U_i(x, y, z_t)$ according to (3.64).
- We apply a two-dimensional Fourier transform on the plane according to (3.67) to get the coefficients $F(k_x, k_y)$.
- We use the far-field approximation (3.71) to get the harmonic radiation on the screen plane. For this, we need to
 - choose a matrix D with the help of equation (3.73).
 - compute the positions of the screen points (x_D, y_D, z_D) using equation (3.74).

- evaluate the F_{ff} term using (3.72), which involves converting $\tilde{\mathbf{k}}$ to \mathbf{k} with (3.57) to (3.60) and computing the Jacobi determinant with (3.70).

For implementing this procedure, the electric field has to be discretized in the input plane. The coefficients $F(k_x, k_y)$ can then be computed with a Fast Fourier Transform (FFT).

Also, the output plane must be discretized. This discretization can be converted to a grid of points (x_D, y_D, z_D) where the far-field approximation should be applied. This grid determines the points $(\tilde{k}_x, \tilde{k}_y) = (kx_D/r, ky_D/r)$ in the reciprocal space at which F_{ff} must be evaluated. After these points are converted to points (k_x, k_y) , we can do an interpolation in the $F(k_x, k_y)$ array that was computed with a FFT. This is the reason why we chose to compute \mathbf{k} from $\tilde{\mathbf{k}}$ and not the other way round, as it is easier to implement interpolation in data given on a rectangular grid.

4. Theoretical and Experimental Applications

4.1. Single Atom Dipole Response – Comparison with the TDSE

In order to verify the implemented model for the single atom dipole response, we compare the obtained dipole spectra with dipole spectra from other sources.

It is difficult to compare to experimental data, because in experiments there are always many atoms involved and the measured spectrum is a superposition of the individual dipole responses. Therefore, the comparison is done with theoretical data obtained from a more accurate (but also computationally more expensive) model.

Le et al. produced dipole spectra for xenon solving the three-dimensional time-dependent Schrödinger equation in single-active electron approximation in [16]. For this, they used an effective atomic potential, while the version of the Lewenstein model implemented here uses a simple hydrogen-like potential. They simulated the dipole response of a xenon atom to a \cos^2 driving pulse with a FWHM of 7.8 fs, a central wavelength of 1600 nm and a peak intensity of $5 \cdot 10^{13}$ W/cm². Moreover, they also did a calculation with the Lewenstein model, using dipole matrix elements corresponding to the same atomic potential as used for the TDSE calculation.

Figure 4.1 shows the results they obtained, in comparison to the results from the Lewenstein model implemented here. It can be seen that there is good agreement between all three curves at high frequencies, which verifies that code implemented for this thesis is working correctly.

For lower harmonics, the two curves of Le et al. differ significantly. The reason for this is that the approximations made in the Lewenstein model are not fulfilled well in this regime. As mentioned before, it does not describe well lower harmonics that are near the ionization potential (which is 12.13 eV for xenon), because these harmonics are produced by electron trajectories that have a low kinetic energy and are nearer to the core so that assumption of free propagation breaks down, as the electron starts to feel the long range Coulomb potential of the core. This is discussed in detail in [16], where also an extension of the Lewenstein model is presented which attempts to fix this shortcoming. Even if the model does not describe low harmonics well quantitatively, it can be used for qualitative considerations in this regime nonetheless. In many applications, it is most important that phase dependence of the harmonics is modelled correctly, while the absolute frequency-dependent intensity has less significance.

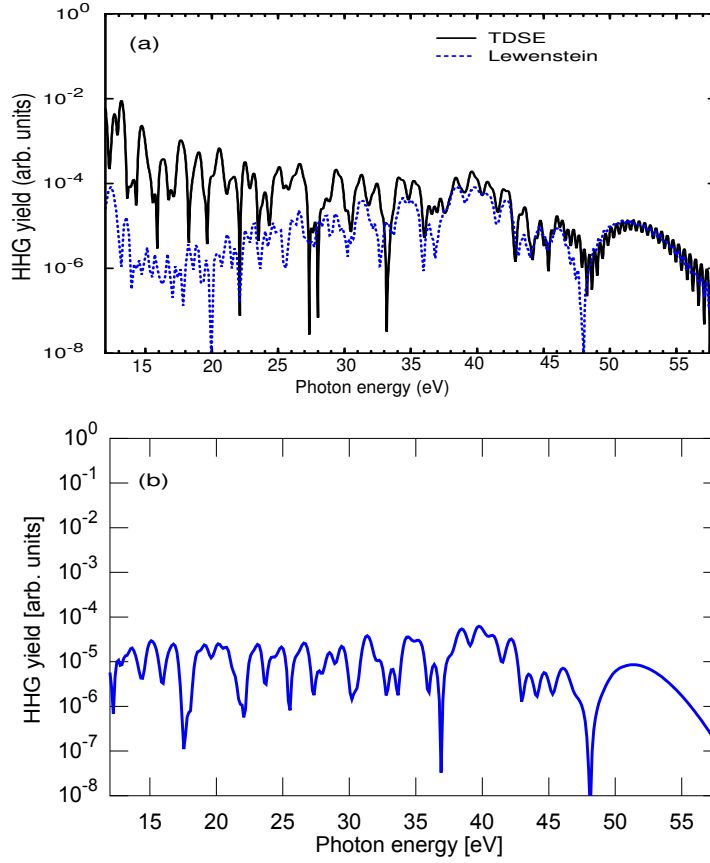


Figure 4.1.: Comparison with TDSE results. a) spectra from the TDSE and the Lewenstein model reproduced from [16]. b) result of a simulation with the code implemented here using the same driving field parameters

It is interesting to see that for low harmonics, even the two curves computed with the Lewenstein model differ. This is because different dipole matrix elements are used which follow from the different atomic potentials.

4.2. Macroscopic Response from a Gas Target

As the gas target consists of many atoms, the macroscopic harmonic radiation results from the interference of the harmonic radiation of the individual atoms. The spatial and spectral/temporal properties of the macroscopic response emerge from this interference.

To achieve a strong harmonic yield, it is important that the interference is constructive. What is important for the magnitude of the harmonic yield is the interference in direction of the optical axis. This is called phase matching. The interference in

transverse direction is also important, but mostly affects the quality of the emitted harmonic beam (transverse profile, e.g. divergence angle) and not the magnitude.

There are several effects that limit phase matching in reality. First, the driving field phase behaves differently from a plane wave. In focussed beams, there is a Gouy phase term that is amplified in the harmonic radiation and leads to a phase mismatch (geometrical phase matching). Second, the driving field intensity may vary in direction of the optical axis. As the driving field intensity affects the phase of the harmonic radiation, this also leads to a phase mismatch. Third, if the driving field and the harmonic radiation have different phase velocities, this will also create a phase mismatch.

It is desirable to optimize HHG experiments for strong harmonic yield, i.e. for good phase matching. There are many degrees of freedom that can be used to achieve good phase matching, two of these are the position of the gas target and the diameter of the gas jet. The implemented model allows us to study how these two degrees of freedom affect the harmonic yield and can help us to get a better understanding of some aspects of phase matching. For this, simulations with the experimental parameters used in [24] were made, which used a pulsed Gaussian beam with a central wavelength of 1040 nm, a beam waist of 20 μm , a peak intensity of $1.1 \cdot 10^{14} \text{ W/cm}^2$ and a temporal FWHM of 57 fs to produce high harmonics in neon. The resulting Rayleigh range of the Gaussian beam is $z_R = 1.21 \text{ mm}$.

Figure 4.2 shows how the gas jet diameter affects the harmonic yield for a gas target placed directly in the middle of the focus, for the 39th, 45th and 51st harmonic. As one can see, the power of the harmonic radiation increases with increasing gas jet diameter, as the interaction volume grows. However, when using gas targets that are larger than approximately 100 μm , the harmonic yield start to decrease again due to the destructive interference that comes from the bad phase matching conditions. So the optimal diameter of the gas jet would be around 100 μm , depending on the harmonic one wants to optimize. One can clearly see that the harmonic power oscillates with the gas jet diameter due to the phase mismatch. However, the oscillation decays slowly because of the absorption of the harmonics within the gas target. For the simulation, a gas density of $2.46 \cdot 10^{24} \text{ m}^{-3}$ was assumed, which corresponds to a pressure of 0.1 bar at 22°C.

Until now, only gas targets placed in the middle of the focus were considered. It is however also possible to move the target in parallel to the optical axis to see which region offers good phase matching conditions. Figure 4.3 shows the results of a simulations for different target positions. Each graph shows three curves. There is one curve for a gas jet with a diameter of 100 μm , one for a gas jet with a diameter of 500 μm and one curve for a very thin gas target (1 μm) that does not exhibit phase mismatch. The latter is only plotted for theoretical considerations and can most probably not be realized experimentally. The total harmonic power for the thin gas target was scaled up with a factor of $100^2 = 10^4$ to be able to see which power would be possible with a 100 μm jet under optimal phase matching. The factor of 100^2 was chosen because, for ideal phase matching, the resulting harmonic amplitude is proportional to the gas jet length under the approximations made in equation (3.44).

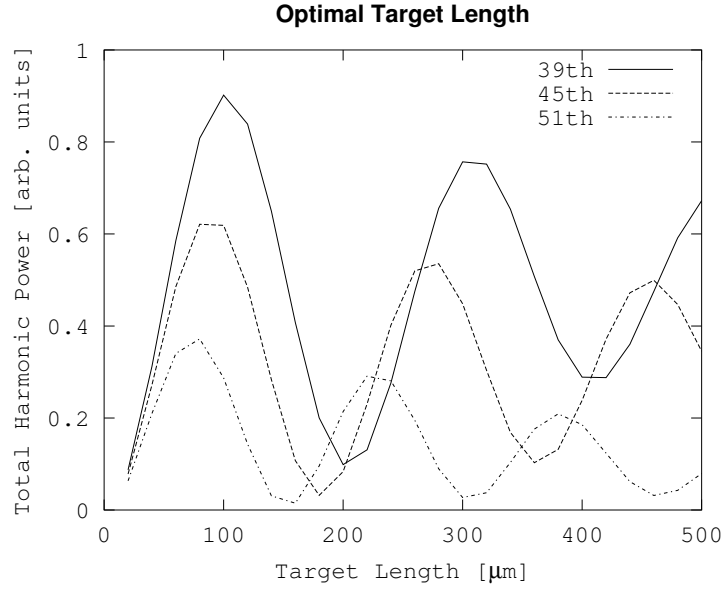


Figure 4.2.: Harmonic yield versus gas jet diameter for a gas target placed directly in the focus

One can see that for the 1 μm target, the optimal target position is directly in the focus, which is not surprising as the driving field is most intense there. Moreover, the curve is symmetric with respect to $z = 0$ because the driving field amplitude is also symmetric, and phase matching effects do not play a role here.

For the 100 μm target, the curve gets asymmetric. Although the driving field amplitude is symmetric, the Gouy phase term of the driving field phase is antisymmetric (compare to equation 3.11). Because of this, there may be different phase matching conditions before and after the focus so that the generated harmonic power can be asymmetric with respect to $z = 0$. The optimal target position is slightly behind the focus. To explain this, one has to consider the different contributions to the harmonic phase. The different phase velocities of driving field and harmonic radiation are neglected in this simulation, but the Gouy phase of the driving field and therefore of the harmonic radiation decreases with increasing z . Moreover, the driving field intensity increases with z before the focus, and after the focus it drops. The harmonic phase has a negative dependence on the driving field intensity, which means that the contribution to the harmonic phase which comes from the driving field intensity increases. Therefore, the phase mismatch due to the Gouy phase and the phase mismatch due to the intensity cancel partially behind the focus and sum up before the focus, which explains why the highest harmonic power can be produced behind the focus.

The 500 μm target shows a more complicated behavior. It can be seen that even though the 100 μm gas jet yields better results than the 500 μm one when both are

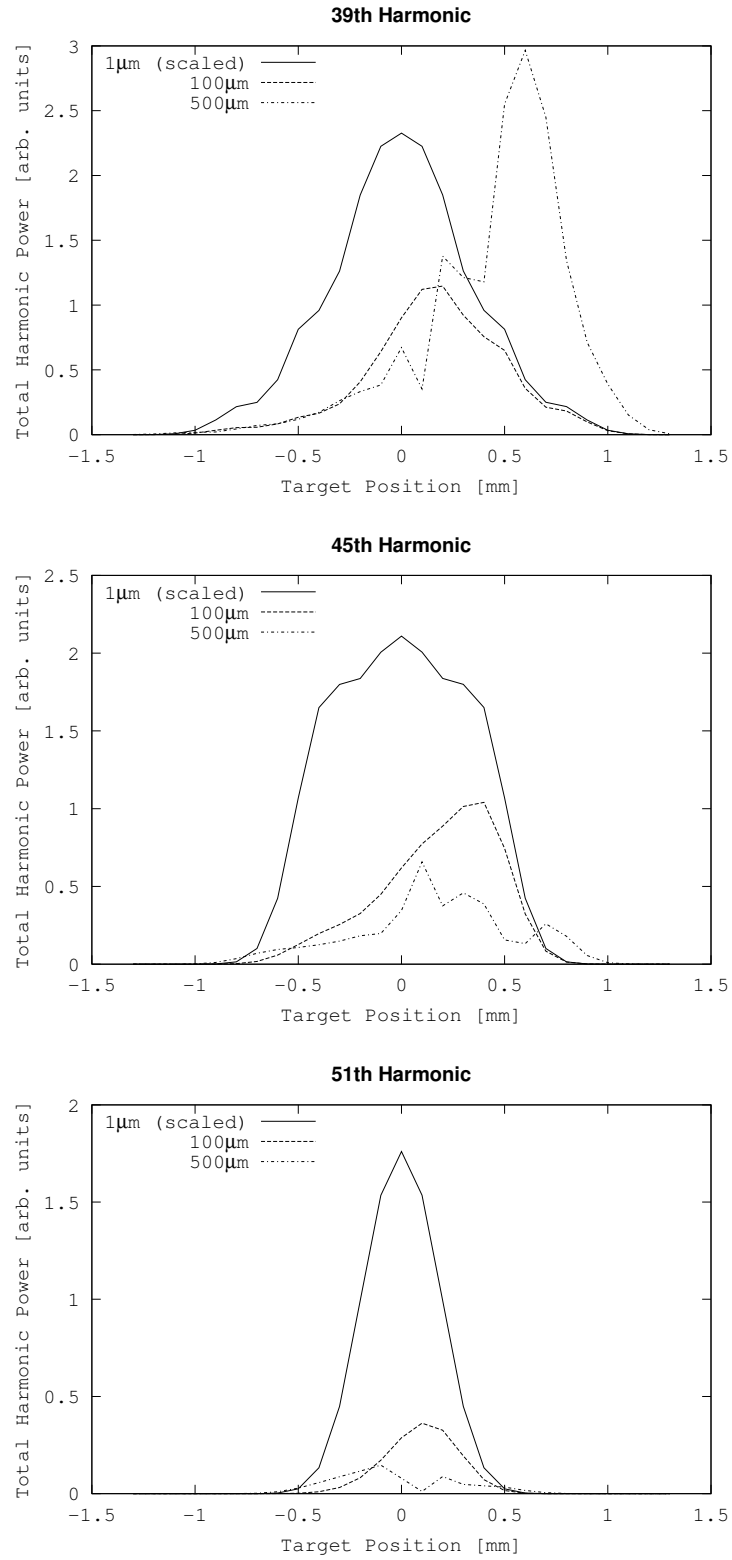


Figure 4.3.: Harmonic yield and effect of phase matching for different target positions. The curve for the 1 μm gas jet was scaled with a factor of 10^4 .

placed directly in the focus, it is possible to achieve more power with the 500 μm target if the target position is varied. For example, at the 39th harmonic, nearly 3 times as much power can be achieved. In real experiments, this may not be possible, however, because additional phase mismatch is introduced by the different phase velocity of driving and harmonic field, which is neglected here.

To quantify how much impact phase matching has for the 100 μm target, we can compare the power with the up-scaled power we get from the thin target with ideal phase matching. Typically, one gets powers within the same order of magnitude when the target is placed at a suitable position, but loses at least a factor of 2 due to phase mismatch.

4.3. Output Coupling from Enhancement Cavities

4.3.1. Motivation

For several applications, not only a high XUV power is interesting, but also high repetition rates, either to achieve sufficient tooth spacing in XUV frequency combs or because the application has an intrinsic limit on the data that can be acquired in one pass. For example, a MHz repetition rate XUV frequency comb at 60 nm with a sufficient intensity might enable spectroscopy of the $1S - 2S$ two-photon transition in He^+ [21]. If it is also possible to achieve isolated attosecond pulses, this would allow much higher data acquisition rates in pump-probe experiments – e.g. in photoelectron emission spectroscopy/microscopy, where the single-pass efficiency is limited by space-charge effects [6]. Another example where a high repetition rate XUV source is desirable is coincidence spectroscopy, which requires a low event probability in one single pass which also leads to large data acquisition times [26].

The most successful approach for high harmonic generation at MHz repetition rates with sufficient power is to produce the harmonics inside of enhancement cavities. Enhancement cavities are passive resonators that are seeded by a pulsed input laser with a repetition rate that fits the round-trip time of the resonator. Inside the cavity, it is possible to achieve pulse energies much higher than that of the seeding laser because the circulating pulse is amplified at each round trip by a seed pulse. As the conversion efficiency for HHG is very low, it is in principle possible to place a gas target inside the cavity and recycle the driving field pulse after it hits the gas target. The main working principle of an enhancement cavity is that there must be a partially reflecting mirror, called the input coupler, at which the seeding laser can enter the cavity with very low loss. For this, the cavity geometry is chosen in a way so that the circulating beam leaving the cavity through the input coupler interferes destructively with the part of the seeding pulse that is reflected by the input coupler (see figure 4.4).

One problem that must be solved when producing high harmonics within an enhancement cavity is how to get the harmonic radiation, which is emitted collinearly with the driving laser beam, out of the cavity. So far, there have been several approaches. The first one was to use an intra-cavity plate that is placed at Brewster's

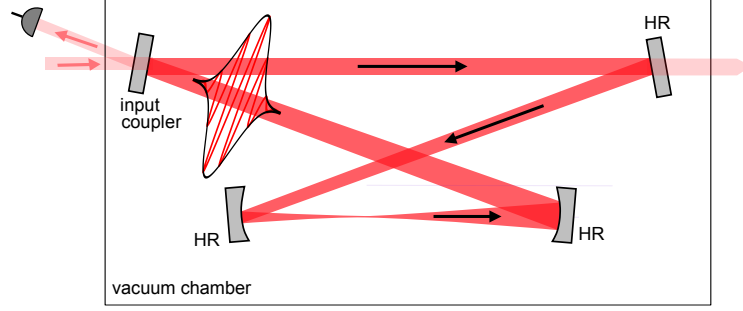


Figure 4.4.: Working principle of an enhancement cavity

angle for the driving field wavelength, so that the circulating driving pulse is transmitted and the harmonic radiation is partially reflected ([15] and [11]). Another approach is to use a reflective grating that reflects the driving beam at another angle than the harmonic radiation. This, however, results in the different harmonics to be angularly dispersed.

Another possibility is to drill a tiny hole in the cavity mirror that comes after the gas target, so that the harmonic radiation can leave the cavity through this hole. This will lead to losses for the circulating driving laser. However, the divergence angle of the harmonics can be significantly smaller than that of the driving beam, so that the hole diameter can be chosen small enough to allow for an acceptable enhancement.

Building on this idea, one can also use a higher order mode for the driving field in the cavity. This mode can be chosen in a way that it avoids an opening in an output coupling mirror, but the harmonics are produced in a way that they pass the opening. This is described in chapter 4.3.2.

4.3.2. HHG in a Quasi-Imaging Resonator

Using the implemented model, it is possible to conduct simulations of HHG with higher order transverse modes optimized for output coupling in an enhancement cavity. In order to excite such a mode inside the cavity, it is necessary to adjust the cavity in a way that multiple Gauss-Hermite modes are resonant at the same time. In this case, the coefficients of these modes adapt automatically for minimal round-trip losses. This is called quasi-imaging [28].

Using the Gauss-Hermite modes GH_{00} and GH_{04} and a slit in the output coupling mirror, it is possible to excite a mode that avoids the slit in the mirror but has a strong on-axis intensity maximum near the focus. This mode is given by

$$\sqrt{3/11} \cdot GH_{00} - \sqrt{8/11} \cdot GH_{04}$$

and will be called simple slit mode (SSM) in the following. The intensity of this mode in the y - z -plane is shown in the upper part of figure 4.6. The on-axis maximum can be seen around the z position ± 0.8 mm. Below the figure, also an on-axis line-cut

is shown. Directly at the focus ($z = 0$), the mode exhibits an on-axis minimum but two off-axis maxima.

Until now, HHG with higher-order transverse modes has not been extensively studied, so the question arises whether good phase matching can be achieved at all with such a mode. The lower part of figure 4.6 shows the phase of the simple slit mode, also in comparison to a Gaussian beam with the same beam parameters¹. It can be seen that the phase has a higher slope than this is the case for the Gaussian beam.

To see whether phase matching is a limiting factor for HHG with the SSM, detailed simulations with the model implemented here and an experiment were conducted² that allows to verify the results. In both the simulation and the experiment, harmonics were produced in a 100 μm xenon gas jet with a backing pressure of 3 bar using a SSM with a beam waist of 18.8 μm and a central wavelength of 1040 nm. The intra-cavity pulse duration was 100 fs.

Interesting questions that can be answered by simulations are the detailed shapes of the harmonic beams for given harmonics, the achievable output coupling efficiency and how the phase matching conditions are. Figure 4.7 shows the harmonic beams for different harmonic numbers and target positions – one time, the target was placed directly in the focus ($z = 0$), where the driving field has two lobes, and one time the target was placed at $z = \pm 0.825$ mm, which corresponds to the on-axis intensity maxima. For a target positioned in the focus, one can clearly see a interference pattern similar to that of a double slit. This is not surprising, since the two lobes of the SSM at $z = 0$ emit harmonic radiation in phase, just as like a double slit aperture would have been placed before a homogenous source of harmonic radiation. For targets positioned at $z = \pm 0.825$ mm, the beam profiles resemble more a Gaussian beam. There are still interference patterns due to the side lobes of the driving field that can also be seen in the upper part of figure 4.6, but most of the power is generated in the on-axis lobes which leads to the emission of nicer harmonic beams, especially for the near-cutoff harmonics H17 and H19, where interference between the short and long trajectory also do not play an important role.

From the beam profiles, the output coupling efficiency for a given slit width can be determined. Figure 4.8 shows the output coupling efficiencies for different harmonics versus assumed slit width, together with a curve that shows the round-trip losses of the circulating driving field, under the assumption of a perfect slit, i.e. all radiation outside the slit width gets reflected and radiation inside the slit width gets transmitted. The target was placed at the position $z = 0.825$ mm. For the 17th harmonic, it is possible to achieve output coupling efficiencies up to 70% if a theoretical enhancement of 200 (which corresponds to round-trip losses of 0.05%) is desired. Lower harmonics have slightly worse output coupling efficiencies due to the fringes that surround central beam (see figure 4.7), which most probably result from

¹The plot uses another sign convention than (3.11), so the phase has the opposite sign.

²The experiment was conducted at the Laboratory for Attosecond Physics by Ioachim Pupeza, Simon Holzberger, Johannes Weitenberg and Maximilian Högner

the long trajectories.

For output coupling, all three considered target positions are interesting. The target position directly in the focus can be expected to have the highest harmonic intensity (compare second plot of figure 4.6), while the target positions at the on-axis maxima of the driving field have beam profiles which are likely to allow for better focusability. Which target position yields the highest harmonic intensity also strongly depends on phase matching. To determine suitable target positions and to investigate the effect of phase matching, the total harmonic intensity for different harmonics is plotted versus the target position (figure 4.9). For this, two different jet diameters were assumed – a jet with a diameter of 100 μm and a diameter of 200 μm . In order to estimate how strong the phase mismatch reduces the harmonic yield, also the power of a very thin gas target (1 μm), which small enough that no phase matching can occur, is plotted along the other curves. This curve is scaled by a factor $50^2 = 2500$, which corresponds to a gas jet of 50 μm with ideal phase matching conditions³.

It can be seen that the curve for the 1 μm target is symmetric with respect to $z = 0$, but the curves for the thicker targets are asymmetric. This is because the harmonic power that is generated in an infinitesimally thin z slice depends only on the amplitude and not on the phase of the driving field. If multiple z slices are considered, the individual contributions sum up coherently so that phase matching plays a role. The SSM, like a standard Gaussian beam, has a symmetric amplitude but anti-symmetric phase with respect to $z = 0$.

Concerning the power, it can be seen that a thicker gas jet does not necessarily lead to more generated XUV power. For some target positions, with a 200 μm target less power is generated than with a 100 μm due to phase mismatch. The optimal gas jet diameter is near 100 μm which corresponds to what was found experimentally for the ideal jet diameter when doing HHG with a Gaussian beam.

If the 1 μm curve is scaled up to a 100 μm gas target instead to a 50 μm target, a factor of 4 will be introduced. Even then, we can see that in the most cases the 100 μm curve achieves the same magnitudes of power than the scaled curve, which indicates that phase matching is not a limiting factor for HHG with this mode.

In the experiment (see figure 4.5), the harmonic yield was optimized by trying different end-fire nozzles for producing the gas jet. It turned out that a 100 μm nozzle gave the best results, which fits with the observations from the simulation that phase mismatch begins to occur for gas jet diameters larger than 100 μm . In order to record the beam profiles of the individual harmonics, the output coupled radiation was split up spectrally with a reflective diffraction grating. An example of the recorded beam profiles can be seen in figure 4.10.

Unfortunately, it is not possible to observe the full beam profiles as shown in figure 4.7, because only a small part is coupled out through the slit in the mirror so that the beam profiles are cut in y direction. Nonetheless, one can compare the behavior in x direction with the simulation results. For this, only a central line cut is considered.

³compare to equation (3.44)

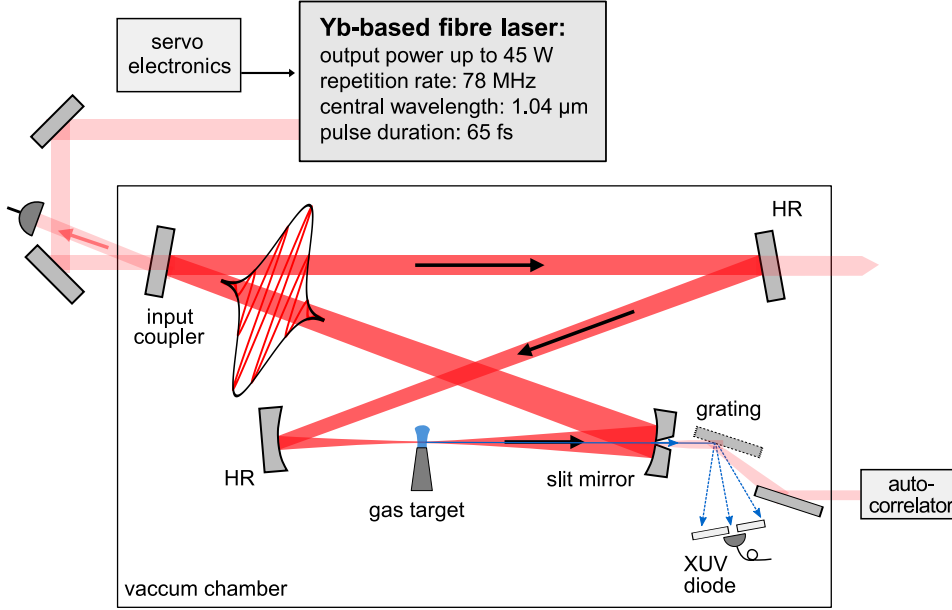


Figure 4.5.: Experimental setup for HHG with the simple slit mode

To verify the simulation data, line cuts through the simulated beam profiles are compared to line cuts through the experimentally obtained beam profiles (see figure 4.11). For this, the x position and scaling of the simulated line cuts are chosen to overlap nicely with the measured ones. After that, the relative scaling factors can be compared to the theoretically obtained ones that follow from the conversion efficiency of the screen and the grating efficiency. The agreement is within 10%, so the implemented model seems to describe the experiment quite well for this purpose.

By fitting Gaussians to the experimental and simulated curves, it is possible to compare the full width at half maximum (FWHM). This makes most sense for the near-cutoff harmonics H17 and H19, as the lower harmonics come with side lobes, which can most probably be explained by the long trajectory and make it difficult to fit a Gaussian to the beam profile. For the 17th and 19th harmonic, the FWHM obtained this way are plotted versus target position in figure 4.12. As can be seen, there is a very good agreement between measurement and simulation.

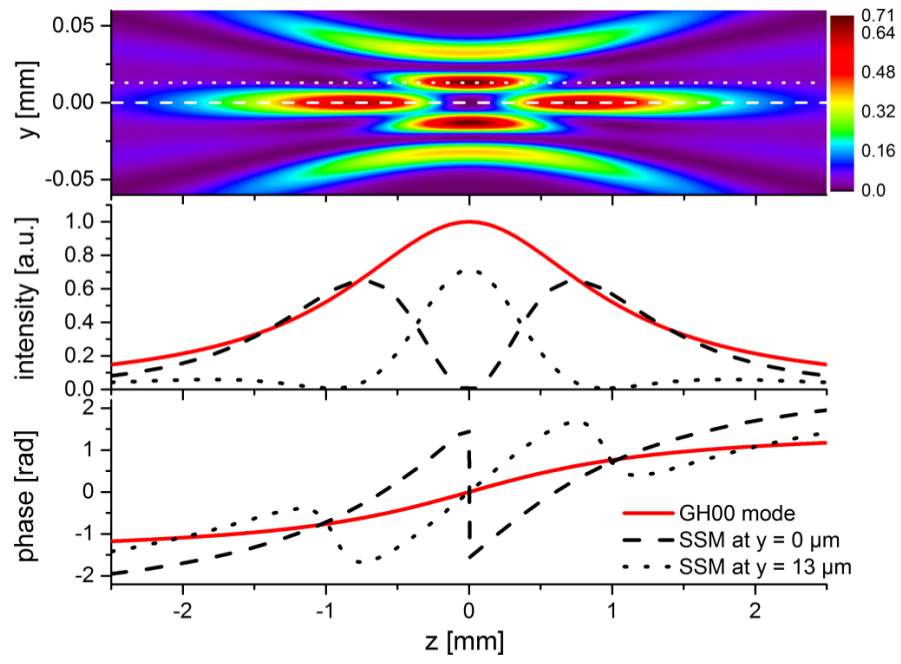


Figure 4.6.: Intensity and phase profile of the simple slit mode

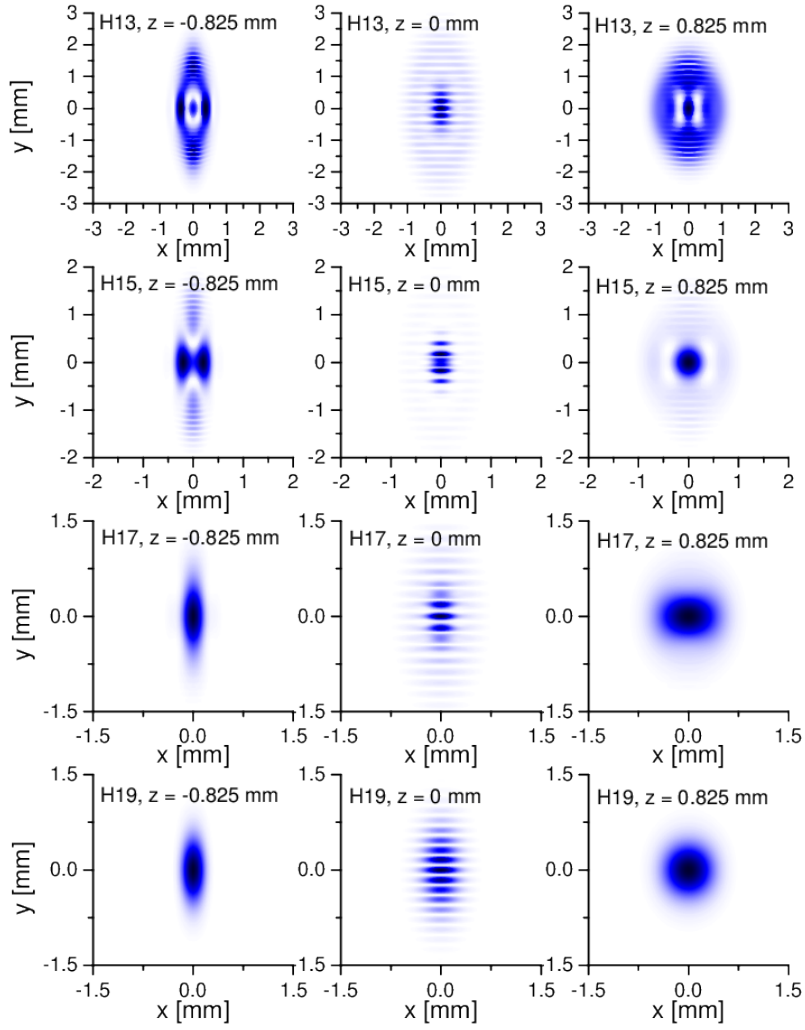


Figure 4.7.: Simulated harmonic beam profiles for three different target positions

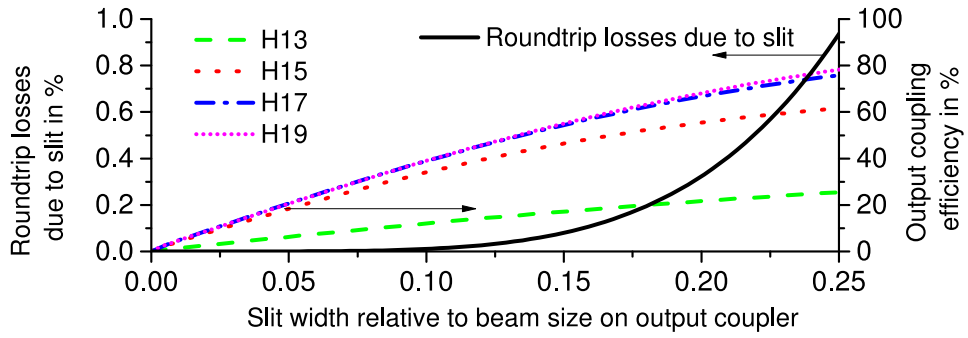


Figure 4.8.: Overview of achievable output coupling efficiencies for different slit widths versus round-trip losses of driving pulse

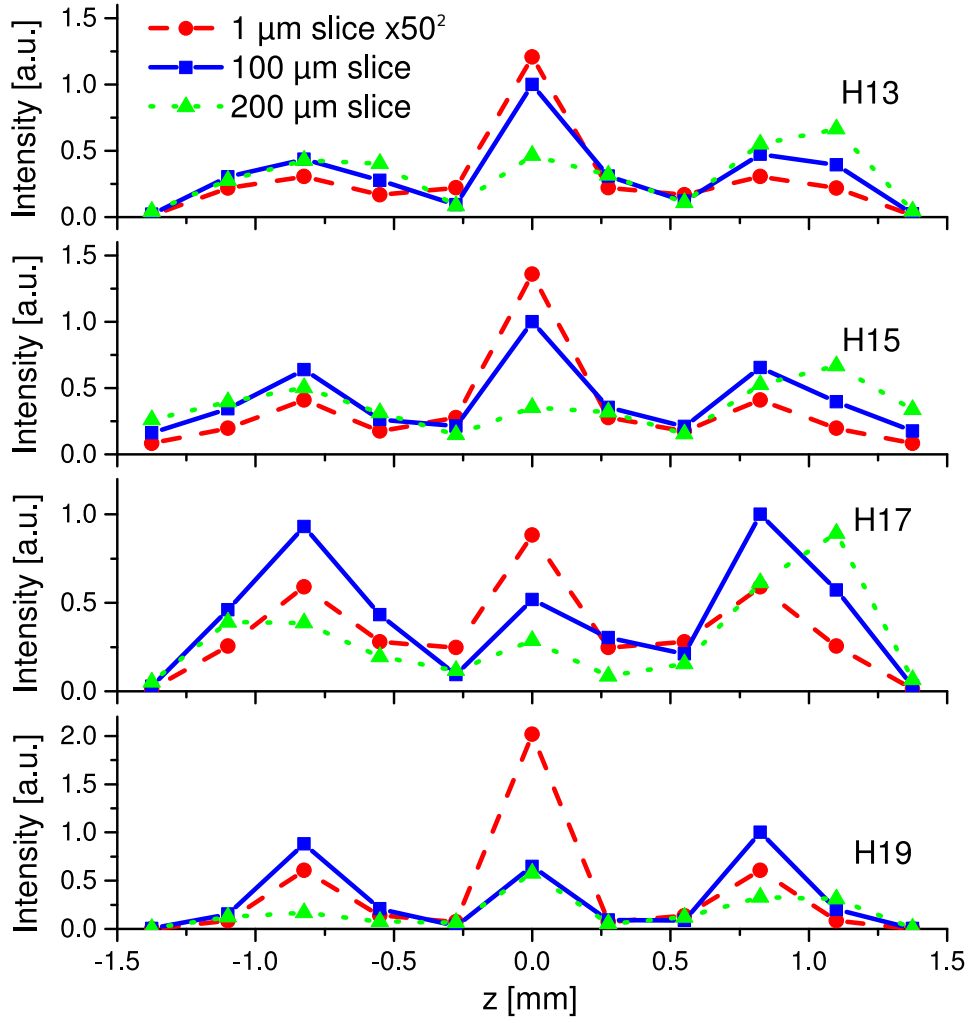


Figure 4.9.: Harmonic power generated with the SSM at different target positions with different gas jet diameters



Figure 4.10.: Picture of fluorescent screen with harmonic orders 7–19

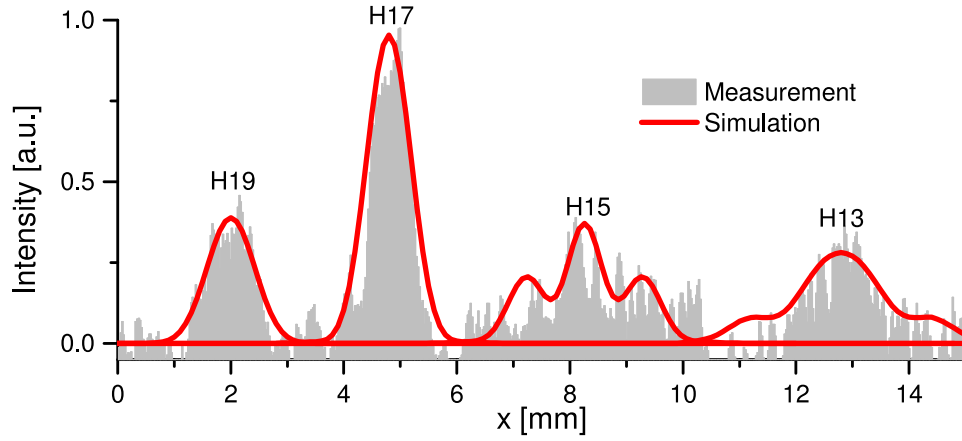


Figure 4.11.: Comparison of linecuts obtained from measurement and simulation

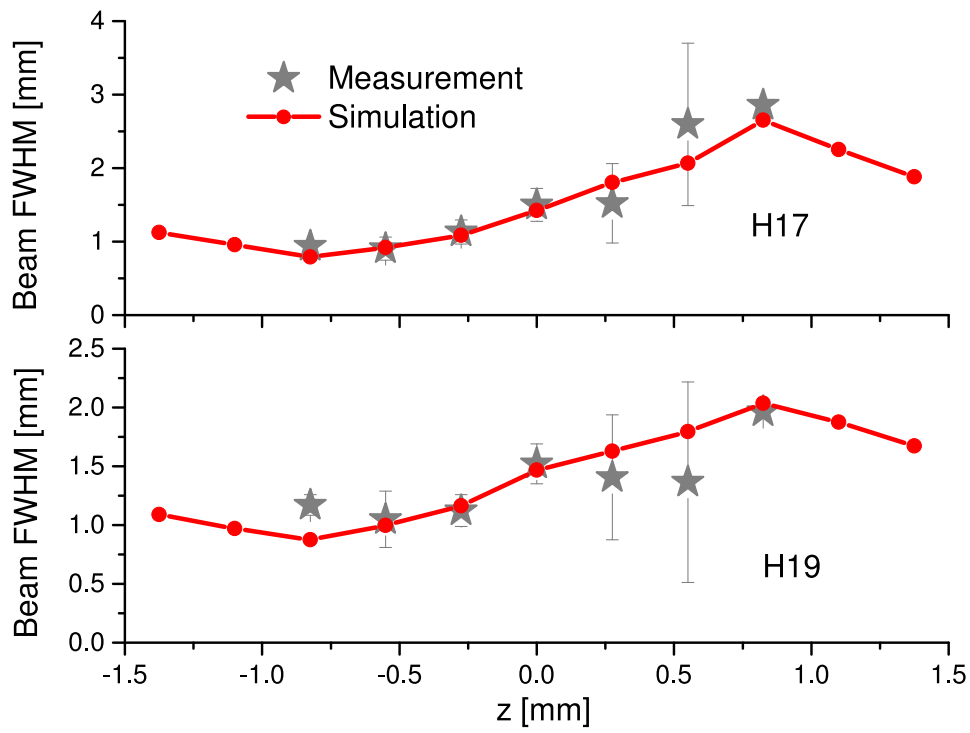


Figure 4.12.: Comparison of full widths at half maximum determined from measured and simulated beam profiles

5. Outlook

5.1. Future Experimental Focus

The proof-of-principle experiment described in chapter 4.3.2 demonstrates that it is possible to use spatially tailored driving fields in combination with slit mirrors as an efficient output coupling mechanism for HHG in enhancement cavities. In particular, a considerable harmonic power of $11\ \mu\text{W}$ was coupled out at $60\ \text{nm}$. Exploiting all spatial degrees of freedom of the driving field and optimizing other experimental parameters like mode matching, it appears quite possible to increase the power at and around this wavelength by an order of magnitude, which would pave the way for precision spectroscopy of the $1S - 2S$ two-photon transition in He^+ . Using the computational model developed in the scope of this thesis, different transverse modes can be investigated with respect to output coupling efficiency and harmonic beam quality, and experiments with these optimized transverse modes can be conducted.

Until now, the computational model described in this thesis was only applied to describe spectral and spatial features of the harmonic radiation. However, the time domain is also very interesting to examine, given the fact that isolated attosecond pulses at a high repetition rate would allow for several interesting applications in time-resolved spectroscopy and microscopy. Usually, an attosecond burst per driving field half cycle is emitted, as long as the oscillation amplitude is large enough. Therefore few-cycle driving pulses are needed to achieve isolated attosecond pulses. In enhancement cavities, however, which would be the means of choice for achieving high repetition rates, the cavity mirrors are usually not broad-band enough to allow for few-cycle circulating pulses. So to obtain isolated attosecond pulses in enhancement cavities, it is necessary to use gating mechanisms that restrict the time window in which harmonics are produced even though the driving field pulse is relatively long.

One promising gating mechanism is polarization gating. The conversion efficiency of HHG drops considerably for increasing ellipticity of the driving field, which allows to produce pulses with time-dependent ellipticity that only produce harmonics within a narrow time window. This can be realized e. g. by sending a linearly polarized input beam through two birefringent plates. This gating mechanism was already demonstrated in several experiments (e. g. [25]), and should also be suitable for enhancement cavities, as the polarization features of a circulating pulse also reproduce after each round trip.

Moreover, it might be possible to tailor driving fields that lead to a time-dependent emission direction of the harmonic radiation (lighthouse effect), so that isolated

attosecond pulses can be obtained by spatial filtering in the far field.

5.2. Extensions of the Computational Model

Single-Atom Dipole Response

For lower harmonics, the Lewenstein model, which is implemented here, does not yield quantitatively correct results. One possibility to improve this would be to include a module that solves the TDSE numerically, e. g. using a split-step Fourier method, as an alternative to the fast Lewenstein model. This, however, is computationally very expensive and might only be suitable for small space grids on which the dipole elements should be calculated. There also exist several more sophisticated models than the Lewenstein model that achieve impressive agreements with TDSE solutions ([22], [10]), which might be suitable for implementing but might be less general than the Lewenstein model. Most easy, however, would be to scale the dipole spectra obtained from the Lewenstein model to account better for the atomic potential in the recombination step, as suggested by Le et al. in [16].

Elliptical Polarization

To investigate polarization gating, the implementation of the computational model must support generally polarized driving fields. The current implementation already allows to compute dipole spectra for general elliptically polarized driving fields. The described model is in principle also able to simulate the build-up of polarized harmonic beams as long as the electric field component in direction of the optical axis vanishes, but this is not implemented yet. This would be straightforward to do and is planned for the future.

Performance Optimizations by Exploiting Symmetry

Often, the driving field is radially symmetric or symmetric with respect to a plane. This symmetry also manifests in the dipole responses. A considerable improvement in computation speed could be achieved if these symmetries would be exploited when present, without restricting the implementation to symmetric fields.

Ionization of the Gas Target

To examine the harmonic radiation in the time domain, it is important that the harmonic spectrum is modeled very accurately. One important factor which the presented computational model neglects currently is the ionization of the target atoms, which plays an important role except for very short driving pulses or low intensities. Properly including ionization into the computational model takes two steps: First, the ground state depletion must be handled in the single atom dipole response. This is already covered both in [17] and [3] for the case that the effect of depletion is still negligible over the time scale of a few optical periods.

Second, the effect of ionization on the driving field must be taken into account. In the general case, it is not possible anymore to describe the field as a superposition of Gauss-Hermite modes, as the refractive index not spatially homogenous anymore and even gets time-dependent. In our group, some work on modeling the propagation of the driving pulse through a medium that gets ionized was already done [14], which is summarized shortly in the following to give an outlook for a possible further extension of the model implemented here.

To understand which influence the ionization has on the passing driving pulse, we consider an infinitesimally small cubic volume of the gas target. The driving pulse will start ionizing this volume as soon as the pulse amplitude arrives at a high enough level. Using e. g. the ADK model [2], it is possible to quantitatively obtain the time-dependent ionization fraction within the volume which can be assumed to be spatially constant as we assumed an infinitesimally small volume. An example using realistic parameters, apart from the volume size which is chosen in a way so that an effect is clearly visible, is shown in figure 5.1. The recombination process is rather slow – the exact recombination rate depends on the plasma temperature, which in turn depends on the interaction time – so the ionization does not drop significantly immediately after the pulse. From the ionization fraction, it is possible to calculate the susceptibility of the plasma using formula (3.34). Figure 5.1 also shows the refractive index corresponding to this susceptibility, neglecting the contributions from the neutral and ionized atoms, as the contribution from the plasma is much more important than the other contributions for high ionization fractions. By passing through a volume with a time-dependent refractive index, the driving pulse is altered non-linearly.

In order to get some insight into this process, we now regard only the central frequency component of the driving pulse. If a plane wave with frequency ω passes through a volume of length Δz with refractive index n , it acquires a phase $\Delta\phi = n\omega/c \cdot \Delta z$. For a time-dependent refractive index, this acquired phase is also time-dependent, and results in a field $A_0 \exp(i[\omega t + \Delta\phi(t)])$ right behind the volume. The increasing time-dependent phase adds to the term ωt (compare figure 5.1), which results in a higher effective frequency, i.e. the central frequency component is blue-shifted. The same considerations are valid for the other frequency components of which the driving pulse is constituted, therefore the pulse is blue-shifted in the spectral domain. The explanation for this is that the dropping refractive index results in an increasing phase velocity inside the considered volume, which allows the end of the pulse to "catch up", so that the oscillation gets faster which corresponds to a blue shift.

In figure 5.2, both the original driving pulse as well as the altered pulse after passing through the volume, as calculated with the described model, are plotted in the time and in the frequency domain. As can be seen, the spectrum is shifted to higher frequencies, and spectral broadening occurs which causes the spectral peak intensity to decrease.

In addition to this blue shift, also spatial effects must be considered. When the driving beam hits the gas target, ionization occurs where the driving field intensity

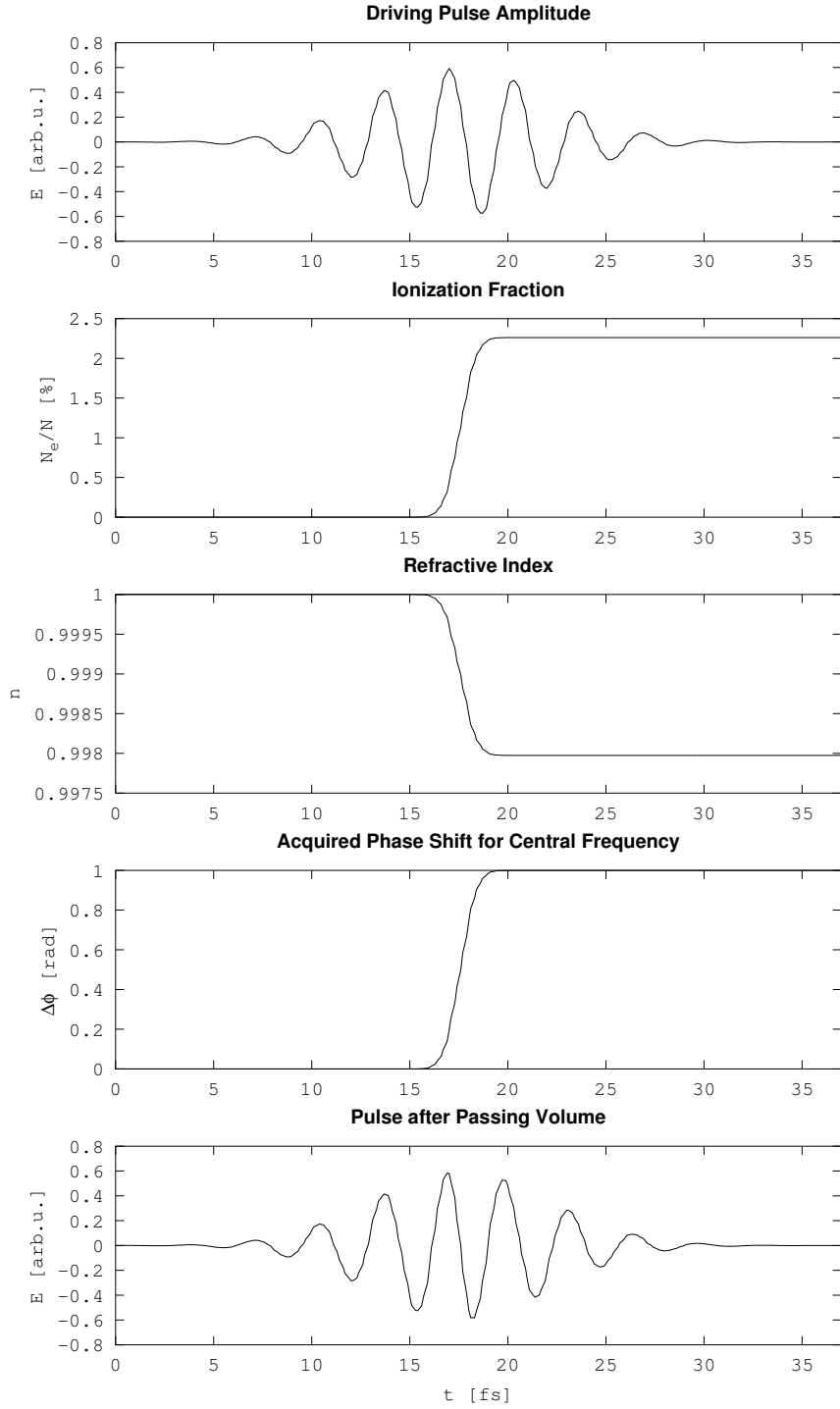


Figure 5.1.: Influence of ionization on the driving pulse for an infinitesimal cubic volume. Data from simulations conducted by Simon Holzberger.

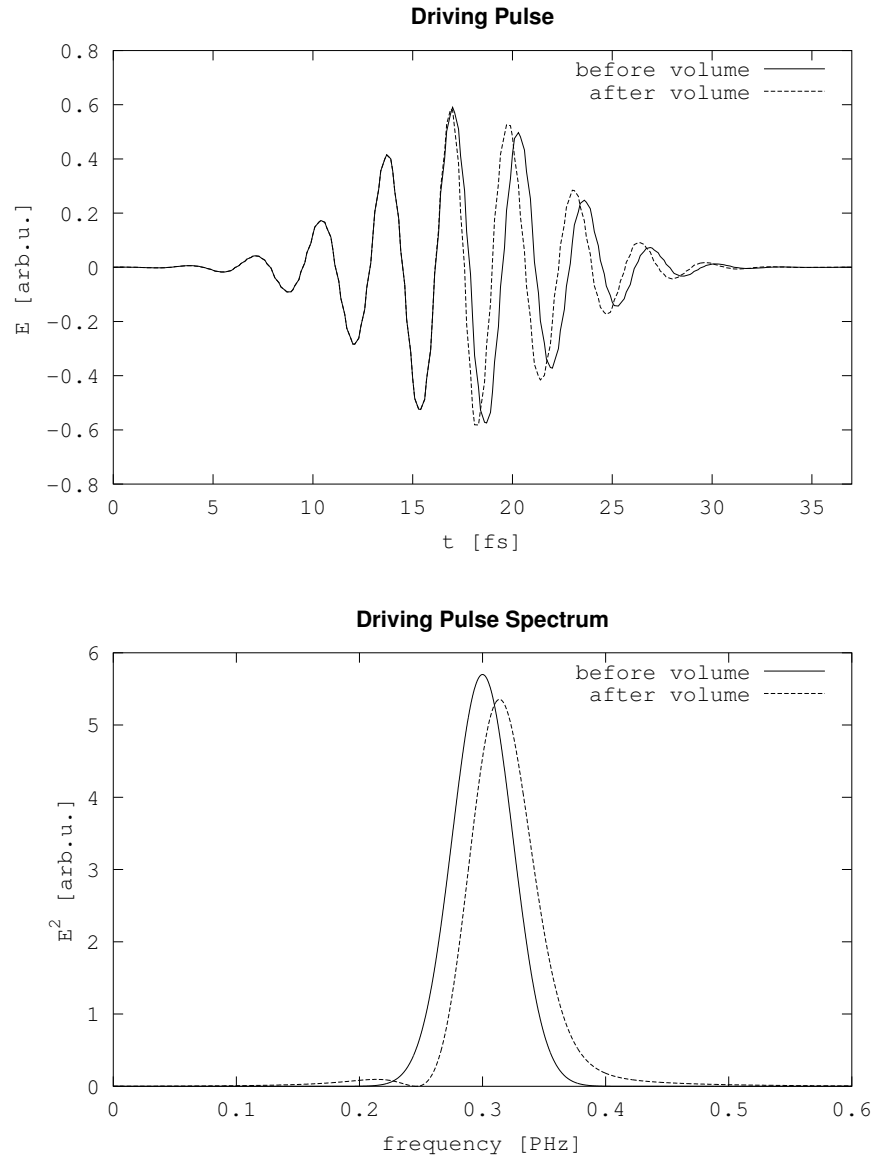


Figure 5.2.: Blueshift of the driving pulse due to ionization

is the highest, so typically near the optical axis. This means that the phase velocity near the optical axis is larger, so the phase front will be bent in a way that the beam is defocussed. This effect is called self-defocussing.

Moreover, if a high repetition rate is used, so that complete recombination between the pulses is not possible and the velocity in the gas is not sufficient to exchange the target medium fast enough, cumulative effects occur, i.e. a steady-state plasma is formed. This regime generally is not very suitable for HHG, especially in the context of enhancement cavities, as less neutral atoms are available for producing harmonics and the steady-state plasma leads to dispersion which limits the possible enhancement in cavities if not compensated.

To include these effects into a computational model, a more flexible approach for the driving field must be chosen. Currently a closed solution to the paraxial wave equation for constant refractive index is used for the driving field (compare chapter 3.3). It is not possible anymore to write down such a closed solution for the general case of a temporally and spatially dependent refractive index. Therefore the paraxial wave equation must be solved completely numerically. One suitable approach might be a split-step Fourier method where space is divided in z slices perpendicular to the optical axis and the effect of time-dependent refractive index is treated as described before while slice-to-slice propagation of the field is done in reciprocal space with a Fourier optics approach. For enhancement cavities, modeling the driving field is even more involved, since the incoming driving field is a circulating pulse, which was already modified by the gas target in previous passes.

Bibliography

- [1] TDM-GCC compiler suite. <http://tdm-gcc.tdragon.net/>.
- [2] M. V. Ammosov, N. B. Delone, and V. P. Krainov. Tunnel ionization of complex atoms and of atomic ions in an alternating electromagnetic field. *Soviet Physics - JETP*, 64(6):1191–1194, 1986.
- [3] Philippe Antoine, Anne L’Huillier, Maciej Lewenstein, Pascal Salières, and Bertrand Carré. Theory of high-order harmonic generation by an elliptically polarized laser field. *Physical Review A*, 53(3):1725–1745, March 1996.
- [4] S. Bhardwaj, Massachusetts Institute of Technology. Department of Electrical Engineering, and Computer Science. *Limits of Long Wavelength High Harmonic Generation*. Massachusetts Institute of Technology, Department of Electrical Engineering and Computer Science, 2010.
- [5] Thomas Brabec and Ferenc Krausz. Intense few-cycle laser fields: Frontiers of nonlinear optics. *Reviews of Modern Physics*, 72(2):545–591, April 2000.
- [6] S. H. Chew, F. Süssmann, C. Späth, A. Wirth, J. Schmidt, S. Zharebtsov, A. Guggenmos, A. Oelsner, N. Weber, J. Kapaldo, A. Gliserin, M. I. Stockman, M. F. Kling, and U. Kleineberg. Time-of-flight-photoelectron emission microscopy on plasmonic structures using attosecond extreme ultraviolet pulses. *Applied Physics Letters*, 100(5):051904, 2012.
- [7] P. B. Corkum. Plasma perspective on strong field multiphoton ionization. *Physical Review Letters*, 71(13):1994–1997, September 1993.
- [8] A. Dalgarno and A. E. Kingston. The refractive indices and verdet constants of the inert gases. *Proceedings of the Royal Society of London. Series A, Mathematical and Physical Sciences (1934-1990)*, 259(1298):424–431, December 1960.
- [9] Richard Fitzpatrick. Classical electromagnetism: An intermediate level course. <http://farside.ph.utexas.edu/teaching/em/lectures/node100.html>, 2006.
- [10] M. V. Frolov, N. L. Manakov, A. M. Popov, O. V. Tikhonova, E. A. Volkova, A. A. Silaev, N. V. Vvedenskii, and Anthony F. Starace. Analytic theory of high-order-harmonic generation by an intense few-cycle laser pulse. *Phys. Rev. A*, 85:033416, Mar 2012.

- [11] Christoph Gohle, Thomas Udem, Maximilian Herrmann, Jens Rauschenberger, Ronald Holzwarth, Hans A. Schuessler, Ferenc Krausz, and Theodor W. Hänsch. A frequency comb in the extreme ultraviolet. *Nature*, 436(7048):234–237, July 2005.
- [12] T. J. Hammond, Arthur K. Mills, and David J. Jones. Near-threshold harmonics from a femtosecond enhancement cavity-based euv source: effects of multiple quantum pathways on spatial profile and yield. *Opt. Express*, 19(25):24871–24883, Dec 2011.
- [13] B. L. Henke, E. M. Gullikson, and J. C. Davis. X-Ray interactions: Photoabsorption, scattering, transmission, and reflection at $e = 50\text{--}30,000$ eV, $z = 1\text{--}92$. *Atomic Data and Nuclear Data Tables*, 54(2):181–342, July 1993.
- [14] Simon Holzberger. Personal communication, 2013.
- [15] R. Jason Jones, Kevin D. Moll, Michael J. Thorpe, and Jun Ye. Phase-coherent frequency combs in the vacuum ultraviolet via high-harmonic generation inside a femtosecond enhancement cavity. *Phys. Rev. Lett.*, 94:193201, May 2005.
- [16] Anh-Thu Le, Toru Morishita, and C. D. Lin. Improved Lewenstein model for high-order harmonic generation of atoms and molecules with scattering wavefunctions. <http://arxiv.org/pdf/0707.4192v1.pdf>, 2007.
- [17] M. Lewenstein, Ph Balcou, Misha Ivanov, Anne L’Huillier, and P. B. Corkum. Theory of high-harmonic generation by low-frequency laser fields. *Physical Review A*, 49(3):2117–2132, March 1994.
- [18] A. McPherson, G. Gibson, H. Jara, U. Johann, T. S. Luk, I. A. McIntyre, K. Boyer, and C. K. Rhodes. Studies of multiphoton production of vacuum-ultraviolet radiation in the rare gases. *J. Opt. Soc. Am. B*, 4(4):595–601, April 1987.
- [19] W. Nagourney. *Quantum Electronics for Atomic Physics*. Oxford Graduate Texts. OUP Oxford, 2010.
- [20] Lukas Novotny. Electromagnetic fields and waves. <http://www.photonics.ethz.ch/en/courses/electrodynamics.html>, 2013.
- [21] A. Ozawa, J. Rauschenberger, Ch. Gohle, M. Herrmann, D. R. Walker, V. Pervak, A. Fernandez, R. Graf, A. Apolonski, R. Holzwarth, F. Krausz, T. W. Hänsch, and Th. Udem. High harmonic frequency combs for high resolution spectroscopy. *Phys. Rev. Lett.*, 100:253901, Jun 2008.
- [22] J. A. Pérez-Hernández, L. Roso, and L. Plaja. Harmonic generation beyond the strong-field approximation: the physics behind the short-wave-infrared scaling laws. *Opt. Express*, 17(12):9891–9903, Jun 2009.

- [23] L. Plaja and J. A. Pérez-Hernández. A quantitative s-matrix approach to high-order harmonic generation from multiphoton to tunneling regimes. *Opt. Express*, 15(7):3629–3634, Apr 2007.
- [24] I. Pupeza, S. Holzberger, T. Eidam, H. Carstens, D. Esser, J. Weitenberg, P. Rußbüldt, J. Rauschenberger, J. Limpert, Th. Udem, A. Tünnermann, T. W. Hänsch, A. Apolonski, F. Krausz, and E. Fill. Compact high-repetition-rate source of coherent 100 ev radiation. *Nature Photonics*, 7(8):608–612, 2013.
- [25] G. Sansone, E. Benedetti, F. Calegari, C. Vozzi, L. Avaldi, R. Flammini, L. Polletto, P. Villoresi, C. Altucci, R. Velotta, S. Stagira, S. De Silvestri, and M. Nisoli. Isolated single-cycle attosecond pulses. *Science*, 314(5798):443–446, 2006.
- [26] G. Sansone, F. Kelkensberg, J. F. Perez-Torres, F. Morales, M. F. Kling, W. Siu, O. Ghafur, P. Johnsson, M. Swoboda, E. Benedetti, F. Ferrari, F. Lepine, J. L. Sanz-Vicario, S. Zherebtsov, I. Znakovskaya, A. L’Huillier, Ivanov, M. Nisoli, F. Martin, and M. J. J. Vrakking. Electron localization following attosecond molecular photoionization. *Nature*, 465(7299):763–766, June 2010.
- [27] user1071136. Using GCC(minGW) as Matlab’s MEX compiler. <http://stackoverflow.com/questions/8552580/using-gccmingw-as-matlabs-mex-compiler#answer-9453099>, 2012.
- [28] Johannes Weitenberg, Peter Rußbüldt, Tino Eidam, and Ioachim Pupeza. Transverse mode tailoring in a quasi-imaging high-finesse femtosecond enhancement cavity. *Opt. Express*, 19(10):9551–9561, May 2011.
- [29] Richard W. Ziolkowski and Justin B. Judkins. Propagation characteristics of ultrawide-bandwidth pulsed gaussian beams. *J. Opt. Soc. Am. A*, 9(11):2021+, November 1992.

A. Documentation of the Code

A.1. Overview

In the following, the most important parts of the implementation of the computational model are described in detail. There are some additional modules which are currently undocumented, which will be fixed in the near future along with some extensions and improvements of the implementation.

The code consists of a few MATLAB modules, which are also compatible with the open source alternative GNU Octave, and an efficient, multi-processor capable implementation of the Lewenstein model in standards-compliant C++. The concept of the code is to provide a flexible framework that can be adapted to many experimental situations, but should be very easy to use. Applying the code to a standard problem should not involve programming, but only configuring experimental parameters. To achieve this goal, many example files are included.

The most important modules of the code are `dipole_response.m`, `harmonic_propagation.m` and `farfield.m` (see figure A.7). The first one computes the dipole spectra on a space grid for a given driving field, the second uses the dipole spectra to calculate the electric field within a plane right after the target, and the third propagates the electric field to a far-away plane.

The driving field can be computed by `gh_driving_field.m`, which in turn makes use of `gh_mode.m` for the spatial shape.

The Lewenstein model is implemented in C++ in the file `lewenstein.hpp`, which can also be used standalone from other C++ code. The Matlab (or Octave) interface is provided by `lewenstein.cpp`.

`info.m` can be used to display some useful parameters like photon energy or cutoff position. `hermite.m` calculates physical hermite polynomials, as needed for `gh_mode.m`. `plane_wave_driving_field.m` can be used for simple tests that do not need a fancy spatial shape of the driving field.

A.2. Installation

A.2.1. MATLAB under Windows

If you use MATLAB under Windows, it should be sufficient to copy the program directory to your disk. In order for the C++ implementation of the Lewenstein model to run, you need the DLL file `vcomp90.dll`. For the case that your system does not provide this file, the program directory contains a 32-bit and a 64-bit version of this file (`vcomp90_x86-32.dll` and `vcomp90_x64-64.dll`) that you can rename to

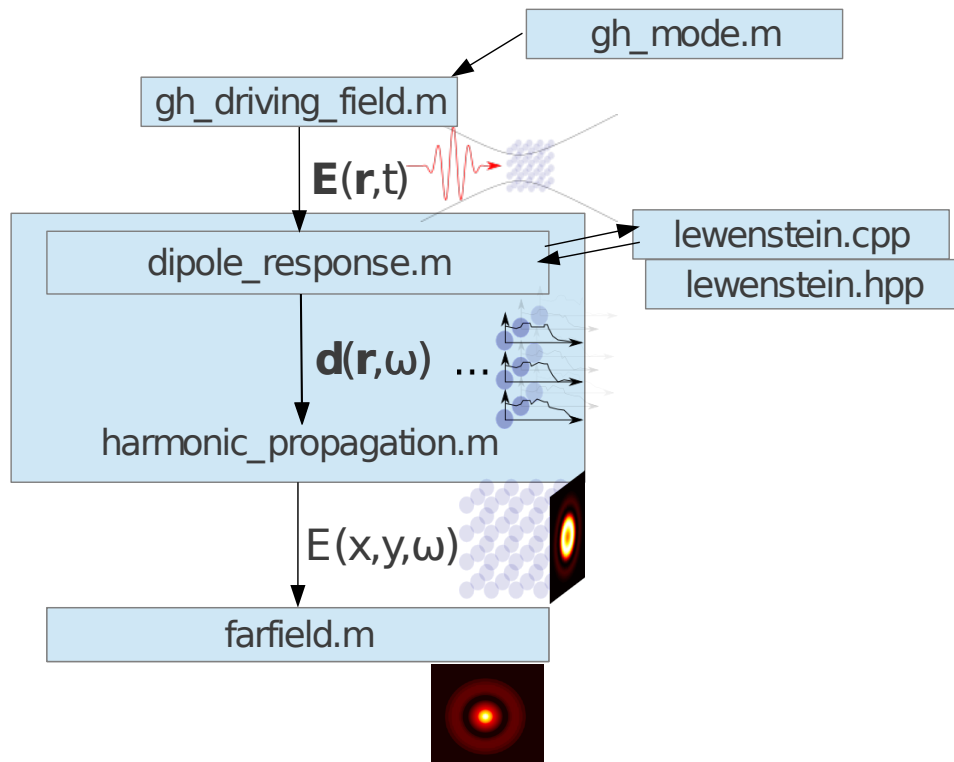


Figure A.1.: Data flow diagram

vcomp90.dll. Alternatively, you can obtain this file from the Microsoft Visual C++ Redistributable Package.

The program comes with precompiled 32-bit and 64-bit executables for the C++ implementation of the Lewenstein model, so you don't need to compile anything.

If you make changes to the C++ part of the code, however, you will need to recompile. This works from within MATLAB, but you will need Microsoft Visual Studio C++ installed – unfortunately, the free Express version of the compiler does not produce multi-processor capable executables. To compile the Lewenstein implementation, open MATLAB, change your working directory to the program directory, and run

```
> mex lewenstein.cpp COMPFLAGS="/openmp $COMPFLAGS"
```

With some tweaking, it is also possible to use the Express version of the compiler to produce multi-processor capable executables. For this, you need to obtain `vcomp.lib` from the Windows SDK and copy it to the `VC\lib\ARCH` subdirectory of your Visual Studio installation directory, where `ARCH` must be replaced by your architecture.

Also, as an alternative to Microsoft Visual Studio C++, you can use the open source compiler TDM-GCC [1, 27]. At installation, you must select **Components** > **gcc** > **openmp**. To compile a `.mex` file for 64-bit MATLAB, open MinGW Command Prompt, change your working directory to the program directory, and run

```
> set MATLAB=YOUR_MATLAB_PATH
> x86_64-w64-mingw32-c++ -m64 -shared -I"%MATLAB%/extern/
  include" -DMATLAB_MEX_FILE -fopenmp -O3 -ansi -o
  lewenstein.mexw64 -Wl,--export-all-symbols lewenstein.
  cpp -L"%MATLAB%/bin/win64" -lmex -lmx -leng -lmat
```

To compile for 32-bit MATLAB, use these commands:

```
> set MATLAB=YOUR_MATLAB_PATH
> mingw32-c++ -shared -I"%MATLAB%/extern/include" -
  DMATLAB_MEX_FILE -fopenmp -O3 -ansi -o lewenstein.
  mexw32 -Wl,--export-all-symbols lewenstein.cpp -L"%
  MATLAB%/bin/win32" -lmex -lmx -leng -lmat
```

A.2.2. GNU Octave under Linux

If you use Linux and GNU Octave, you need to compile the C++ part of the program yourself, but this is very easy. For Debian or Ubuntu, you need to make sure that you have installed the packages `octave`, `liboctave-dev`¹ and `build-essential`. The package names for other distributions should be similar. Then you must change your working directory to the main directory of the code and execute

¹Older systems might need `octave-headers` instead of `liboctave-dev`

```
$ CPPFLAGS="-fopenmp -O3 -ansi" LDFLAGS="$CPPFLAGS"
mkoctfile -lgomp --mex lewenstein.cpp
```

A.3. Reference

A.3.1. Driving Field

Description

The module `gh_driving_field.m` aids in calculating the time-dependent driving field at a given point in space as described in subsection 3.3. It can be used as a callback function for the `config.driving_field` argument of the `dipole_response.m` module.

Arguments and Return Values

The signature of the `gh_driving_field` function is

```
function [Et_cmc] = gh_driving_field(x, y, z, config)
```

The return value is the time-dependent complex electric field as a row vector (or multiple row vectors if a non-linearly polarized driving field is used), in vacuum comoving coordinates $(x', y', z', t') = (x, y, z, t - z/c)$ and scaled atomic units. The input arguments are:

- `x`, `y` and `z` specify a position in mm where the time-dependent driving field should be calculated.
- `config` is a `struct()` of the following fields:
 - `config.wavelength` is the central wavelength of the driving field, in mm. This is only used for unit conversion.
 - `config.peak_intensity` is the peak intensity of a corresponding Gaussian beam with the same power as the considered spatial mode, if both are assumed to be monochromatic. The unit is W/cm^2 .
 - `config.pulse_coefficients` are the complex Fourier coefficients of the temporal shape of the pulse, and `config.omega` is the corresponding angular frequency axis in scaled atomic units. The angular frequency axis must include both negative and positive frequencies. These two arguments can be produced easily with the `pulse.m` module.
 - Additionally, you need to supply all `config` fields required by `gh_mode.m`.

Example

We simulate the electric field of a Gaussian beam in vacuum with a central wave length of $1\text{ }\mu\text{m}$ and a beam waist of $10\text{ }\mu\text{m}$ for two positions: at the focus and one millimeter behind the focus. The temporal shape is a Gaussian pulse with a FWHM of 20 fs. For the peak intensity, we assume 7 W/cm^2 . For this, we use the following code:

```
% basic configuration for gh_driving_field
config = struct();
config.wavelength = 1.0e-3; % mm
config.peak_intensity = 7e13; % W/cm^2

% set pulse coefficients (temporal shape)
% configure time axis (t is in scaled atomic units, i.e.
    one
% driving field period equates to 2*pi
time_steps = 200; % per period
t = -10*2*pi : 2*pi/time_steps : 10*2*pi; % 20 periods

% and get spectrum using the pulse.m module
config.pulse_shape = 'gaussian';
config.pulse_duration = 20; % fs
[pulse_omega, pulse_coefficients] = pulse(t, config);

config.omega = pulse_omega;
config.pulse_coefficients = pulse_coefficients;

% set mode (spatial shape)
% - for details see documentation of gh_mode.m -
% note: by default, the optical axis is the z axis
config.mode = 'TEM00';
config.beam_waist = 0.010; % mm

% compute on-axis driving field at two different z
    positions
% and plot it (output is in co-moving coordinates)
Et_cmc_0mm = gh_driving_field(0, 0, 0, config);
Et_cmc_1mm = gh_driving_field(0, 0, 1, config);

plot(t, real(Et_cmc_0mm), t, real(Et_cmc_1mm))
legend('driving_field_at_z=0mm','driving_field_at_z=1mm')
xlabel('time_in_co-moving_coordinates[scaled_atomic_units
    ]')
ylabel('real_part_of_driving_field[s.a.u.]')
```

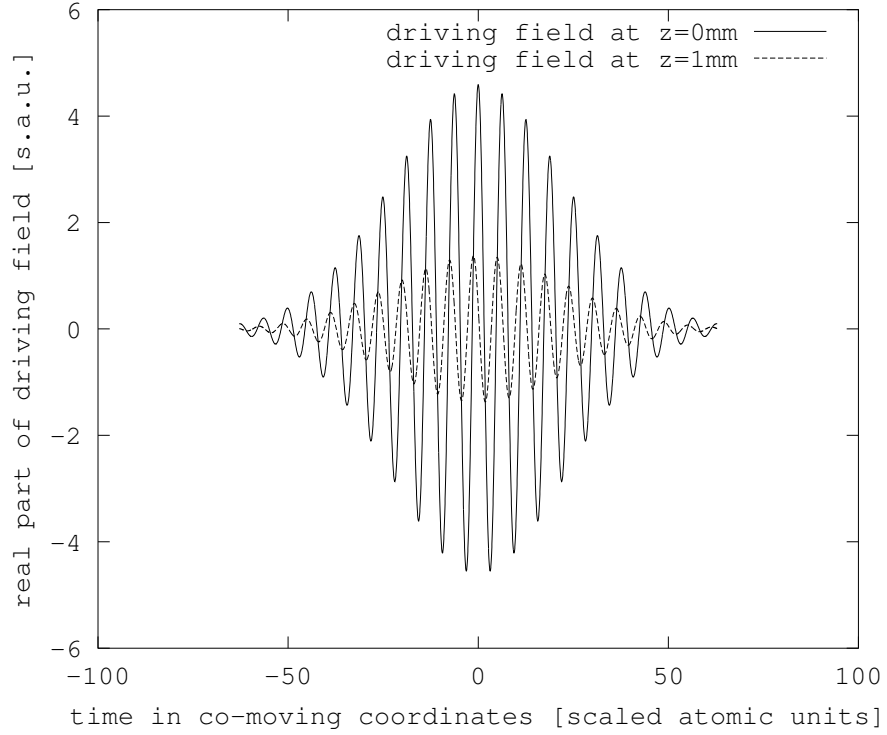


Figure A.2.: Output of the example file for simulating the driving field

The output is shown in figure A.3.1. One can see that the carrier-envelope phase differs for the two considered positions, which is due to the difference between phase and group velocity that comes from the Gouy phase.

A.3.2. Gauss-Hermite Modes

Description

The module `gh_mode.m` is used by `gh_driving_field.m` for calculating superpositions of Gauss-Hermite modes. You can select some common modes by name, but also specify the coefficients A_{nm} for the superposition directly to have more control. The following formula is implemented:

$$\sum_{nm} A_{nm} \cdot \frac{w_0}{w(z)} \cdot H_n \left(\sqrt{2} \frac{x}{w(z)} \right) \exp \left(-\frac{x^2}{w^2(z)} \right) \cdot H_m \left(\sqrt{2} \frac{y}{w(z)} \right) \exp \left(-\frac{y^2}{w^2(z)} \right) \times \\ \exp \left(i \left(kz - (1 + n + m) \arctan \frac{z}{z_R} + \frac{k(x^2 + y^2)}{2R(z)} \right) \right)$$

Arguments and Return Values

The signature of the `gh_mode` function is

```
function field = gh_mode(x,y,z,k,config)
```

The return value is the complex field amplitude of the mode superposition at the specified position, for the given `k` value, or a grid of values if a grid is used in the arguments.

- `x`, `y` and `z` specify a position in mm where the mode should be calculated.
- `k` is the wave number in mm^{-1} . Note that you can also pass a grid of values over any subset of the arguments `x`, `y`, `z`, and `k`. In this case, the return value `field` is also a grid of equal shape.
- `config` is a `struct()` of the following fields:
 - `config.beam_waist` is the beam waist w_0 in mm.
 - `config.mode_coefficients` is an array of the coefficients A_{nm} . The corresponding n and m values must be passed using the `config.mode_n` and `config.mode_m` arguments, which must be arrays of the same length.
 - `config.mode` (optional) can be used to select a predefined mode. If this is used, the arguments `config.mode_coefficients`, `config.mode_n` and `config.mode_m` are ignored and can be neglected. These modes are currently implemented:
 - * `config.mode='TEM00'` is a simple Gaussian beam.
 - * `config.mode='GH10'` is the first higher-order mode GH_{10} .
 - * `config.mode='Donut'` is the mode $\sqrt{1/2} \cdot GH_{01} + \sqrt{1/2} \cdot GH_{10}$.
 - * `config.mode='1d-quasi-imaging'` is the mode $\sqrt{3/11} \cdot GH_{00} - \sqrt{8/11} \cdot GH_{04}$.
 - * `config.mode='2d-quasi-imaging'` is the mode $\sqrt{3/11} \cdot GH_{00} - \sqrt{4/11} \cdot GH_{04} - \sqrt{4/11} \cdot GH_{40}$.
 - This argument is case-insensitive.
 - `config.rotation` (optional) is a 3×3 rotation matrix that is applied to the mode. This argument can only be used if `size(x)==size(y)==size(z)`, which can be achieved with the `ndgrid` and `meshgrid` functions.

Example

We compute the complex amplitude within three z planes for three different modes, assuming a wavelength of $\lambda = 1\mu\text{m}$. For the modes, we use a simple Gaussian beam (`config.mode='TEM00'`), a predefined higher-order mode (`config.mode='1d-quasi-imaging'`) and a user-defined mode $\sqrt{3/10}GH_{00} - i\sqrt{5/10}GH_{20} + \sqrt{2/10}GH_{03}$.

Each mode is plotted in the focal plane ($z = 0$), in a plane which is one Rayleigh range behind the focus ($z = z_R$) and at a z value far away from the focus ($z = 100z_R$). The result can be seen in figure A.3.2.

```
% set wave number (assuming lambda=1um)
k = 2*pi/1e-3; % mm^-1

% configure 3 different modes
% Gaussian beam
config1 = struct();
config1.beam_waist = 0.010; % mm
config1.mode = 'TEM00';

% a predefined mode
config2 = struct();
config2.beam_waist = 0.010; % mm
config2.mode = '1d-quasi-imaging';

% a custom mode
config3 = struct();
config3.beam_waist = 0.010; % mm
config3.mode_n = [0 2 0];
config3.mode_m = [0 0 3];
config3.mode_coefficients = [sqrt(3/10) -1i*sqrt(5/10)
    sqrt(2/10)];

% setup grid
xv = -0.02:0.001:0.02; yv = -0.02:0.001:0.02;
[x,y] = meshgrid(xv, yv);

% plot each mode at three different z positions:
% at focus, one Rayleigh range behind focus, far from
% focus
z_R = k*config1.beam_waist^2/2;

subplot_nr = 1;
for config={config1, config2, config3}; config=config{1};
    % compute field at z=0, z=z_R, z=100*z_R
    field_0 = gh_mode(x,y,0, k, config);
    field_z_R = gh_mode(x,y,z_R, k, config);
    field_far = gh_mode(100*x,100*y,100*z_R, k, config);

    % plot fields
    subplot(3,3,subplot_nr); subplot_nr = subplot_nr+1;
```

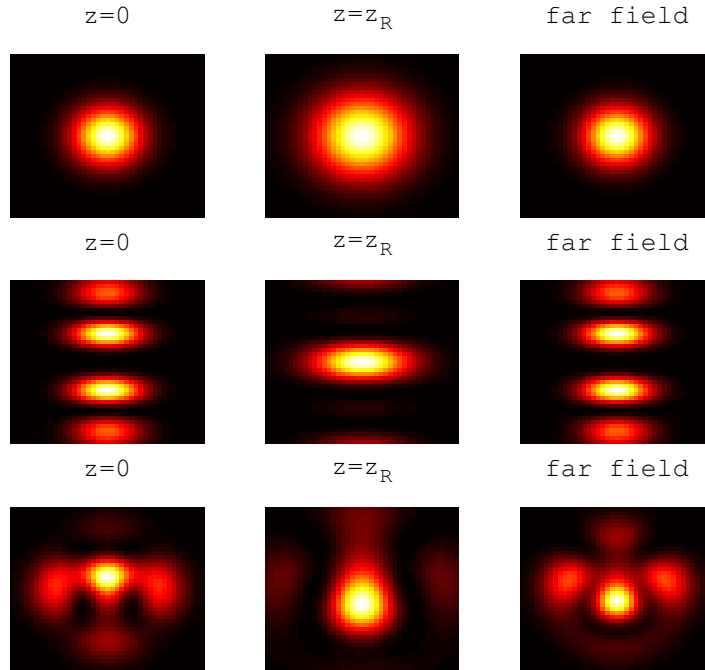


Figure A.3.: Modes calculated by `gh_mode.m`. The first row shows a Gaussian beam, the second row the predefined mode `1d-quasi-imaging`, and the third a custom superposition of Gauss-Hermite modes.

```

imagesc(xv,yv,abs(field_0).^2);
title('z=0');

subplot(3,3,subplot_nr); subplot_nr = subplot_nr+1;
imagesc(xv,yv,abs(field_z_R).^2);
title('z=z_R');

subplot(3,3,subplot_nr); subplot_nr = subplot_nr+1;
imagesc(100*xv,100*yv,abs(field_far).^2);
title('far field');
end

```

A.3.3. Pulse Shape

Description

The module `pulse.m` computes the Fourier coefficients of the temporal shape of the pulse, as needed by `gh_driving_field.m`. It can also produce elliptically polarized pulses.

The signature of the `pulse` function is

```
function [omega, coefficients] = pulse(t, config)
```

The return values are:

- `omega` is the angular frequency axis which is calculated from the `t` axis supplied as input argument. It is in scaled atomic units, i.e. a value of 1 corresponds to the angular frequency of the driving field. The array includes negative angular frequencies and starts at $\omega = 0$.
- `coefficients(C,omega_i)` is an array containing the complex Fourier coefficients of the pulse shape, for a peak value of 1. The first index gives the component C of the field vector, which may take the values 1 or 2 for elliptical polarization or just 1 for linear polarization (see `config.ellipticity` argument), and the second index gives the angular frequency corresponding to the return value `omega`.

The Fourier transformation is implemented as `conj(fft(conj(...)))` to account for the sign convention we use, which is important to know if you want to invert the Fourier transformation to get the temporal pulse shape.

The arguments are:

- `t` is the time axis, as an equally spaced, one-dimensional array. It must be in scaled atomic units, i.e. a value of 2π corresponds to one driving field period.
- `config` is a `struct()` of the following fields:
 - `config.wavelength` is the central wavelength of the driving field, in mm. This is only used for unit conversion.
 - `config.pulse_shape` (optional) is the temporal shape of the pulse. It can be one of 'constant' (continuous wave, default), 'gaussian' (a Gaussian pulse), 'super-gaussian' ($\propto \exp(-\alpha t^4)$) or 'cos_sqr' (a \cos^2 pulse). If this argument is set to a different value than 'constant', you also need to supply a `config.pulse_duration` argument which gives the FWHM of the pulse with respect to intensity in fs.
 - By default, the envelope is centered at $t = 0$ and the carrier is a cos function. You can phase shift the carrier using the optional `config.ce_phase` argument to become $\cos(\omega t + \Delta\phi)$ were $\Delta\phi$ is given by `config.ce_phase` in radians.

- By default, a the carrier is assumed to be linearly polarized. In this case, the first index of the return value `coefficients(C,omega_i)` takes only the value 1. If you specify the optional argument `config.ellipticity`, an elliptically polarized carrier

$$\frac{1}{\sqrt{1+(1-e)^2}} \begin{pmatrix} \cos(\omega t) \\ (1-e)\sin(\omega t) \end{pmatrix}$$

with given ellipticity e is assumed, with two components $C = 1, 2$. This argument can also be combined with the `config.ce_phase` argument.

Example

We calculate the spectrum of a \cos^2 pulse with a FWHM of 30 fs and a central wavelength of 1 μm . The spectrum as well as the pulse are plotted (see figure A.3.3).

```
% setup time axis: 100 driving field periods
t= -50*2*pi : 2*pi/100 : 50*2*pi;

config = struct();
config.wavelength = 1e-3; % mm
config.pulse_duration = 30; % fs
config.pulse_shape = 'cos_sqr';

% compute pulse coefficients
[omega, coefficients] = pulse(t, config);

% plot pulse and spectrum
subplot(2,1,1);
plot(t, real(ifft(conj(coefficients))));
title('pulse');
xlabel('time [s.a.u.]');

subplot(2,1,2);
plot(omega, abs(coefficients).^2);
xlim([0.5,1.5])
title('spectrum');
xlabel('angular frequency [s.a.u.]');
```

A.3.4. Dipole Response

Description

The module `dipole_response.m` calculates the Fourier-transformed dipole response on a given space grid, using the Lewenstein model as implemented in `lewenstein`

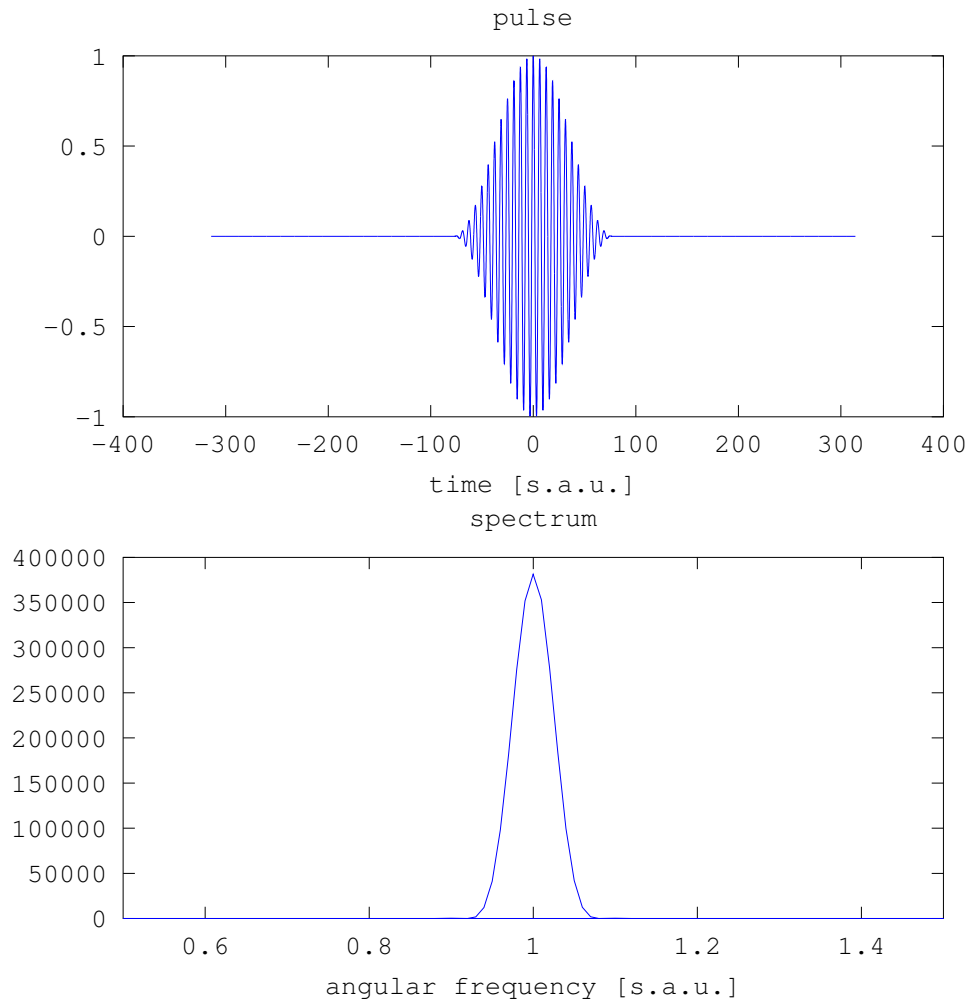


Figure A.4.: Time evolution and spectrum of a \cos^2 pulse computed by `pulse.m`

.cpp. Calculating the dipole responses is what takes most of the time when running the program, therefore an intelligent on-disk cache is implemented so that already computed dipole responses can be used later without repeating the calculation. This module can compute the dipole responses for driving fields with general time-dependent polarization.

In order to provide maximum flexibility and to avoid the need to keep big amounts of data in memory, the driving field must either be passed as a callback function that computes the driving field for a given position, or as a directory of files containing the position-dependent precomputed driving field.

Arguments and Return Values

The signature of the `dipole_response` function is

```
function [omega, response_cmc, progress] = dipole_response
    (t_cmc, xv, yv, zv, config, progress)
```

The return values are:

- `omega` is the angular frequency ω axis corresponding to the last index of the `response_cmc` return value. It is in scaled atomic units, i.e. a value of 1 corresponds to the angular frequency of the driving field.
- `response_cmc(yi,xi,zi,C,omega_i)` contains the dipole response for each space grid point and frequency. It is an array with five indices, where the first three give the position in the space grid (corresponding to the input arguments `yv`, `xv` and `zv`), the last one gives the angular frequency (corresponding to the return value `omega`), and `C` numerates the components of the dipole moment vector $\mathbf{d} = \sum_C d_C \mathbf{e}_C$, which is important if you do calculations with elliptically polarized fields.
- `progress` (optional) is a `struct()` that contains information about how much of the calculation is already done and how much time was spent. Using this return value only makes sense if you subdivide your space grid and call the `dipole_response` function multiple times. The returned `struct()` has the following fields:
 - `progress.points_total` is the total number of grid points for which the dipole response must be calculated.
 - `progress.points_computed` is the number of grid points for which the dipole response was already calculated.
 - `progress.time_spent` is the time in seconds that was already spent calculating the dipole responses.

The arguments of the `dipole_response` function are:

- `t_cmc` is the vacuum comoving time axis $t' = t - z/c$ in scaled atomic units, i.e. a value of 2π corresponds to one driving field period. It must be equally spaced.
- `xv`, `yv` and `zv` are arrays of x , y and z values, respectively, which are used to build the space grid on which the dipole responses should to be calculated.
- `config` is a `struct()` of the following fields:
 - `config.wavelength` is the central wavelength of the driving field, in mm.
 - `config.driving_field` is the name of a .m file (without the .m extension) that calculates the driving field. This callback function must have the same signature as `gh_driving_field.m`, which is described in subsection A.3.1.
 - `config.precomputed_driving_field` (optional) can be used to specify a directory that contains .mat files with a per-z-slice precomputed driving field to read in. If this option is set, `config.driving_field` is ignored and can be omitted. The directory must be organized as follows:

It must contain a file called `axes.mat` with the variables `xv`, `yv`, `zv` and `t_cmc`. If `xv`, `yv` and `t_cmc` do not match the ones given as arguments to this functions, an error is thrown. The file may also contain an optional variable `zv_precision` which defines the precision in mm when looking up the field for a specific z value in the folder. The default precision is 10^{-6} mm.

Furthermore, the directory must contain a file `data_ZI.mat` for each z position given by the `zv` variable defined in `axes.mat`, where `ZI` is the array index in `zv`. Each of these files must contain an array `driving_field(XI,YI,C,TI)`, where `XI`, `YI` and `TI` are indices corresponding to the variables `xv`, `yv` and `t_cmc` defined in `axes.mat`, respectively, and `C` is used to specify the electric field component in the case of a polarized driving field.

For pulses consisting of many oscillations, you get a fairly big amount of data per z slice, which may be problematic due to RAM limitations. Therefore it is also possible to subdivide the data files. For this, you can use a more general way of indexing the `driving_field` variable:

Instead of `driving_field(XI,YI,C,TI)`, you can use `driving_field(DI,C,TI)`, which is treated equally due to an internal reshape operation. The index `DI = (XI-1)+(YI-1)*length(xv)-1` is a flattened version of the indices `(XI,YI)`. Using this indexing, you can arbitrarily subdivide the files along the `DI` index, i.e. instead of one big file `data_1.mat` containing the array `driving_field(1:10,1:10,1,1:100)`, you can use the alternative form of indexing `driving_field(1:100,1,1:100)` and for example subdivide into two files `data_1.1.mat` and `data_1.2.mat`, containing `driving_field(1:30,1:100)` and `driving_field(31:100,1:100)`, respectively. The naming scheme for subdivided files is `data_ZI.K.mat`,

where ZI gives the z position as an index of **zv** and K is a consecutive numbering starting at 1.

- **config.ionization_potential** is the ionization potential of the model atom for which the dipole responses should be calculated, in eV.
- **config.tau_interval_length** and **config.tau_window_length** specify the shape of the window function $w(\tau)$ used in the Lewenstein formula (3.6). The former gives the length over which integration runs without window function, the latter gives the length of an appended \cos^2 window, i.e. **config.tau_interval_length** corresponds to τ_1 and **config.tau_window_length** corresponds to $\tau_{\max} - \tau_1$. Both arguments are in driving field periods, so to include all long trajectories, you should at least choose a **config.tau_interval_length** of 1. A reasonable value for **config.tau_window_length** is 0.5.
- **config.t_window_length** is the length of a falling \cos^2 window that is applied to end of the time-dependent dipole response before the Fourier transformation is performed to obtain the dipole spectrum. This is also used to reduce artifacts in the spectrum due to the fact that the array containing the time-dependent dipole response starts at zero but may end at a non-zero value. This value is also in driving field periods. A few periods, e.g. **config.t_window_length**=5, should be sufficient.
- By default, the driving field is assumed to be zero for $t < \mathbf{t_cmc}(1)$. To simulate a periodic driving field, it is possible to change this behaviour by setting **config.periodic**=1 so that the driving field is periodically continued below $\mathbf{t_cmc}(1)$. This only works if the **t_cmc** array is a periodically continuable subdivision of the interval $[0, 2\pi)$, e.g. **t_cmc** = 0 : pi/100 : 2*pi-pi/100. For periodic mode, the argument **config.t_window_length** must be zero and can be omitted.
- If the driving field has a spatial symmetry, you can specify this symmetry using the **config.symmetry** option to save computation time. Possible values are '' (no symmetry, default), 'x' (symmetry w.r.t. x - z -plane), 'y' (symmetry w.r.t. y - z -plane) and 'xy' (symmetry w.r.t. x - z - and y - z -plane).
- By default, the full spectrum is calculated, so that the returned array may get very large and unmanagable. The optional **config.cache_omega_ranges** argument can be used to confine the returned spectrum to certain interesting ranges. The format is [**start1 end1; start2 end2; ...**] where each pair of **start** and **end** values declares one range of angular frequencies ω , again in scaled atomic units.
- By default, only the dipole spectrum for positive angular frequencies ω is returned. If you want to calculate the time-dependent dipole response

using an inverse Fourier transformation, you can set the optional `config.raw` argument to 1 so that you get the raw spectrum as returned by the `fft` function, with both positive and negative angular frequencies. If `config.raw=1` is used, `config.cache_omega_ranges` must not be set.

- `config.cachedir` (optional) is a directory that is used as cache for already computed dipole spectra. If no directory is given, no result is saved and no previously saved results will be used. If a directory is given, the `dipole_response` function will check if the configuration of the cached spectra equals the current configuration, and if it does, it uses the cached spectra instead of recomputing. If the configuration of the saved spectra does not fit or if the cache directory is empty or non-existent, the dipole response is computed and saved to the cache.
- This module calls `lewenstein.cpp`. You can override the lower-level config values `epsilon_t` and `dipole_method` (see chapter A.3.8).
- Additionally, you need to supply all `config` fields required by the function specified in `config.driving_field`.
- `progress` (optional) is a `struct()` that contains information about how much of the calculation is already done and how much time was spent. Passing this as an argument only makes sense if you subdivide your space grid and call the `dipole_response` function multiple times. The passed `struct()` must have at least the field `progress.points_total` and it may have the other fields described before (see list of return values).

Example

We consider a 100 fs Gaussian pulse that propagates as a Gaussian beam with a beam waist of 10 μm , with a peak intensity of 7 W/cm^2 and a central wavelength of 1 μm . We assume a xenon gas target and compute the dipole spectrum in four different points: on-axis in the focus and 200 μm behind the focus, and the same off-axis at a distance of 5 μm from the optical axis. The resulting plots can be seen in figure A.3.4.

```
% configure time axis
time_steps = 200; % per period
t_cmc = -40*2*pi : 2*pi/time_steps : 40*2*pi; % 80 periods

% configure space grid
xv = [0 0.005]; % mm
yv = [0]; % mm
zv = [0 0.200]; % mm

% configure wavelength
config = struct();
```

```

config.wavelength = 1.0e-3; % mm

% configure driving field
config.driving_field = 'gh_driving_field';

% basic configuration
config.peak_intensity = 7e13; % W/cm^2

% temporal shape
config.pulse_shape = 'gaussian';
config.pulse_duration = 100; % fs
[pulse_omega, pulse_coefficients] = pulse(t_cmc, config);
config.omega = pulse_omega;
config.pulse_coefficients = pulse_coefficients;

% spatial shape
config.mode = 'TEM00';
config.beam_waist = 0.010; % mm

% set ionization potential for a Xe atom
config.ionization_potential = 12.13; % eV

% configure tau window and t window
config.tau_interval_length = 1;
config.tau_window_length = 0.5;
config.t_window_length = 5;

% we are only interested in harmonics below the 50th
config.cache_omega_ranges = [0 50];

% if we are only interested in 13th and 15th harmonics:
%config.cache_omega_ranges = [12.5 13.5; 14.5 15.5];

% set cache directory
config.cachedir = 'example_dipole_response_cache';

% call dipole_response
[omega, response_cmc] = dipole_response(t_cmc, xv, yv, zv,
    config);

% plot dipole spectrum at different positions
subplot(2,2,1);
spectrum = squeeze(response_cmc(1,1,1,1,:));
semilogy(omega, abs(spectrum).^2);

```

```

ylabel('|dipole_moment|^2[s.a.u.]');
title('x=z=0');

subplot(2,2,2)
spectrum = squeeze(response_cmc(1,1,2,1,:));
semilogy(omega, abs(spectrum).^2);
title('x=0_z=200um')

subplot(2,2,3)
spectrum = squeeze(response_cmc(1,2,1,1,:));
semilogy(omega, abs(spectrum).^2);
xlabel('angular_frequency[s.a.u.]');
ylabel('|dipole_moment|^2[s.a.u.]');
title('x=5um_z=0')

subplot(2,2,4)
spectrum = squeeze(response_cmc(1,2,2,1,:));
semilogy(omega, abs(spectrum).^2);
xlabel('angular_frequency[s.a.u.]');
title('x=5um_z=200um')

```

A.3.5. Propagation of Harmonics

Description

The module `harmonic_propagation.m` simulates the high harmonic generation on a space grid using `dipole_response.m` and calculates the complex electric field amplitude of the harmonic radiation within the last z plane of the grid. The `dipole_response` function is called for each z slice of the grid, so that it can be avoided to keep large amounts of data in memory.

Note that the refractive index is assumed to be one for the harmonic radiation, so that only geometrical and intensity-dependent phase matching effects can be accounted for. Absorption of the harmonics within the gas target can be specified, however. Also note that the driving fields that have an electric field component parallel to the optical axis are not supported.

Arguments and Return Values

The signature of the `harmonic_propagation` function is

```

function [z_max,omega,U] = harmonic_propagation(t_cmc, xv
    ...,
    yv, zv, dipole_response_config, config)

```

The return values are:

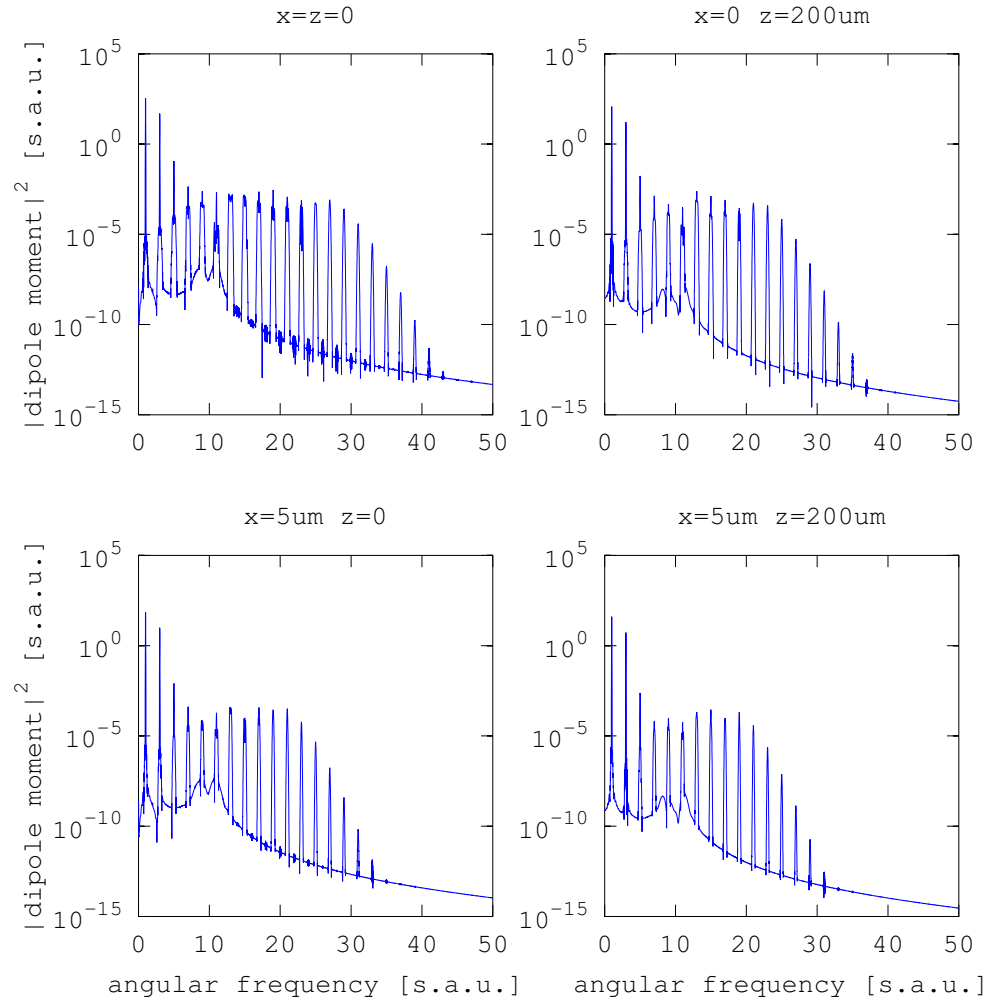


Figure A.5.: Dipole spectra calculated with the `dipole_response.m` module

- `z_max` is the z value in mm in which the complex electric field `U` is computed.
- `omega` is the angular frequency ω axis corresponding to the last index of the `U` return value. It is in scaled atomic units, i.e. a value of 1 corresponds to the angular frequency of the driving field.
- `U(yi,xi,component,omega_i)` is the complex electric field amplitude of the harmonic radiation within the last z plane of the input grid, in scaled atomic units. It is an array with four indices, where the first two give the position within the output plane (corresponding to the input arguments `yv`, `xv`), the third the electric field component, and the last one gives the angular frequency (corresponding to the return value `omega`).

The arguments are:

- `t_cmc` is the vacuum comoving time axis $t' = t - z/c$ in scaled atomic units, i.e. a value of 2π corresponds to one driving field period. It must be equally spaced.
- `xv`, `yv` and `zv` are arrays of x , y and z values, respectively, which are used to build the space grid on which the dipole responses are should be calculated. As trapezoidal integration in z direction is used, you need to make sure that the `zv` array has at least two elements. For testing purposes, it might be convenient to pass an array with only one element to save computation time. In this case, a target width of 1 nm is assumed and a warning is issued.
- `dipole_response_config` is a `struct()` that is passed to the `dipole_response` function as `config` argument. See the documentation of the `dipole_response` function for more information. Note: Until general polarization is implemented, you must choose these configuration parameters so that only component of the dipole moment vector is returned by `dipole_response`.
- `config` is a `struct()` of the following fields:
 - `config.density` is the density of the gas, in mm^{-3} . Currently, the gas density is assumed to be constant over the entire space grid.
 - `config.pressure` (optional) can be used instead of `config.density` to provide the gas pressure in bar. Then, the density is calculated using the ideal gas law assuming a temperature of 295 K.
 - `config.transmission` and `config.transmission_photon_energy` (optional) can be used to provide a photon-energy-dependent transmission curve of the target gas, so that the absorption of harmonics within the gas target can be taken into account. If not given, no absorption is assumed. `config.transmission` must be an array specifying the transmission with respect to intensity for the used gas at a pressure of 30 Torr, a temperature of 295 K and a path of 1 cm. `config.transmission_photon_energy`

is the corresponding photon energy axis and must be in eV. This data can be obtained e.g. from http://henke.lbl.gov/optical_constants/gastrn2.html [13].

- By default, it is checked whether the discretization of the space grid is fine enough by comparing the phases of the of the harmonic radiation at adjacent grid points. If the phase difference is too big, a warning is issued. This check is computationally quite expensive, so if you are sure that the discretization is fine you can disable the checks setting `config.nochecks=1`.

Example

We consider a 1 μm continuous wave Gaussian laser beam with a beam waist of 10 μm and a peak intensity of 7 W/cm^2 that hits a xenon gas target with a diameter of 50 μm . The electric field right after the gas target is computed and plotted (compare figure A.3.6). Although a continuous wave laser with such a high intensity is not realistic, it makes sense to approximate a pulsed laser with a long pulse duration by a CW laser, as this decreases the computation time drastically.

```
% configure time axis - only one period as we use periodic
mode
time_steps = 70; % per period
t_cmc = 0 : 2*pi/time_steps : 2*pi;
t_cmc = t_cmc(1:end-1);

% configure space grid
xv = -.010:0.0002:.010; % 20 um
yv = -.010:0.0002:.010; % 20 um
zv = -0.025:0.005:0.025; % 50 um

% configure wavelength
config = struct();
config.wavelength = 1.0e-3; % mm

% configure driving field
config.driving_field = 'gh_driving_field';

% basic configuration
config.peak_intensity = 7e13; % W/cm^2

% temporal shape
config.pulse_shape = 'constant'; % optional, is default
value
[pulse_omega, pulse_coefficients] = pulse(t_cmc, config);
```

```

config.omega = pulse_omega;
config.pulse_coefficients = pulse_coefficients;

% spatial shape
config.mode = 'TEM00';
config.beam_waist = 0.010; % mm

% set ionization potential for a Xe atom
config.ionization_potential = 12.13; % eV

% configure tau window and t window
config.tau_interval_length = 1;
config.tau_window_length = 0.5;

% activate periodic mode
config.periodic = 1;

% we are only want to plot harmonic 21
config.cache_omega_ranges = [21-0.1 21+0.1];

% set cache directory
config.cachedir = 'example_harmonic_propagation_cache';

% configuration for harmonic propagation
propagation_config = struct();
propagation_config.pressure = 0.1; % bar

% set absorption data:
% xenon_abs.dat is the file downloaded from
% http://henke.lbl.gov/optical\_constants/gastrn2.html
% (first two lines commented out with %)
load('xenon_abs.dat');
propagation_config.transmission_energy = xenon_abs(:,1);
% photon energy in eV
propagation_config.transmission = xenon_abs(:,2);
% for 30 torr, 1 cm

% call harmonic_propagation
[z_max, omega, U] = harmonic_propagation(t_cmc, xv, yv, zv
    , config, propagation_config);

% plot electric field amplitude of harmonic radiation
% - due to config.cache_omega_ranges and using periodic
% mode, the

```

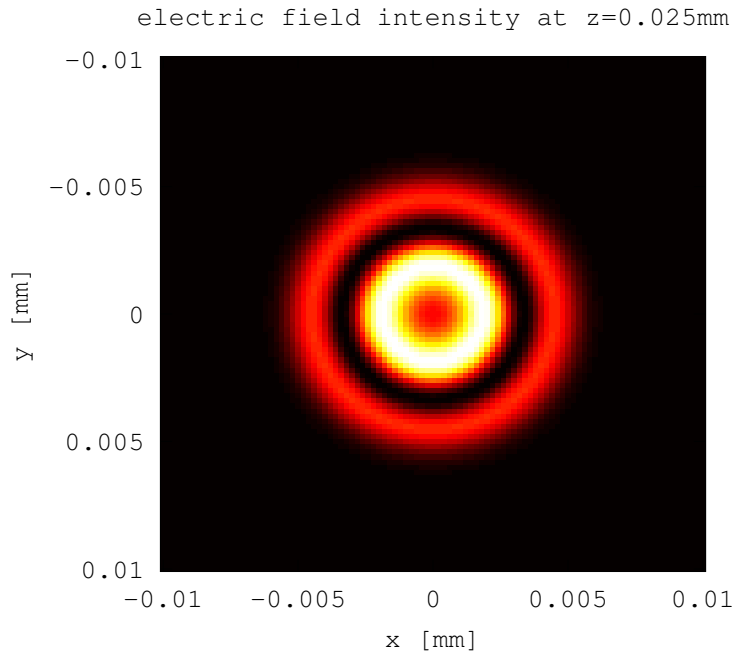


Figure A.6.: Electric field of 21st harmonic in plane right after gas target as computed with `harmonic_propagation.m`

```
% omega_i index of U is one-dimensional, so we can use
% squeeze to get a 2d array
intensity = abs(squeeze(U)).^2;

imagesc(xv,yv, intensity / max(max(intensity)))
title(['electric field intensity at z=' num2str(z_max) 'mm
'])
xlabel('x [mm]')
ylabel('y [mm]')
```

A.3.6. Far Field

Description

Given the complex electric field amplitude in an input plane, the module `farfield.m` calculates the field in a far-away plane using the far field approximation. This is useful to get the electric field of the harmonics on a screen plane from the electric field right after the gas target as calculated by `harmonic_propagation.m`.

Arguments and Return Values

The signature of the `farfield` function is

```
function [E_plane] = farfield(xv,yv,z_U,omega, U, config)
```

The return value `E_plane(omega_i,component,yi,xi)` is an array that contains the complex electric field amplitude in the output plane for each angular frequency. It has four indices, where the first gives the angular frequency (corresponding to the `omega` argument), the second the electric field component, and the last two give the position within the output plane (corresponding to the meshgrid input arguments `config.plane_x`, `config.plane_y`).

The arguments are:

- `xv` and `yv` are arrays of x and y values for the input plane, respectively. The unit is mm.
- `z_U` is the z position of the input plane, in mm.
- `omega` is the angular frequency axis for the input field given by the argument `U`. It is in scaled atomic units, i.e. a value of 1 corresponds to the angular frequency of the driving field.
- `U(yi,xi,component,omega_i)` is the complex electric field amplitude in the input plane, and has to be in scaled atomic units, and conventional (not co-moving) coordinates. It must be an array with four indices, where the first two give the position in the input plane (corresponding to the `yv` and `xv` arguments), the third gives the electric field component and the last one gives the angular frequency (corresponding to the argument `omega`).
- `config` is a `struct()` of the following fields:
 - `config.wavelength` is the central wavelength of the driving field, in mm. This is only used for unit conversion.
 - With `config.plane_x` and `config.plane_y` you specify the rectangle within the output plane in which the far field is computed. These arguments must be a meshgrid of output plane coordinates, in mm. The meshgrid can be produced with the `meshgrid` function: `[plane_x, plane_y] = meshgrid(plane_xv, plane_yv)` where `plane_xv` and `plane_yv` are 1-dimensional arrays of x and y values, respectively.
 - `config.plane_distance` is the distance of the output plane from the origin, in mm.
 - For the far field approximation, a 2-dimensional spatial Fourier transform on the input field is calculated. Then an interpolation must be done in this spatial frequency spectrum. Due to the oscillating complex phase, this is only possible if the resolution of the spectrum is fine enough. If it

is not, a warning is issued (see `config.nochecks` argument). In this case, you must increase the resolution of the spectrum by increasing the size of the input plane. This can be achieved by applying zero padding using the two optional arguments `config.padding_x` and `config.padding_y`. The format of both arguments is `[start, end]`, where `start` and `end` specify the interval to which the `xv` and `yv` arguments should be extended by zero padding.

- `config.plane_theta`, `config.plane_phi` and `config.plane_psi` can be used to rotate the output plane around the x , y and z axis, respectively, with the specified angles. If more than one argument is given, first the rotation around the z axis is applied, then around the y axis and then around the x axis. If no rotation is given, the output plane is parallel to the x - y -plane. All three angles are in degree.
- By default, it is checked whether the zero padding applied with the `config.padding_x` and `config.padding_y` arguments is sufficient by comparing the phases of adjacent points in the spatial frequency spectrum of the input field. If it is not, a warning is issued. As this check is computationally quite expensive, you can disable the checks by setting the optional argument `config.nochecks=1`.

Example

The harmonic radiation U right after the gas target is computed as shown in the example of the `harmonic_propagation.m` module. Using this and the corresponding variables `z_max`, `omega`, `xv` and `yv`, we can compute the complex electric field of the harmonic radiation on a screen that is placed 50 cm behind the focus, standing perpendicular to the optical axis. The output can be seen in figure A.3.6.

```
% ... z_max, omega and U computed like in the example for
% the harmonic_propagation module ...

% Now: compute far field from field U behind target

% configure far field module
plane_xv = -20:0.05:20; % mm
plane_yv = -20:0.05:20; % mm
[plane_x, plane_y] = meshgrid(plane_xv, plane_yv);
config.plane_x = plane_x;
config.plane_y = plane_y;

config.plane_distance = 500; % mm

config.padding_x = [-0.02 0.02];
config.padding_y = [-0.02 0.02];
```

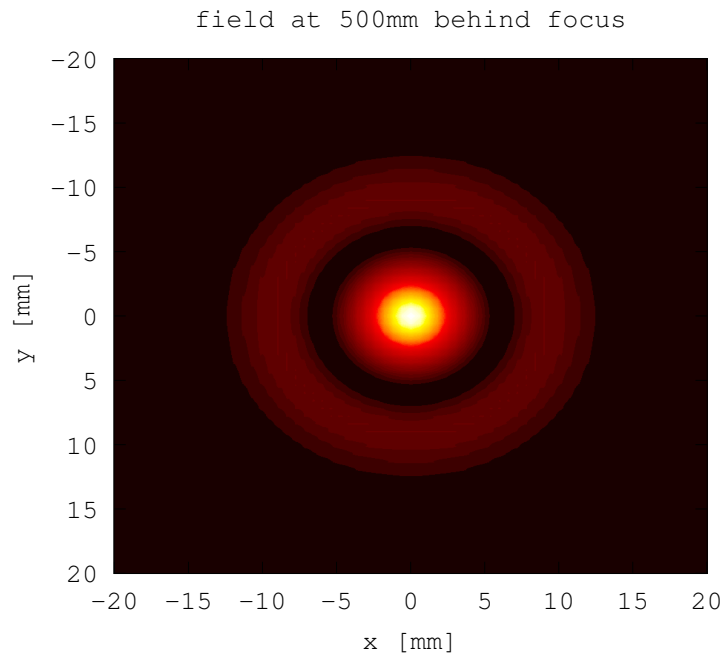


Figure A.7.: Electric field of 21st harmonic at a z plane 50cm behind the focus, as computed by `farfield.m`

```
% compute far field
E_plane = farfield(xv,yv,z_max,omega, U, config);

% as the omega_i index of U is one-dimensional, the
% omega_i
% index of E_plane also is, so we can use squeeze to get a
% 2d array
intensity = abs(squeeze(E_plane)).^2;

imagesc(plane_xv,plane_yv, intensity / max(max(intensity))
)
title(['field_at_', num2str(config.plane_distance) 'mm_
      behind_focus'])
xlabel('x [mm]')
ylabel('y [mm]')
```


A.3.7. Conversion between SI units and scaled atomic units

Description

Most calculations are done in scaled atomic units internally. The `sau_convert.m` module helps you to convert between SI units and scaled atomic units.

Arguments and Return Values

The signature of the `sau_convert` function is

```
function converted = sau_convert(value, quantity, target,
                                config)
```

The return value `converted` is the converted input value, either in SI units or in scaled atomic units depending in which direction you ask the module to convert. The arguments are:

- `value` is the value that should be converted
- `quantity` is the respective physical quantity as a symbol; currently supported are 'E' (electric field), 'V' (energy), 's' (length), 'A' (area), 'V' (volume), 't' (time) and 'v' (speed)
- `target` gives the direction of the conversion. If it is 'SI', the value is converted from scaled atomic units to SI units; if it is 'SAU', conversion is done vice versa
- `config` is a `struct()` with at least one field:
- `config.wavelength` must be set to the central wavelength of the driving field, in mm.

Example

```
% set driving field wavelength
config = struct();
config.wavelength = 1e-3; % mm

% convert a time value of 2*pi in scaled atomic units,
% which corresponds to one driving field period, to SI
% units, i.e. to seconds
T_SI = sau_convert(2*pi, 't', 'SI', config)
```

A.3.8. Matlab Interface to the Implementation of the Lewenstein Model

Description

Unlike the other modules, the Lewenstein model is implemented in C++ (`lewenstein.hpp`). The file `lewenstein.cpp` provides the Matlab (or Octave) interface to this C++ code and must be compiled to a `.mex` file in order to be usable from within Matlab/Octave (see A.2). It computes the time-dependent single-atom dipole response from a given driving field $\mathbf{E}(t)$ and is able to deal with elliptically polarized fields.

This module is rather low-level, so you might prefer to use the `dipole_response.m` module which has a more convenient interface and calls this module for you.

Arguments and Return Values

The signature of the `farfield` function is

```
dt = lewenstein(t, Et, config);
```

The return value `dt(C,t_i)` is an array that contains the time-dependent dipole moment in scaled atomic units, where the first index gives the component of the dipole moment vector and the second index gives the time (corresponding to the argument `t`). The arguments are:

- `t` is the time axis in scaled atomic units, i.e. a value of 2π corresponds to one driving field period. The array must be equally spaced and start at 0.
- `Et(C,t_i)` is the time-dependent electric driving field in scaled atomic units. The first index gives the component of the electric field vector, so that you can pass elliptically polarized driving fields. The second index gives the time (corresponding to the argument `t`).
- `config` is a `struct()` of the following fields:
 - `config.ip` is the ionization potential I_p of the used model atom in scaled atomic units.
 - `config.epsilon_t` (optional) is a small positive constant that is used to prevent integral (3.6) from diverging at $\tau = 0$, in scaled atomic units. The default value is 10^{-4} .
 - `config.weights` is a one-dimensional array specifying the window function $w(\tau)$ of (3.6). The corresponding τ axis is given by the `t` argument.
 - `config.dipole_method` (optional) specifies which method should be used to compute the bound-continuum dipole matrix elements $\mathbf{D}(\mathbf{v})$. Currently, 'H' (default) and 'symmetric_interpolate' are supported. The former uses dipole matrix elements for a scaled hydrogen-like potential, as given by (2.2). When this method is used, you can specify the

depth of the potential in units of I_p using the optional `config.alpha` argument.

The latter allows you to pass arbitrary spherically symmetric functions $\mathbf{D}(\mathbf{v}) = \tilde{D}(|\mathbf{v}|) \cdot \hat{\mathbf{v}}$ by providing an array $\tilde{D}(v_i)$ in which $\tilde{D}(|\mathbf{v}|)$ is interpolated. The v_i axis is assumed to be equally spaced and to start at zero, and the spacing must be given by the `config.deltav` argument. The array $\tilde{D}(v_i)$ must be specified with the `config.dipole_elements` argument. Both arguments are in scaled atomic units. Note that in the Lewenstein model, the dipole spectra are very sensitive to the dipole matrix elements. As linear interpolation is used, you need to make sure to use a sufficiently fine discretization to avoid artifacts.

Erklärung

Hiermit erkläre ich, die vorliegende Arbeit selbständig verfasst zu haben und keine anderen als die in der Arbeit angegebenen Quellen und Hilfsmittel benutzt zu haben.

München, 3. September 2013

.....